Faculty of Physics, Astronomy and Applied Computer Science
Jagiellonian University in Kraków

PhD Thesis

Selection of Q.Clear image reconstruction parameters for small lesions with the pathological uptake of ^{68}Ga-labeled somatostatin analogues

Konrad Skórkiewicz

Thesis written under the supervision

of prof. dr hab. n. med. Anna Sowa-Staszczak

and prof. dr hab. Kazimierz Łątka

Kraków 2023

Wydział Fizyki, Astronomii i Informatyki Stosowanej

Uniwersytet Jagielloński

Oświadczenie

Ja niżej podpisany Konrad Skórkiewicz (nr indeksu: 1063239) doktorant Wydziału Fizyki, Astronomii i Informatyki Stosowanej Uniwersytetu Jagiellońskiego oświadczam, że przedłożona przeze mnie rozprawa doktorska pt. *Selection of Q.Clear image reconstruction parameters for small lesions with the pathological uptake of ^{68}Ga-labeled somatostatin analogues"* jest oryginalna i przedstawia wyniki badań wykonanych przeze mnie osobiście, pod kierunkiem prof. dr hab. n. med. Anny Sowy-Staszczak oraz prof. dr hab. Kazimierza Łątki. Pracę napisałem samodzielnie.

Oświadczam, że moja rozprawa doktorska została opracowana zgodnie z Ustawą o prawie autorskim i prawach pokrewnych z dnia 4 lutego 1994 r. (Dziennik Ustaw 1994 nr 24 poz. 83 wraz z późniejszymi zmianami).

Jestem świadom, że niezgodność niniejszego oświadczenia z prawdą ujawniona w dowolnym czasie, niezależnie od skutków prawnych wynikających z ww. ustawy, może spowodować unieważnienie stopnia nabytego na podstawie tej rozprawy.

Kraków, dnia …… ……

podpis doktorantki/doktoranta

Acknowledgments

I would like to thank sincerely Mrs. Supervisor and Mr. Supervisor for their support and all valuable tips given during the research.

I also extend my thanks to Prof. dr hab. Andrzej Budkowski for a fruitful suggestion to use the Minkowski method to analyze the images obtained in the work, and to Prof. dr hab. Joanna Raczkowska for help in the implementation of this method for the analysis of some of the results obtained.

Family and friends for their support and motivation while pursuing the set goal.

I would also like to thank my wife Sylwia and daughter Otylia.

Podziękowania

Pragę serdecznie podziękować Pani Promotor i Panu Promotorowi za wsparcie oraz wszystkie cenne wskazówki udzielone podczas prowadzonych badań.

Podziękowania kieruję również do Pana prof. dr hab. Andrzeja Budkowskiego za owocną sugestię użycia metody Minkowskiego do analizy uzyskanych w pracy obrazów oraz Pani prof. dr hab. Joanny Raczkowskiej za pomoc w implementacji tej metody do analizy części otrzymanych wyników.

Rodzinie oraz przyjaciołom za wsparcie i motywację podczas dążenia do wyznaczonego celu.

Słowa podziękowania kieruję również do mojej żony Sylwii oraz córki Otylii.

Disclosure

The research presented in this paper was carried out with the financial support of two research grants:

- N17/MNW/000016, N17/MNS/000060,
- "Research support module" as a part of the "Excellence Initiative – Research University" program at the Jagiellonian University.

Abstract

PET/CT diagnostics uses iterative image reconstruction techniques to obtain reliable information about the biodistribution of radiotracers in the human body. Clinically used devices are usually equipped with several image reconstruction algorithms. Changing the image reconstruction algorithm or its modification by changing the number of iterations and subsets affects the study results.

The aim of my doctoral dissertation was to analyze the available image reconstruction algorithms in a clinically used PET/CT device installed at the University Hospital in Kraków (Department of Nuclear Medicine). The purpose of the analysis was to select an algorithm intended for the reconstruction of images of oncological patients treated and diagnosed in the Department of Nuclear Medicine. In particular, the conducted analysis was to lead to the selection of an algorithm that allows for a more accurate diagnosis of patients with neuroendocrine tumours, in whom a study with ^{68}Ga-labelled somatostatin analogues is performed at various stages of the disease.

The research was divided into two stages. In the first stage, the PET/CT examination of the NEMA phantom was analyzed. The study analyzed the effect of changing the β parameter (range 150 – 950, step 100) in the VP FX+Q.Clear and VP HD+Q.Clear algorithms on the semi-quantitative Standard Volume Uptake (SUV) scores and the ratio of the measured sphere to the background (CR coefficient). The homogeneity of the background in the body part of the phantom was also assessed with Minkowski analysis.

In the second part of the work, a comparative analysis of three image reconstruction algorithms VP FX+Q.Clear, VP HD+Q.Clear and VP FX was performed using the results of patients with advanced forms of cancer. The group of patients was carefully selected, because the impact of the reconstruction algorithm changes was tested, especially for small (< 2cm) metastases of neuroendocrine tumours.

The results obtained allowed us to assess the effect of the beta parameter value on Q.Clear reconstruction and the suitability of using Q.Clear reconstruction at various stages of cancer, especially at its early stage. The selected value of the β parameter is in the range of 350-450. It was found that it is more advantageous to use the VP FX+Q.Clear algorithm, which uses information from the correction of attenuation and time of flight of photons generated during the annihilation phenomenon.

Key words: Q.Clear algorithm, neuroendocrine tumours, NEMA standards

Streszczenie

Diagnostyka PET/CT wykorzystuje iteracyjne techniki rekonstrukcji obrazu w celu uzyskania wiarygodnej informacji o biodystrybucji radioznaczników w ciele człowieka. W urządzeniach stosowanych klinicznie dostępnych jest zazwyczaj kilka algorytmów rekonstrukcji obrazów. Zmiana algorytmu rekonstrukcji obrazu lub jego modyfikacja poprzez zmianę ilości iteracji i podzbiorów wpływa na wyniki badań.

Celem mojej rozprawy doktorskiej było przeprowadzenie analizy dostępnych algorytmów rekonstrukcji obrazu w stosowanym klinicznie urządzeniu PET/CT zainstalowanym w Szpitalu Uniwersyteckim w Krakowie. Przeprowadzona analiza miała na celu wybór algorytmu przeznaczonego do rekonstrukcji badań pacjentów onkologicznych leczonych i diagnozowanych w Zakładzie Medycyny Nuklearnej. W szczególności, prowadzona analiza miała doprowadzić do wyboru algorytmu, który pozwala na bardziej dokładną diagnostykę pacjentów z guzami neuroendokrynnymi, u których na rożnych etapach choroby wykonywane jest badanie ze znakowanymi izotopem ^{68}Ga analogami somatostatyny.

Badania podzielono na dwa etapy. W pierwszym etapie dokonano analizy badań PET/CT fantomu NEMA. W badaniu przeanalizowano wpływ zmiany parametru β (zakres 150 – 950, krok co 100) w algorytmach VP FX+Q.Clear i VP HD+Q.Clear na wyniki półilościowe jak Standard Uptake Volume (SUV) oraz stosunek zmierzonego wychwytu w sferach do tła (CR coefficient). Wykonano również ocenę jednorodności tła w części body fantomu z wykorzystaniem analizy Minkowskiego.

W drugiej części pracy dokonano analizy porównawczej trzech algorytmów rekonstrukcji obrazu VP FX+Q.Clear, VP HD+Q.Clear i VP FX z wykorzystaniem wyników badań pacjentów z zaawansowaną postacią choroby nowotworowej. Grupa pacjentów była bardzo starannie wyselekcjonowana, gdyż badano wpływ zmian parametrów algorytmu rekonstrukcji w szczególności dla małych zmian przerzutowych guzów neuroendokrynnych, których zmierzony największy wymiar wynosił <2cm.

Uzyskane wyniki pozwoliły ocenić wpływ wartości parametru β dla rekonstrukcji Q.Clear oraz słuszności wykorzystywania rekonstrukcji Q.Clear, na różnych etapach choroby nowotworowej, a zwłaszcza na jej wczesnym etapie. Najbardziej optymalna wartość parametru beta mieści się w przedziale 350 – 450. Oceniono, że najkorzystniej jest stosować algorytm VP FX+Q.Clear, który wykorzystuje dane z korekcji osłabienia oraz czasu przelotu fotonów powstałych podczas zjawiska anihilacji.

Słowa kluczowe: algorytm Q.Clear, guzy neuroendokrynne, standardy NEMA

Table of contents

List of Abbreviations

PET/CT – positron emission tomography combined with computed tomography

PET/MRI – positron emission tomography combined with magnetic resonance imaging

SPECT/CT – single-photon emission computed tomography combined with CT

NET – neuroendocrine tumor

GEP-NET – gastroenteropancreatic neuroendocrine tumor

WCC – well counter correction

SUV – standard uptake volume

18F-FDG – fludeoxyglucose

VP FX – VUE Point FX (the proper name of the OSEM algorithm with time of flight)

VP HD – VUE Point HD (the proper name of the OSEM algorithm)

5-year OS – 5-year Overall Survival

SEER – surveillance, epidemiology and end result program

BGO – bismuth germanium oxide

LYSO – lutetium–yttrium oxyorthosilicate

PMT – photomultiplier tubes

PVE – partial volume effect

LOR – line of response

FBP – filtred backprojection

FFT – fast Fourier Transform

ART – algebraic reconstruction technique

ILST – iterative least-squares technique

MLEM – maximum likelihood expectation maximization

OSEM – ordered subsets expectation maximization

ASIR – adaptive statistical iterative reconstruction

TOF – time-of-flight

PSF – point spread function

NEMA – national electrical manufacturers association

GEP-NET – gastro-entero-pancreatic neuroendocrine tumors

SST – somatostatin

SSTR – somatostatin receptors

GMP – good manufacturing practice

TLC – thin layer radiochromatograph

Topogram – 2-dimensional CT imaging

FDA – Food and Drug Administration

FWHM – full width at half maximum

CRC – contrast recovery coefficient

PRRT – peptide receptor radionuclide therapy

Chapter I – Introduction

1. Physical basics of ionizing radiation

Radioactivity is the ability of the atomic nuclei to decay. The radioactive decay is the process by which an unstable atomic nucleus spontaneously transforms to another nucleus with emission of ionizing radiation (figure 1.1). There are several types of radioactive decays, the most common are: alpha ($\boldsymbol{\alpha}$), beta ($\boldsymbol{\beta^- and\ \beta^+}$), gamma ($\boldsymbol{\gamma}$), and electron capture ($\boldsymbol{EC}$) decays:

a) Alpha decay $\quad {}^{A}_{Z}X \longrightarrow {}^{A-4}_{Z-2}Y + {}^{4}_{2}He^{2+}$ (1)

b) Beta (-) decay $\quad {}^{A}_{Z}X \longrightarrow {}^{A}_{Z+1}Y + e^- + \nu_e^-$ (2)

c) Beta (+) decay $\quad {}^{A}_{Z}X \longrightarrow {}^{A}_{Z-1}Y + e^+ + \nu_e$ (3)

d) Gamma decay $\quad {}^{A}_{Z}X^* \longrightarrow {}^{A}_{Z}X + \gamma$ (4)

e) Electron capture $\quad {}^{A}_{Z}X + {}^{0}_{-1}e \longrightarrow {}^{A}_{Z-1}Y + \nu_e$ (5)

Radioactive decay occurs regardless of the chemical or physical environment. Usually, during molecular (alpha, beta, and EC) decays the accompanying gamma decays can be observed [1].

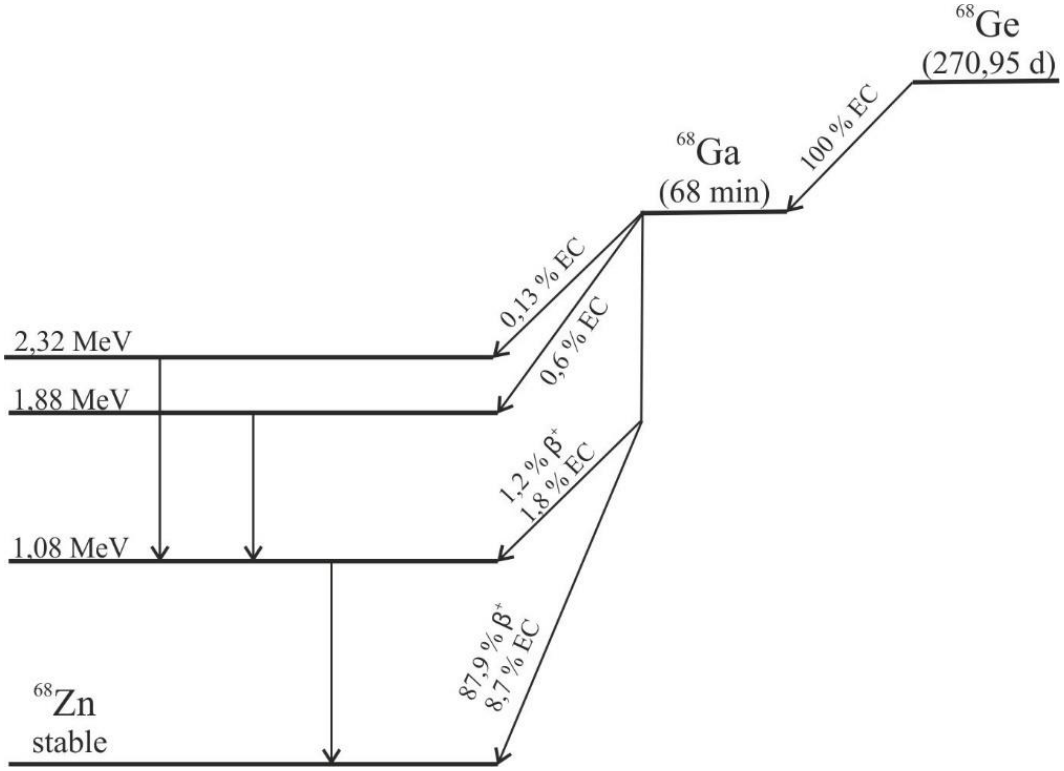

Figure 1. 1 Decay scheme of ^{68}Ga. Possible energy transitions with their probability were presented [1].

$$^{68}_{32}Ge\ (EC) \longrightarrow\ ^{68}_{31}Ga\ (\beta^{+}, \gamma, EC) \longrightarrow\ ^{68}_{30}Zn + e^{+} + \nu_e + \gamma\ (1077\ keV) \quad (6)$$

The amount of radiation emitted from the radioactive material is described by the activity $\boldsymbol{A}$, which is expressed as the number of nuclear transformations in one second. The unit of activity in the SI system is Bequerel (Bq) from the name of the famous chemists, now considered the inventor of the radioactivity phenomenon – Antoine Henri Becquerel.

$$1\ Bq = \frac{1\ decay}{1s} \quad (7)$$

The change in activity A (t) over time is described by the law of radioactive decay, which is one of the basic laws in nuclear physics [1]:

$$A(t) = A_0 e^{-\lambda t} \quad (8)$$

where λ is so-called decay constant, A_0 – activity in t=0, t – time after t=0. It is easy to show that the decay constant λ can be expressed as:

$$\lambda = \frac{(ln2)}{T_{1/2}} \quad (9)$$

where $T_{1/2}$ – half-life of the isotope.

1.2. Interactions of gamma radiation with matter

The transmission of gamma radiation through the material medium is accompanied by energy loss as a result of interactions with the orbital electrons and the absorber nucleus. There are three main ways of transferring energy to the medium, which are described below [1].

a) Photoelectric effect

In the photoelectric phenomenon, the gamma quantum transfers all its energy to the electron bound on the shells. If the transferred energy is higher than the binding energy, it allows the ejection of an electron to the medium in the form of a so-called photoelectron [1].

b) Compton scattering

Compton scattering takes place on weakly bound electrons. The incident photon transfers some of its energy to the electron that is thrown away and then propagates in the medium; however, its energy is lower [1].

c) Pair production

A photon with energy higher than 1.02 MeV can interact with the nucleus of the medium and produce two particles - a negative electron (e^-) and positive electron (e^+) called positron. The

positron propagating in the medium combines soon with one of the electrons present in the material and the process of annihilation takes place [1].

2. PET/CT technique

In PET technique, we are based on the beta plus decay, where the positron is created (3). The positron is one of the three $\boldsymbol{\beta^+}$ decay products. Passing through the matter, positron loses energy as a result of inelastic Coulomb interactions with electrons [2]. At the end of the road in tissue, the positron interacts with one of the electrons in a process called annihilation, in which two 511 keV gamma quanta are generated from the mass of particles (fig. 1.2). During annihilation, two quanta of gamma are formed, which diverge at an angle of about 180 degrees (exactly 180 degrees when both electrons, i.e. e^+ and e^- are at rest) in opposite directions (7) [3].

$$\boldsymbol{e^+ + e^- \longrightarrow 0,511\ MeV\ \gamma\ + 0,511\ MeV\ \gamma} \tag{10}$$

We can observe 0.5 degree random variation of the 180 degree which have impact to spatial resolution, called *annihilation angle blurring* [4]. In about of 0.003 % annihilation events more than 2 gammas quanta are created [3].

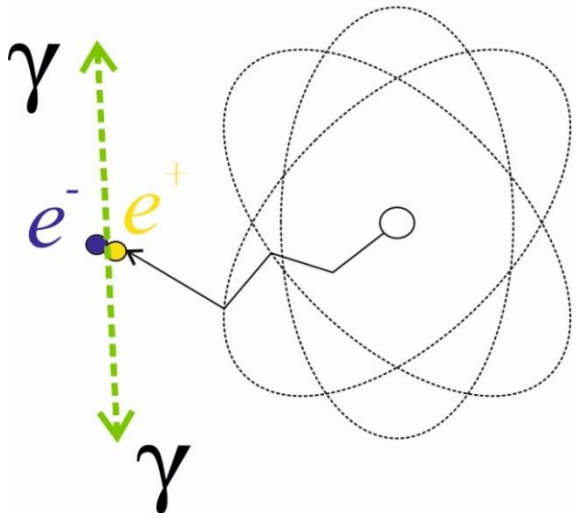

Figure 1. 2 Beta plus decay and annihilation process.

2.1. Radioisotopes in PET

The tracers used in PET technique are based on some particular radioisotopes. The radioisotopes production for PET imaging usually requires application of cyclotron techniques [5] (Table 1.1), where the target material is bombarded with high-energy charged particles [6]. Unfortunately, the application of short-lived isotopes is profitable only when the cyclotron is close to the PET centers. In case of some isotopes it is possible to build generators in which a

long-lived parent isotope undergoes a radioactive decay. As a result of disintegration, a daughter isotope is formed, which is then leached out of the generator using chemical solutions [5].

Table 1. 1 The most important PET radionuclides [7].

Nuclide	Half-life $T_{1/2}$	Average β^+energy [MeV]	Mean range in tissue [mm]	β^+intensity [%]	Production
^{11}C	20.385 min	0.386	0.3	99.75	Cyclotron
^{13}N	9.965 min	0.492	1.4	99.80	Cyclotron
^{15}O	2.037 min	0.735	1.5	99.90	Cyclotron
^{18}F	109.77 min	0.250	0.2	96.73	Cyclotron
^{62}Cu	9.673 min	1.314	2.3	97.43	Cyclotron
^{64}Cu	12.701 h	0.278	0.2	17.60	Cyclotron
^{68}Ga	67.71 min	0.830	1.9	89.14	Cyclotron/Generator
^{82}Rb	76.38 s	1.479	2.6	95.43	Cyclotron/Generator
^{86}Y	14.74 h	0.660	0.7	31.9	Cyclotron
^{89}Zr	78.41 h	0.396	0.3	22.74	Cyclotron
^{124}I	4.176 days	0.820	0.8	22.7	Cyclotron

The 68 gallium isotope for PET imaging can be obtained in two ways, in the cyclotron and from the ^{68}Ge /^{68}Ga generator (fig. 1.3) [8]. The production of the generators widens considerably the number of centers using the ^{68}Ga radioisotopes in their daily work. Unfortunately only registered medicinal products can be used in clinical practice, which affects significantly and negatively the price and availability. Currently in Poland a brand generator by Eckert&Ziegler allows the production of radiopharmaceuticals based on gallium 68.

In this kind of generators a long-lived parent ^{68}Ge isotope is placed on TiO_2 matrix. The 5 ml of 0.1 M HCL solution is applied in the elution process. The sterile, ultrapure solution of HCl is recommended for clinical applications. During the elution, the daughter isotope (^{68}Ga) is eluted from the column in a form of gallium chloride, which can be used in further labeling processes e.g. for diagnosis purposes based on somatostatin analogues. There are some Germanium isotope impurities present in the elution but they are at the level of about 0.001 % in gallium chloride solution, if the previous elution was carried out no later than 24 hours before radiolabelling [9].

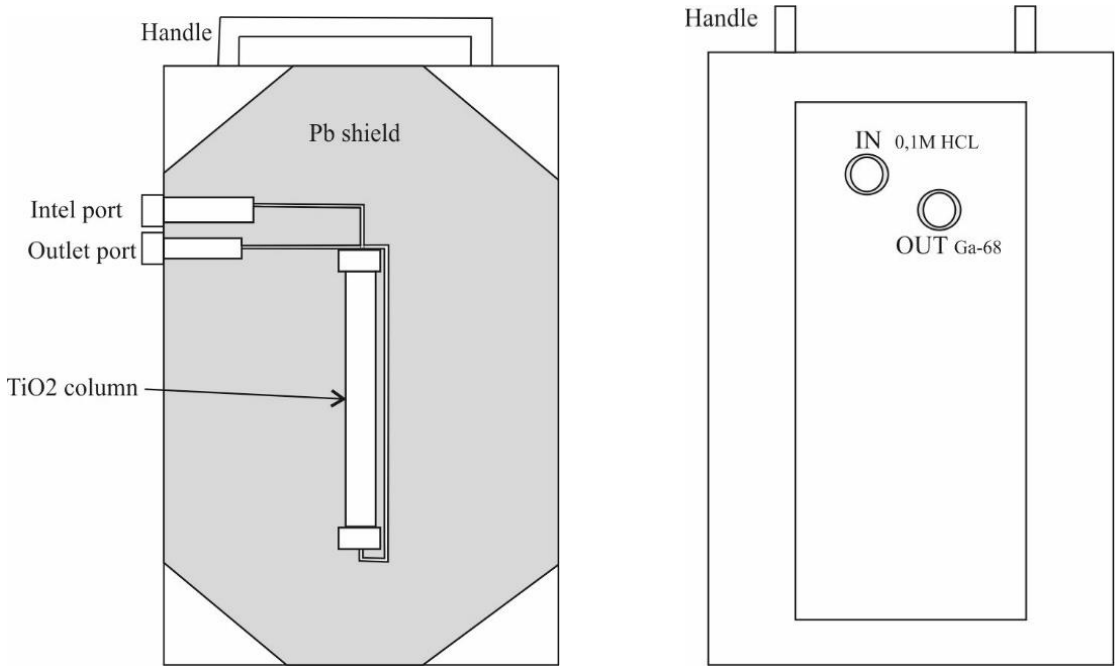

Figure 1.3 Scheme of $^{68}Ge/^{68}Ga$ generator by Eckert&Ziegler [9].

2.2. PET imaging technique

PET imaging is classified as molecular imaging technique, which allows to observe the metabolism or affinity to receptors of radiopharmaceutical at the cellular level with the appropriate spatial resolution compared to currently available other imaging techniques (Table 2.). This rises these technique sensitivity and specificity to high levels [7]. Additionally, numerous possibilities of PET application result from a wide range of various radiopharmaceuticals, defining the PET technique as a well suitable for routine cancer diagnostic as well as for special tasks in neurology or cardiology where the other non-invasive image techniques have some limitations [5].

Table 1. 2 Characteristics of selected imaging techniques [7].

Feature	Ultrasound	CT	MRI	SPECT	PET
Image acquisition method	Reflection at interfaces	X – ray attenuation	Electromagnetic excitation of nuclei, relaxation	Single-photon emission of radioisotopes	β^+ - Decay of radioisotopes annihilation radiation
Spatial resolution	1 – 3 mm	30μm	< 30μm – 1mm	0.3 – 1.5 mm	1 – 4 mm
Acquisition time	10-30 s	1 s per scan	1 – 10 min	10 – 60 min	10 – 80 mn
Sensitivity	Good	Low	Low /Medium	High	Very high
Specificity	Low	Low	Medium	High	Very high

The basic PET system consists of several parts, the most important are: gantry with gamma ray detector blocks, patient bed and computer with image reconstruction software [5] (fig. 1.4). The PET imaging is based on photons being the effect of annihilation processes which move to different directions at the speed of light. Gamma photons almost simultaneously reach the detector blocks located on opposite sides of the gantry, the first line of detection system.

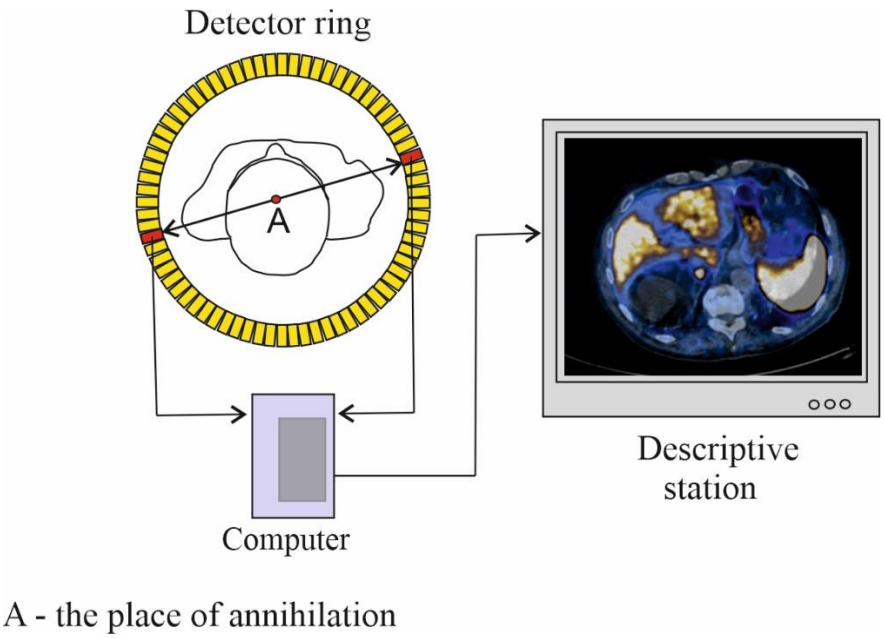

Figure 1.4 PET system scheme.

If the annihilation angle geometry is preserved (180 degrees) and the time difference between the detection of two quanta falls in the pre-defined time window (usually 6 – 12 nanoseconds), the event is called the true coincidence and contributes to the reconstruction of the final diagnostic image. In addition to true coincidences, the detection system also receives numerous accidental coincidences [4] (fig. 1.5).

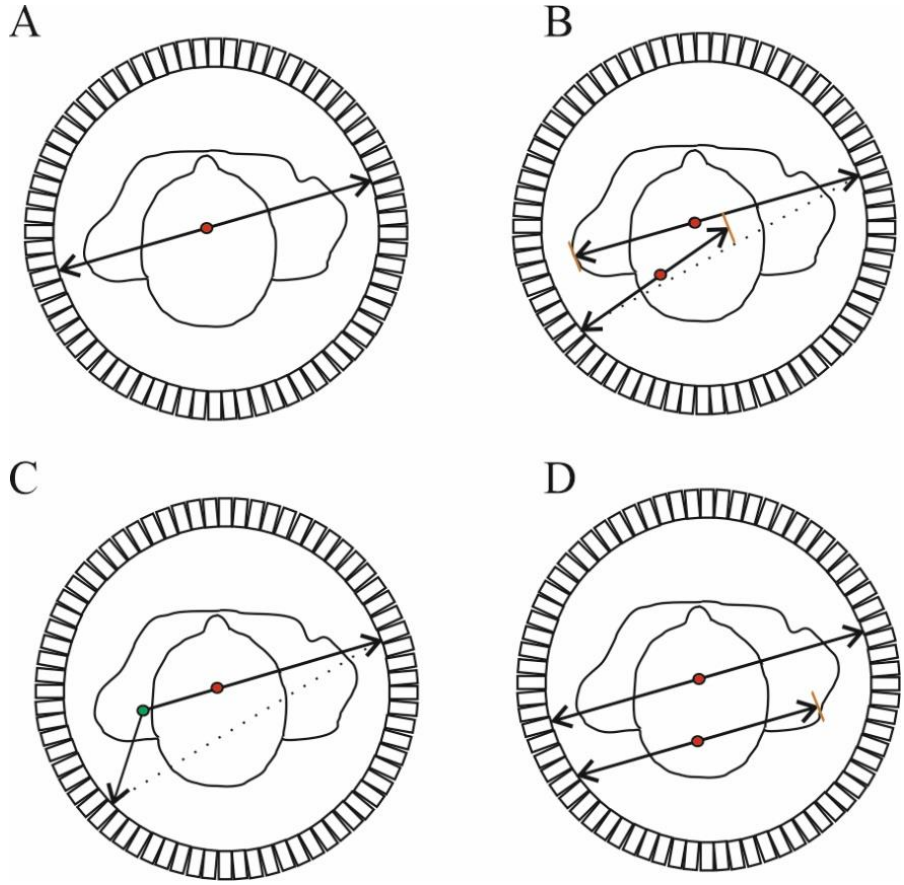

Figure 1. 5 The various coincidences types in PET detection system [5]. From left side: true, random, scattered and multiple coincidences.

The understanding of the physics lying behind the annihilation process allows to avoid additional gamma collimation systems. For successful image reconstruction, detectors need to record many true coincidence events, that's why patients must receive sufficiently high radiopharmaceutical activity [5].

2.2.1. Detection system in PET

The PET detection system consists of many detector blocks, containing photomultipliers (PMT) and signal processing electronics (fig. 1.6). In detection systems, scintillation crystals with appropriate properties are most often used [10], but other materials with similar characteristics are increasingly being sought, e.g. plastic detectors [11].

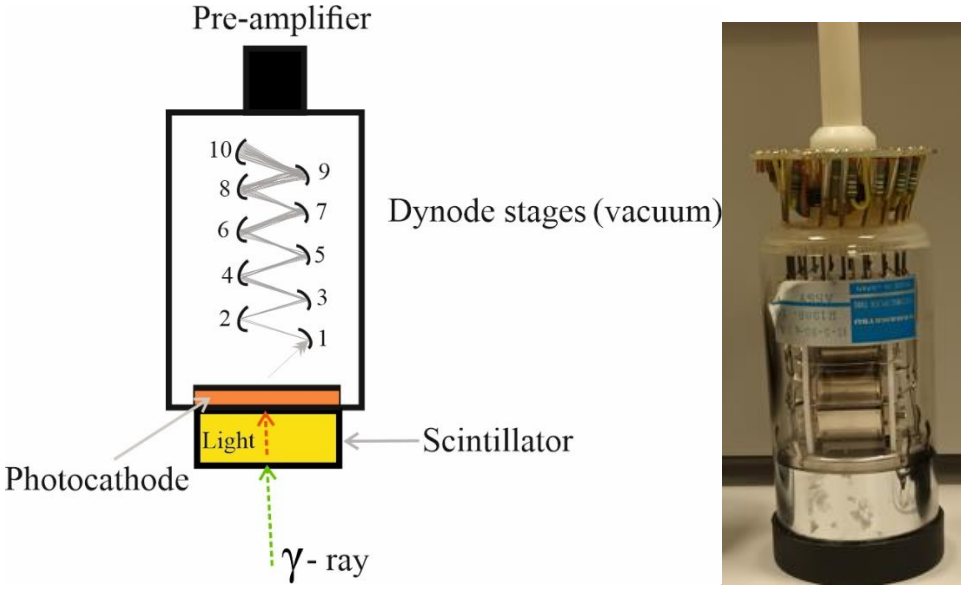

Figure 1. 6 Diagram of the detector block and photography of the detector (Hamamatsu, Japan).

As a result of absorbing radiation, the detector generates a signal. This allows to identify the amount of absorbed energy, the location of the event and the time of radiation interaction with the detector. The scintillator crystal needs to present some of important properties [10] (Table 1.3):

a) high probability of absorption for the photons with the energy of 511 keV,
b) high spatial resolution and good energy resolution,
c) very high time resolution and an acceptable price.

Table 1. 3 Properties of some scintillators used in PET detectors [5].

	BaF_2	BGO	LSO	GSO	LYSO	$LaBr_3$	LFS	LuAP	LuI_3
Effective atomic no. (Z)	54	74	66	59	60	47	63	65	60
Linear atten. coeff. (cm^{-1})	0.44	0.92	0.87	0.62	0.86	0.47	0.82	0.9	0.56
Density (gm cm^{-3})	4.89	7.13	7.4	6.7	7.1	5.3	7.3	8.34	5.6
Index of refraction	-	2.15	1.82	1.85	1.81	1.88	1.78	1.95	-
Peak wavelength (nm)	220	480	420	430	420	370	430	365	470
Decay constant (ns)	0.8	300	40	65	41	25	35	18	30
Hydroscopic	Slight	No	No	No	No	No	No	No	Yes

The choice of the optimal crystal depends on the future applications of the PET imaging system. The higher the scintillator's absorption coefficient for 511 keV gamma rays, the higher the light emission capability. As the thickness increases, the probability of the scintillator interaction with detected 511 keV gamma rays rises. A similar value of the absorption coefficient occurs in BGO and LYSO, so the use of these materials of appropriate thickness allows to obtain detector characterized with high sensitivity. One thing is certain, the perfect detector does not exist currently and this is the field for further extensive research [12].

Behind the detector, there is a vacuum tube of a PMT, where scintillation photons are highly amplified (>10^6) and converted to the electric signal [13]. Signal amplification in PMT results from the high voltage applied to the dynodes located inside, on which the generation of secondary electrons occur. Due to PMT size limitations (they should not be too small), current PET detection systems share PMT for several scintillation crystal segments, built in the form of a matrix. The location of the actual crystal segment in which the gamma absorption process took place is based on a weighted response algorithm from all PMTs [5].

2.2.2. Limitations of PET

In PET, as in other imaging techniques, there are also some limitations in obtained spatial resolving power, which is crucial for imaging. Limitations of PET imaging are due to physical factors [13]:

- size of the detector element d,
- deviations from the correct angle for quantum annihilation,
- the range of positrons in tissue, resulting from its energy before the annihilation process,
- decoding error of the detection system.

Spatial resolution in PET system can be express as follows:

$$\boldsymbol{R = a\sqrt{(d/2)^2 + b^2 + r^2 + c^2}} \tag{11}$$

where: a – degradation factor dependent on the reconstruction method used ($1 \leq a \leq 1.3$); d/2 – geometrical response midway between coincident detection pixels of size d; b – is the detector positioning accuracy, r – is the average positron range in tissue before annihilation, and finally c – is the non-colinearity effect, which can be expressed as follows:

$$\boldsymbol{c = 0.5D \cdot \tan(0.25) = 0.0022 \cdot D} \tag{12}$$

D – is the distance between coincident detectors

The blurring effect resulting from the positron range in tissue can be described using root-mean-square (rms) value of the positron range distribution, expressed as a measure of the effective range r of positron,

$$r = 2,355 \cdot rms \quad (13)$$

Table 1. 4 Effect of positron range on spatial resolution (mm) in PET [13].

Radioisotope	β^+ energy [MeV]		Resolution [mm]
	Max	Average	r
^{11}C	0.96	0.385	0.92
^{13}N	1.20	0.491	1.4
^{15}O	1.73	0.735	2.4
^{18}F	0.64	0.242	0.54
^{64}Cu	0.65	0.278	0.55
^{68}Ga	1.90	0.836	2.8
^{82}Rb	3.36	1.52	6.1

Detector geometry influences the sensitivity of the system. This issue includes the probability that both photons resulting from positron annihilation will reach the detector surfaces e.g. if the axial length of the scanner is doubled, the PET system sensitivity rises almost four times. Modern PET systems are equipped with the function of measuring and correcting changes in the detector temperature. This allows for the accurate qualification and evaluation of the detected gamma radiation [13].

Most of the PET systems limitations result from the physical properties of the detection system applied and ionizing radiation, imposing the resolution capability for clinical systems> The best achieved resolution is about of 2.5 mm [14]. Even reduction of the size of individual detectors only slightly improves the resolving power of PET system [14]. Due to the non-zero kinetic energy of positrons resulting from radioactive decay and the extent of the tissue, PET images using isotopes with high energy positron may be slightly blurred.

An important factor influencing the semi-quantitative assessment in PET is the Partial Volume Effect (PVE). This effect causes that the intensity value of individual voxels in the image is different than it actually seems to be. This phenomenon is related to the finite resolving power of the PET system and the limitations of signal sampling, i.e. the size of individual voxels. Patient movement also has a similar effect. PVE also has a very significant effect the assessment of activity distribution, especially for small hot spots surrounded by an area with a low concentration of the radiopharmaceutical. Then you get SUV values much lower than they actually are [15].

3. Reconstruction process in PET

3.1. Introduction

Image reconstruction in PET involves processing of the raw data obtained from the detection system into a 3-dimensional image of radiopharmaceutical biodistribution in the patient's body. The choice of the right image reconstruction algorithm affects the obtained image resolution (see equation 11) and should be adapted to the type of examination and the selected radiopharmaceutical [5]. Simultaneous detection of annihilation quanta by opposite detectors is defined by the system as a line of response (LOR) (fig. 1.7) [16].

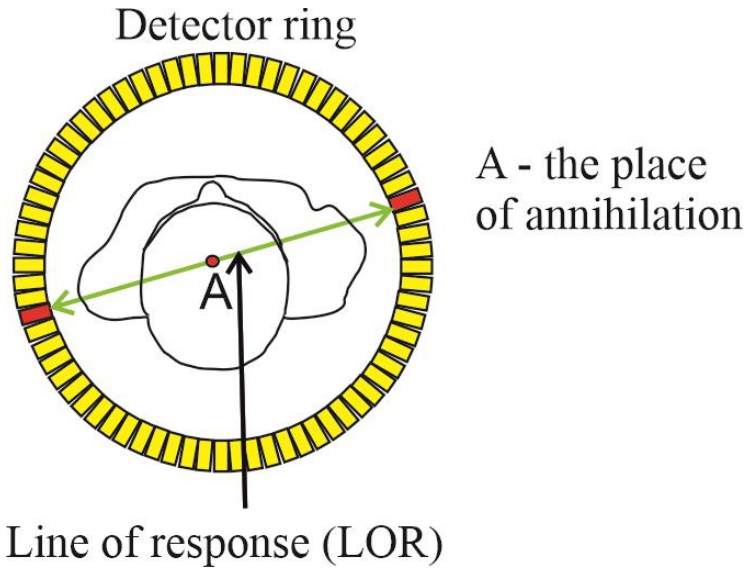

Figure 1.7 Line of response in PET system.

In order to reconstruct the image from a set of acquired LORs it is required to switch from the Cartesian coordinate system to coordinates dependent on the detection system. Each radius can be characterized by its angle of inclination φ relative to the OY axis and its distance $\boldsymbol{t}$, in relation to the center of the coordinate system (fig. 1.8) [17].

$$\boldsymbol{x cos\varphi + y sin\varphi = t} \tag{14}$$

The projection function $P_\varphi(t)$ is obtained as a parallel integral of LOR for a given φ angle

$$\boldsymbol{P_\varphi(t) = \int_{L(\varphi,t)} f(x,y) ds} \tag{15}$$

What could be written with the use of delta function:

$$\boldsymbol{P_\varphi(t) = \int_{-\infty}^{\infty}\int_{-\infty}^{\infty} f(x,y)\delta(x cos\varphi + y sin\varphi - t)\, dx\, dy} \tag{16}$$

As a result of this transformation called Radon transformation [19] and collection of all projections in $0 < \varphi < 2\pi$, we obtain 2-D raw data in the form of a sinogram (fig. 1.9) [16].

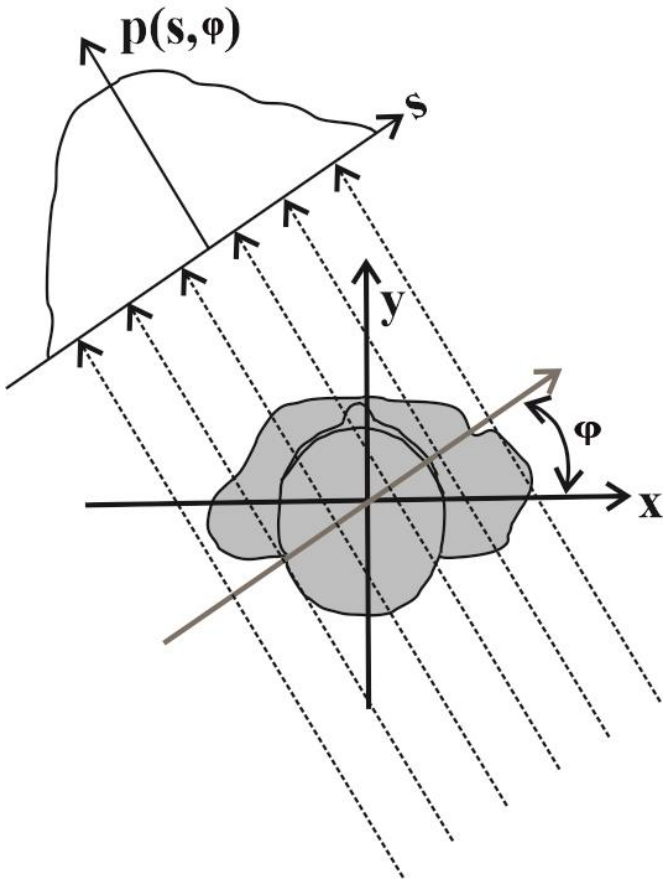

Figure 1. 8 The projection of the object [15].

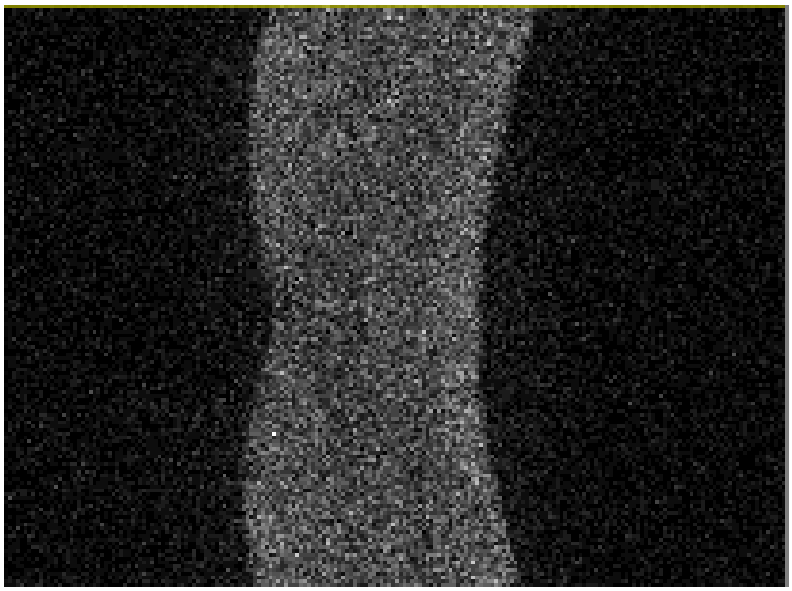

Figure 1. 9 A PET sinogram obtained for the hot spheres part of the NEMA Body Phantom .

Currently, the 3D image acquisition technique is used in multi-scoring PET, which involves the simultaneous collection of LOR from direct, cross and high oblique planes [17]. The use of this data collection technique significantly increases the sensitivity of the method and reduces the examination time. However, it requires separate collection of sinograms for LOR oblique planes [3].

3.2. Reconstructions

The data obtained in the form of a sinogram should be reconstructed with the use of the appropriate algorithms of image reconstruction. In commercial systems, manufacturers provide the right tools, but specific features and reconstruction parameters should be selected accordingly to the medical procedures performed.

Over the years, the development of technology has influenced not only the quality of detection systems. It also has enabled significant progress in the development of image reconstruction algorithms. This progress has significantly influence the quality of the obtained imaging results in nuclear medicine. Below I will describe some techniques of image reconstruction.

3.2.1. Analytical techniques

One of the first methods of image reconstruction in nuclear medicine was Filtred Backprojection (FBP). This is probably due to the fact that it was widely used in computed tomography [20]. Due to the speed and accuracy FBP is one of the most frequently used analytical image reconstruction techniques [19]. Image reconstruction in FBP can basically be divided into two stages to obtain adequate image quality: filtration and backprojection [21].

- In the filtration step we get optimal shape of the object. In this case, we transform the detector function using Fast Fourier Transform (FFT) to the frequency domain. Next, the spectrum is filtered by ramp filter and the high-frequencies are highly amplified. After the filtration process is completed, the data are recalculated into the initial domain by applying the Inverse Fourier Transform. This allows for the blur reduction [21].
- Filtered data (each projection) is “back projected” on the orientation it was measured [20].

This analytical technique has been used extensively due to computing speed and low demands for the computer system performance[20,21]. However, the use of this reconstruction technique was affecting the high radiation dose to patient in CT imaging [21]. Limitations of FBP also occur in the PET technique due to the degradation factors described in section 3.2.2. and the inability to take into account stochastic variation in photon detection [20].

3.2.2. Iterative Image Reconstruction

The above-described limitations of FBP forced the development of other image reconstruction techniques category – iterative methods. In this group, two types of reconstruction can be distinguished:

- classical, based on the reconstruction of linear equations eg. Algebraic Reconstruction Technique (ART) and Iterative Least-Squares Technique (ILST), which will not be discussed in this work,
- statistical, aiming at maximizing a likelihood function eg. Maximum Likelihood Expectation Maximization (MLEM), based on Poisson distribution statistics [23].

The process of image reconstruction using the iterative technique uses the solution estimation process, which is then refined in subsequent steps called iterations. Successive result forecasts are compared to the measured projections, which allows for further modifications to the initial estimates [24]. In getting the right data, we are looking for the vector $\boldsymbol{f}$ ($\boldsymbol{unknow\ image}$), which enables us to solve the equation:

$$\boldsymbol{p = Hf + n} \tag{17}$$

where: $\boldsymbol{p}$ is projection data, $\boldsymbol{H}$ is projection process (matrix), n – additional noise

Each of the iterative techniques consists of 5 basic components [5, 25, 26]:

- object parameterization, or image model definition - most often a discrete image values for different pixels,
- system model – $\boldsymbol{H}$ characterizes imaging system,
- model for data – relationship between measured and expected value,
- cost function and governing principle, which defines the best image.

a) Maximum Likelihood Expectation Maximization (MLEM)

In the MLEM technique, we are looking for the most probable activity distribution based on the Poisson distribution statistical model [27]:

$$\hat{\boldsymbol{f}}_{\boldsymbol{j}}^{(\boldsymbol{n+1})} = \frac{\hat{\boldsymbol{f}}_{\boldsymbol{j}}^{(\boldsymbol{n})}}{\sum_{\boldsymbol{i}`} \boldsymbol{H}_{\boldsymbol{i}`\boldsymbol{j}}} \sum_{\boldsymbol{i}} \boldsymbol{H}_{\boldsymbol{ij}} \frac{\boldsymbol{p}_{\boldsymbol{i}}}{\sum_{\boldsymbol{k}} \boldsymbol{H}_{\boldsymbol{ik}} \hat{\boldsymbol{f}}_{\boldsymbol{k}}^{(\boldsymbol{n})}} \tag{18}$$

where: $\hat{\boldsymbol{f}}_{\boldsymbol{j}}^{(\boldsymbol{n+1})}$ is the next estimate for the j-th voxel, which is based on previous estimate $\hat{\boldsymbol{f}}^{\boldsymbol{n}}$; $\boldsymbol{H}_{\boldsymbol{i}\ \boldsymbol{j}}$ – part of the system model $\boldsymbol{H}$ (matrix), which characterizes the imaging system and represents the probability that an emission from image element (voxel) $\boldsymbol{j}$ is detected in i-th projection [17,20].

An additional advantage of MLEM is the possibility of introducing the effects of image degradation into the reconstruction: attenuation, scattering, depth-dependent resolution and

geometrical weighting [27]. The assumptions used in MLEM form the basis of many iterative methods [20].

b) Ordered Subsets Expectation Maximization (OSEM)

In order to accelerate the iterative reconstruction process, the introduction of subsets was proposed in the 1990s, as Ordered Subsets Expectation Maximization reconstruction algorithm. In this case, the data are divided into subsets with the same number of projections.

The iteration process in this reconstruction takes place for the data obtained in subsets $\boldsymbol{S_b}$. One iteration is to go through all subsets [20].

$$\hat{\boldsymbol{f}}_{\boldsymbol{j}}^{(\boldsymbol{n},\boldsymbol{b})} = \frac{\hat{\boldsymbol{f}}_{\boldsymbol{j}}^{(\boldsymbol{n},\boldsymbol{b}-\mathbf{1})}}{\sum_{\grave{\boldsymbol{i}} \in \boldsymbol{S_b}} \boldsymbol{H}_{\grave{\boldsymbol{i}}\,\boldsymbol{j}}} \sum_{\boldsymbol{i} \in \boldsymbol{S_b}} \boldsymbol{H}_{\boldsymbol{ij}} \frac{\boldsymbol{p_i}}{\sum_{\boldsymbol{k}} \boldsymbol{H_{ik}} \hat{\boldsymbol{f}}_{\boldsymbol{k}}^{(\boldsymbol{n})}} \tag{19}$$

c) Adaptive statistical iterative reconstruction (ASIR)

This was the first so-called hybrid algorithm for clinical use, which combines both analytical and iterative methods. This algorithm uses a statistical approach with the addition of FBP information in each image reconstruction. The FBP component contributes 10% to the ASIR algorithm, but may vary depending on the user's needs. The lavel of changes enables adaptation to specific applications of the imaging device [27].

The use of the ASIR algorithm allows to reduce noise in the image and the radiation dose for the patient during the examination. The improvement in image quality results from a better estimation of the photon statistics and the scanned object [28].

3.2.3. Time-of-Flight technique (TOF)

One of the most interesting solutions in current PET systems is the use of the time of flight technique (TOF). This technique involves the measurements of the difference in time of flight between two coincidence quanta. Research on the TOF technique has been conducted since the 1980s. The basic requirement is the use of fast detectors allowing the accurate measurement of the time differences between quanta detections. Detectors based on lutetium–yttrium oxyorthosilicate (LYSO) scintillators achieve a time resolution of about 600 ps, resulting in an event location uncertainty of 9 cm [30, 31] and are well suitable for the TOF application.

The use of TOF allows to introduce a certain probability of positron annihilation site on the resulting LOR, which significantly increases the signal-to-noise ratio in the image [30]. The place where the annihilation took place is determined as follows [32]:

$$\boldsymbol{\Delta s = c\Delta t/2} \tag{20}$$

Where: Δs is the distance of the annihilation point from the center of the LOR, Δt is the time difference of the photon flight, and c is the speed of light.

3.3. Iterative reconstruction techniques in PET/CT GE Discovery MI DR system

The PET/CT system has several types of image reconstruction. The algorithms used are briefly described below.

a) VUE Point HD (VP HD) – OSEM 3D

The reconstruction of the VUE Point HD includes the dead time, geometry of the detection system and normalization in the system model. The algorithm takes into account the curvature of the detection system and a block array of detectors, which reduces the influence of uneven response lines resulting from the curvature of the system [34].

b) VUE point FX (VP FX) – OSEM 3D + TOF

The VUE Point FX algorithm has been extended to include the time-of-flight assessment. The extension of the VUE point HD algorithm resulted in the fact that the difference in time is also taken into account in the assessment of corrections such as: normalization, randomness, dead time, dispersion, attenuation [35].

- **SharpIR algorithm (VUE Point HD, VUE Point FX)**

The introduction to the 3D iterative image reconstruction technique of the correction concerning the detector Point Spread Function (PSF) made it possible to improve the image contrast. The amendment contains a number of information about the parameters of the PET scanner: detector geometry, sampling width or parallax effect, which affect the quality of the scanner's response function [36]. Introduction of PSF to OSEM algorithm reduces the image blur and improves the PET image quality in the case of small lesions characterized by the enhanced uptake. Response is assessed for each PET detector system offered by GE based on point source measurements. The SharpIR algorithm is available with all possible reconstruction methods [13, 34, 37].

- **Q.Clear**

Q.Clear is a quantitative analysis method used to iteratively reconstruct PET images until full convergence is achieved. This method uses Bayesian penalized likelihood, which includes an additional term that reduces the noise value in the resulting image. This part of the equation avoids the increase in image noise while maintaining full data convergence in contrast to the most frequently used – OSEM algorithm [38]. The penalized likelihood function is written as follows:

$$\hat{\boldsymbol{x}} = \arg \boldsymbol{max}_{\boldsymbol{x}\geq \boldsymbol{0}} \sum_{\boldsymbol{i}=\boldsymbol{1}}^{\boldsymbol{n_d}} \boldsymbol{y_i} \log [\boldsymbol{Px}]_{\boldsymbol{i}} - [\boldsymbol{Px}]_{\boldsymbol{i}} - \boldsymbol{\beta R}(\boldsymbol{x}) \tag{21}$$

where y_i – measured PET data, P – matrix geometry system, x – image estimate, R(x) – penalty control noise, β – is responsible for the control of the regulating element depending on the data statistics.

Both tests carried out on phantoms, eg. NEMA, as well as the results of imaging tests allow to show clearly considerable differences between the images obtained with the use of the Q.Clear and OSEM algorithms. The images obtained with the Q.Clear technique have a better quality, they also allow to obtain a better signal-to-noise ratio. Additionally they show higher SUV values. This algorithm is used together with the VUE Point HD and VUE Point FX techniques [39,40]. According to the manufacturer's information and many scientific publications, the Q.Clear algorithm allows to increase the sensitivity of the system to detect small changes [13, 41, 42, 43].

3.4. Multimodal systems

Currently, multimodality systems such as SPECT/CT, PET/CT and PET/MR are used in nuclear medicine. Such system are the fusion of molecular and anatomical imaging techniques [43]. This solution results in the huge diagnostic benefits for patients, even when using an additional radiation source (which is the CT module) increasing the total absorbed dose obtained from a single examination. A CT scanning is performed for two purposes:

a) to describe precisely the patient's anatomy,
b) to allow the attenuation correction to the image reconstruction algorithm (fig 1.10).

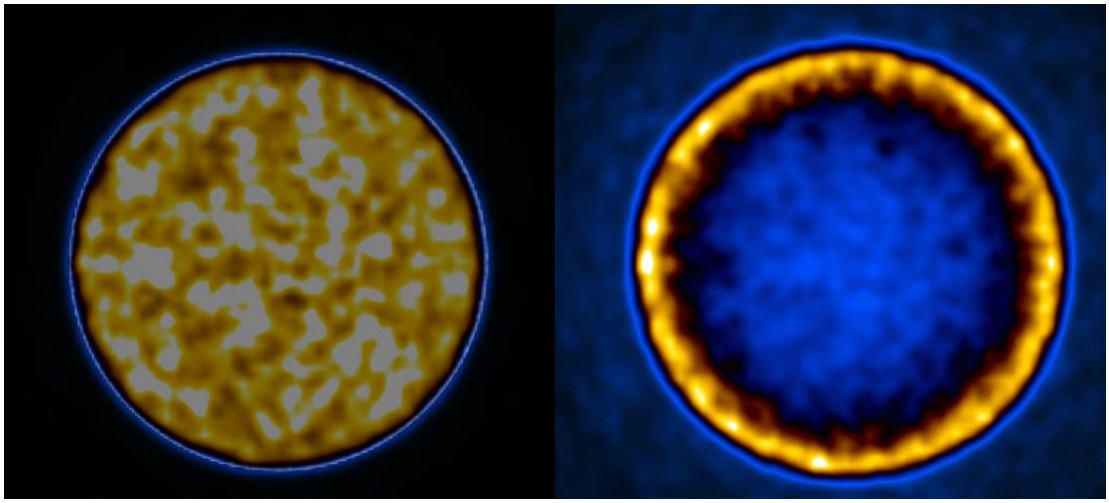

Figure 1. 10 Image with and without attenuation correction (University Hospital in Kraków).

As a result of two independent scans: PET and CT, a fusion of images can be obtained. This allows for the proper and precise localization of the increased or reduced accumulation of radiopharmaceutical in respect to patients anatomy [44]. An example of such fusion is presented in fig. 1.11.

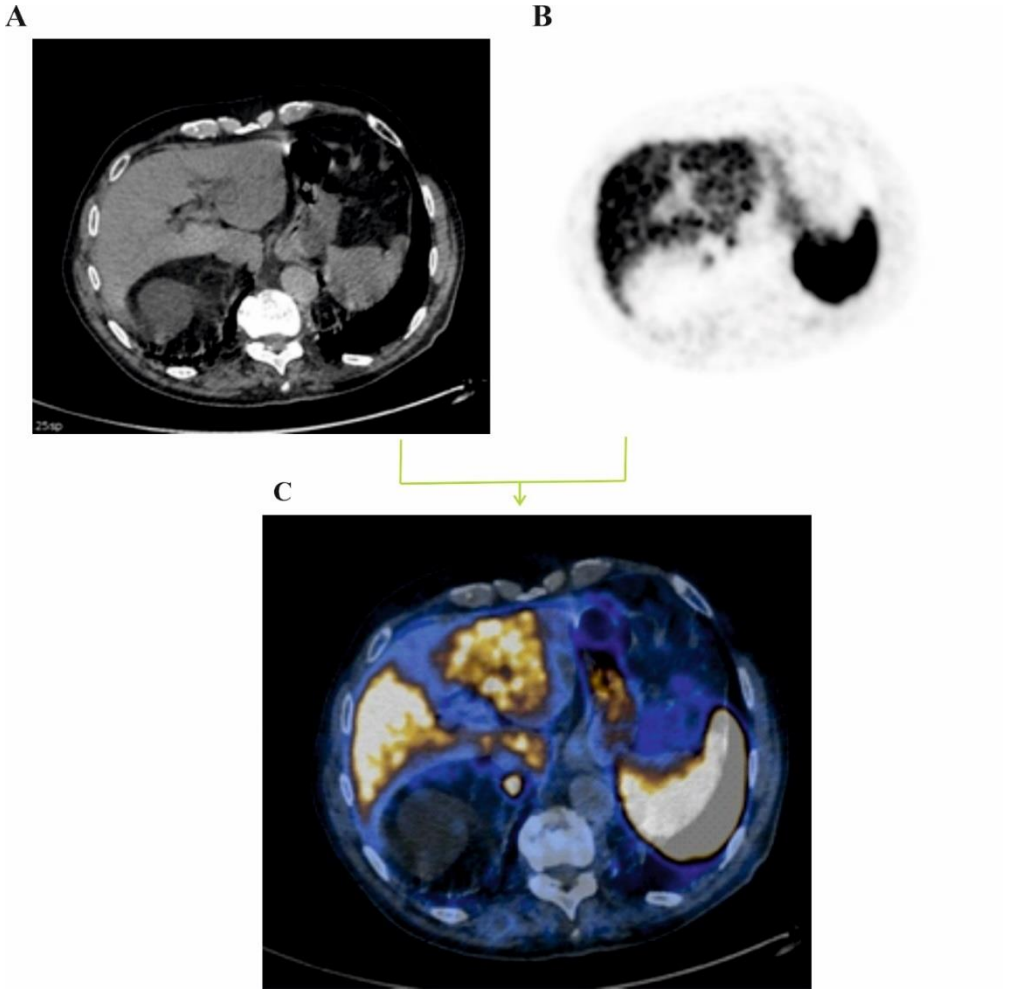

Figure 1. 11 PET, CT and fusion image PET/CT examinations with DOTATATE labelled with ^{68}Ga (University Hospital in Kraków).

As it was mentioned above, annihilation quanta can interact with the patient's body. The probability of interaction depends on the absorption coefficients of individual body elements. In order to eliminate the effect of radiation with matter on the diagnostic image during a CT scan, a map of the patient's body is created as a matrix of weakening factors called attenuation correction and implied for algorithm of PET image reconstruction [45]. The improvement of the image due to such technique can be seen in fig. 1.12.

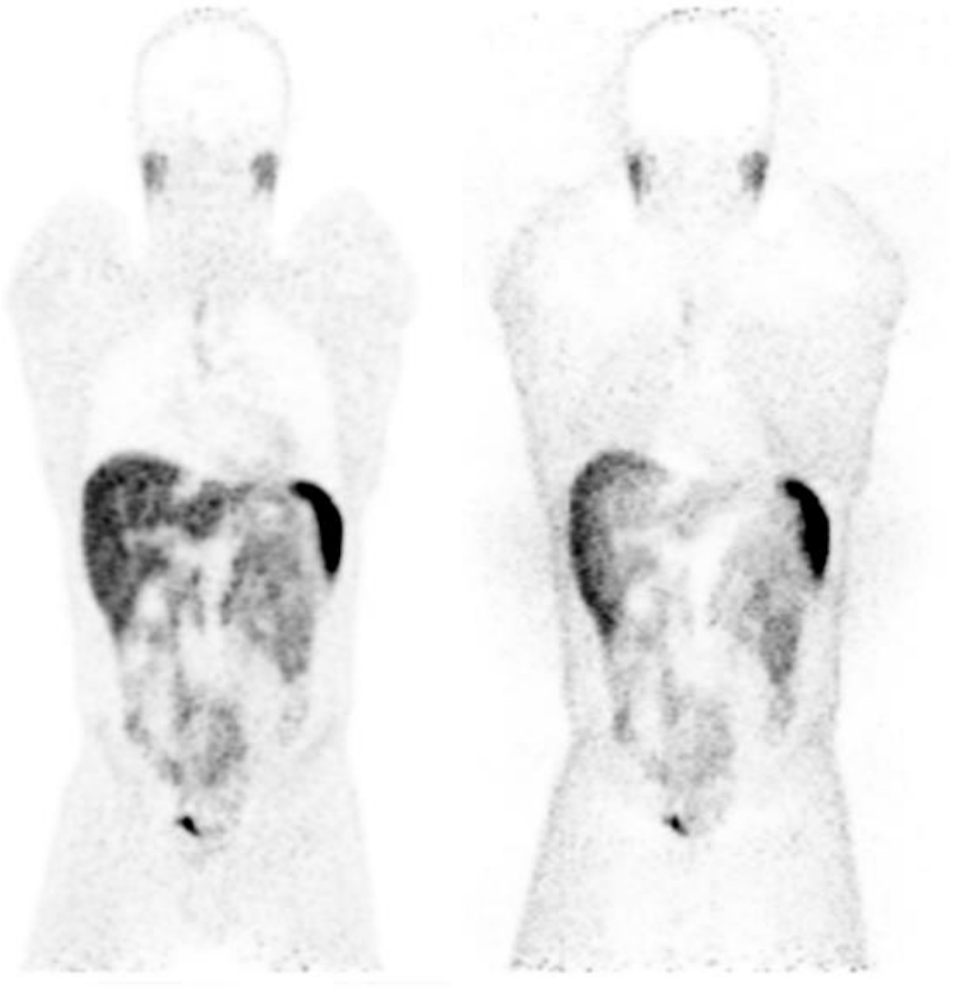

Figure 1. 12 Comparison of the same layer of the patient's body in the PET image with (left) and without (right) attenuation correction. Image obtained courtesy of University Hospital in Kraków.

3.5. Standard Volume Uptake (SUV)

In many areas of life, and even more often in medical imaging, quantitative analysis is required. This may include the necessity of the pixels values evaluation for a given region of interest. This kind of analysis usually relies on the assessment of the boundaries of a given image element in relation to a certain background. The success of such efforts depends on such parameters as image contrast and noise, which are important parameters in quantification.

In PET/CT imaging, not only a qualitative image can be obtained, semi-quantitative data can be obtained also after system calibration [46]. The SUV is used to describe the semi-quantitative data and is calculated using the formula below:

$$\boldsymbol{SUV} = \frac{\boldsymbol{r}}{\boldsymbol{a`/w}} \tag{22}$$

where r is the radioactivity concentration [kBq/ml] measured by the PET scanner within a region of interest (ROI), a' is the decay-corrected amount of injected radiolabeled radiopharmaceutical [kBq], and w is the weight of the patient ([kg]) [46].

The SUV value makes it possible to associate the size (weight) of the patient and the tracer uptake in the marked area. The changes of semi-quantitatively estimated SUV allow to determine the patient's response to the therapy. SUV results are also used in clinical trials of new radiopharmaceuticals [47]. Monitoring of patients' condition and response to treatment is very important, therefore the improvement of image reconstruction algorithms can be very important for quantitative results in PET.

Several types of SUV values can be introduced, depending on the amount of the voxel base adopted [48]:

a) SUV mean - the mean value of voxels from the marked area, for which the standard deviation can also be determined,

b) SUV max - maximum value of a single voxel observed in the marked area,

c) SUV peak - average value from a specific region around the voxel with the maximum value (SUV max).

So far, SUV max is the most frequently used for diagnostic purposes, [48]. The SUV mean value was used in standard measurements performed to produce NEMA Standards using phantoms prepared by the National Electrical Manufacturers Association [49]. SUV PEAK value matters in PET Response Criteria in Solid Tumors 1.0 [50].

In the GE Discovery MI DR PET/CT system, the SUV value is calculated based on the assessment of lean body mass, using biometric data (weight and height) and the patient's sex, whereby the so-called Legacy or Consensus algorithm. The *Legacy* algorithm is set by default [13].

4. Neuroendocrine tumors

4.1. Introduction

The neuroendocrine tumors (NET) account for about 0.5% of all malignancies detected every year in patients. As a rule, the primary exit points of the cancer are: digestive tract (62-67%) and lungs (22-27%) (Tab 1.5) [51]. Gastro-entero-pancreatic neuroendocrine tumors (GEP-NET) are derived from cells of the endocrine system scattered throughout the digestive system. It is a heterogeneous group of tumors, the high diversity of which significantly reduces the diagnostic possibilities in patients [51]. Neuroendocrine tumors are diagnosed at any age, but the risk increases after 50 years of age. Some of them are related to genetic conditions. NETs are usually slow growing and tend to produce and secrete peptides. Some of them are used as tumor markers and may affect the clinical view of the disease. Unfortunately, most tumors are diagnosed at an advanced stage.

Table 1. 5 Frequency, incidence, and survival rates of neuroendocrine tumours [52].

Location	Within Nets [%]	Within GEP-NETs	Incidence SEER [1][/100,000]	Incidence [% of primary site]	5-year OS[2] [%]
GEP-NETs	67		5.25	<2	75-82
Gastric		9-20	0.3	1	45-64
Small intestine		39-42	1.1	37-52	62-71
Appendix		6	0.15	30	90
Colon		9-20	0.35	<1	67
Rectum		26	1.1	<1	90
Pancreas		7-12	0.5-1.0	1-2	27-38
Bronchopulmonary	27		0.46	<2	44-87
Other sites*	6		0.38		

*Esophageal, endometrium, ovary, breast, etc.

4.2. Somatostatin (SST), somatostatin receptors (SSTR) and analogues

Somatostatin is a peptide that plays an important regulatory role by interacting with transmembrane receptors. It is a neurotransmitter and is considered a secretory substance. There are two active biological forms of somatostatin: 14 and 28. Natural somatostatin is characterised by a very short life in the human body (about 3 minutes). Somatostatin also limits the growth

[1] The Surveillance, Epidemiology, and End Results
[2] Overall survival

of cells through a cytostatic or apoptotic mechanisms five subtypes somatostatin receptors can be distinguished: SSTR1-SSTR5, of which SSTR2 has two forms called 2A and 2B [54].

The vast majority of GEP-NETs express somatostatin receptors (SSTR) on the surface, in the cell membrane. The distribution of receptors in neoplastic lesions is usually significantly increased. The mechanisms of receptor overexpression in NETs cells have not been fully elucidated. Neuroedocrine tumors are highly diverse and therefore have the full spectrum of SSTR receptors on their surface. However, type 2 receptors are most often found on the surface of neuroedocrine tumors [54].

Increasing the number of transmembrane receptors in NETs enables their localization in vivo. Unfortunately, the life span of somatostatin in human blood is very short. The research on the analogues began in the early 1980s and resulted in the invention of substances with longer lifetimes allowed the initiation of imaging of NETs using nuclear medicine techniques [54].

4.3. Molecular imaging with radiolabeled somatostatin analogues

The combination of somatostatin analogues with a radioactive isotope enables visualization of the biodistribution of the peptide in the human body. In the first studies, ^{111}In-labeled octreotide analogue was used in SPECT technique. The introduction of this radiopharmaceutical significantly influenced the development of diagnostics of neuroendocrine tumors [54].

However, due to the costs of the ^{111}In isotope and due to the energy characteristics of the emitted gamma radiation, the search for other analogues that could be combined with the ^{99m}Tc isotope was begun. Another significant step was the introduction of chelators enabling the connection of analogues with ^{90}Y and ^{177}Lu and ^{68}Ga isotopes emitting corpuscular, and more precisely – β+, radiation. This solution made it possible to start molecular therapy and improved patient diagnostics due to the higher quality of PET imaging [54].

Considering the technical aspects of the use of somatostatin analogues, several things should be noted. For image reconstruction, detectors need to record sufficient number of coincidence events, and this explains why patients must receive relatively high radiopharmaceutical activity. In PET imaging with ^{68}Ga-DOTA the activity of 100-200 MBq has to be injected. In order to achieve adequate biodistribution of the radiopharmaceutical in the human body and uptake in the tumor, the test is performed after about 60 minutes. Depending on the capabilities of the scanner, the image is obtained with iterative techniques,

sometimes even without the use of the time of flight techniqe. The analysis of the image results is performed by a physician with a specialization in nuclear medicine [55].

4.4. DOTATATE and DOTATOC differentiation

Among the most commonly used SST analogs in PET imaging are DOTATATE and DOTATOC, which are combined with the ^{68}Ga radiometal using the DOTA chelator. There are differences in the affinity between these compounds for particular types of transmembrane receptors:

- DOTATATE has affinity to SSTR 2 and 5,
- DOTATOC has affinity to SSTR 2, 3, 5.

A very important issue is also the stronger affinity of DOTATATE to the second type receptors [56]. These differences can be seen in the clinical PET/CT image. This differentiation can be exploited for personalized patient diagnosis [57].

5. Radiation protection and dosimetry in nuclear medicine

The use of ionizing radiation in diagnostics and therapy in a natural way carries the risk of the dose receiving. The optimization of working conditions results in the reduction of exposure for personnel. It can be easily achieved by the automation of procedures and the application of covers. The dose reduction for the patient is influenced by the half-life of isotopes used in medical procedures and the biodistribution of the tracer in the patient's body. The short lifetimes of the isotopes used in PET diagnostics and their rapid excretion significantly reduce the dose for patients, which makes it possible to perform multiple scans while the patient is being treated. Additionally, low-dose protocols are used in CT imaging. Advances in technology have also made it possible to improve the quality of imaging with the lower activity administered.

The patient doses received from the gallium isotope are approximately 2.1 mSv per 100 MBq of activity administered [56]. Much higher doses are obtained in molecular therapy with the use of isotopes such as ^{90}Y or ^{177}Lu, where it is advisable to perform dosimetry using available imaging techniques [58].

Chapter II

1. Molecular PET/CT imaging at the University Hospital in Kraków

About 400 PET / CT examinations per year are performed at the University Hospital using labeled somatostatin analogs (DOTATATE SSTR 2,5; DOTATOC SSTR 2,3,5). Tests are performed in order to confirm the diagnosis of NETs, qualify for treatment with somatostatin analogues and assess the response to treatment, including Peptide Receptor Radionuclide Therapy (PRRT).

1.1. Materials

The ^{68}Ga radioisotope is obtained from the ^{68}Ge /^{68}Ga generator (Eckert&Ziegler), while somatostatin analogues are purchased in the form of ready-made labeling kits: NETSPOT (DOTATATE), SOMAKIT (DOTATOC) from Advanced Accelerator Applications company (fig. 2.1). Unfortunately, it is currently the only manufacturer of registered medical devices dedicated to the diagnosis of neuroendocrine tumors.

Figure 2. 1 Pictures of Eckert & Ziegler generator and labelling kits (somatostatin analogues) NETSPOT. The kits contain a somatostatin analogue and a buffer solution (UH in Kraków).

In order to meet the requirements of high Good Manufacturing Practice (GMP) criteria, radiopfarmaceutic preparation takes place in a shielded fume cupboard chamber, under sterile conditions (fig. 2.2). There is a negative pressure of 200 kPa in the fume cupboard.

Figure 2. 2 Hot cell for radiolabeling radiopharmaceuticals.

Before injection, the quality of the labeled preparation is checked in accordance with the manufacturer's recommendations [59]. Quality control of radiopharmaceuticals is required for proper biodistribution of the tracer in the patient's body. The appropriate quality of the radiopharmaceutical also affects the patient's safety. Currently, the TLC scanner is used to analyze the quality of the radiopharmaceutical. Sample images from the scanner are shown below (fig 2.3).

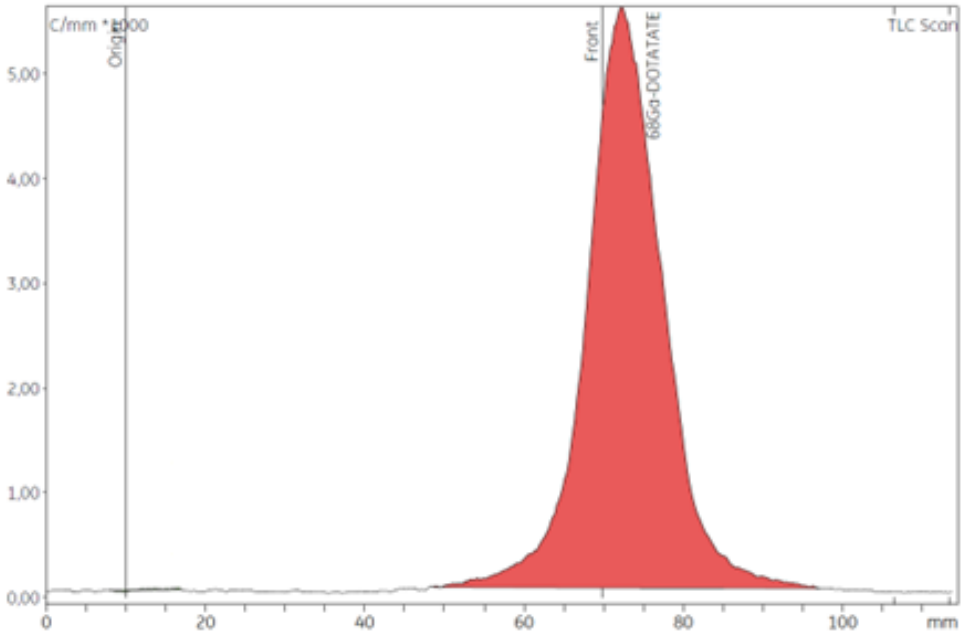

Figure 2. 3 TLC scanner radiograph for labelled somatostatin analogues (68Ga-DOTATATE).

1.2. Patient imaging process

The examination process can be divided into three basic stages: preparation of the patient for the examination, injection of the tracer and imaging. The cooperation of the patient with the medical staff is very important at each stage.

a) **Preparation for the examination**

The patient should be prepared for the examination taking into account the following points:

- in the case of diagnostics using DOTA-peptides, it is recommended to discontinue "cold" somatostatin analogues: short-acting 24-48 hours before the test, and long-acting about 4 weeks before the test, to be ensured that the somatostatin receptor is not blocked;
- the patient must be on an empty stomach and previously used a semi-liquid diet.; previously and still (sometimes) required laxatives before scintigraphy;
- the patient should wear comfortable clothes for the examination, free of metal elements, such as underwires, etc. (this affects the quality of CT imaging).

b) Injection of a radioisotope tracer

For PET/CT, patients receives the activity of approximately 150 MBq in the form of radiolabeled (^{68}Ga) somatostatin analogues in an intravenous injection. The measurement is performed on a Dose Calibrator (ionization chamber) standarized by an accredited laboratory. One hour after the administration of the tracer, the patient is found to have lower activity than the law of radioactive decay, due to the removal of the tracer mainly in the urine.

c) Imaging

Imaging is performed one hour after injection. The standard imaging protocol performs a PET/CT scan of the area from the top of the head to 1/3 of the patient's thighs. In order to limit the impact of bone tissues (additional attenuation), the patient keeps his arms raised. During the examination, 2-dimensional CT imaging (the so-called sagittal and coronal topogram) is performed in order to determine the appropriate range of CT and PET scanning. During the topogram, the density of the medium is also assessed and the appropriate intensity is selected on the X-Ray tube in order to limit the radiation dose from the CT examination. After selecting the appropriate range, PET/CT examination can be performed. After the examination, the patient is allowed to go home. The raw data obtained from PET detectors are processed with an appropriate image reconstruction algorithm. The image will then be described by a physician specialized in nuclear medicine.

1.3. PET/CT imaging systems

At the University Hospital in Kraków, there is a PET/CT Discovery MI DR system (GE Healthcare) in use. The system is equipped with an image reconstruction algorithms available in previous versions of this manufacturer, such as VUE Point HD, VUE Point HD FX. In addition to these reconstruction algorithms, the system also includes the Q.Clear (GE Healthcare) algorithm described in Section 4.3 of Chapter I. The factor in Q.Clear that makes it possible to change the image quality is the beta parameter, which can range from 1 to 10,000. The use of this algorithm was approved by the U.S. Food and Drug Administration (FDA) due to the improvement of the quality and precision in PET/CT imaging [60].

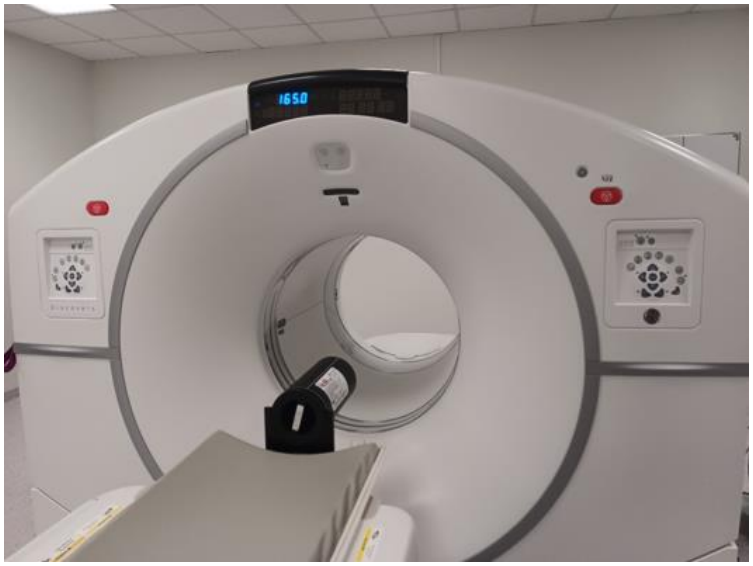

Figure 2. 4 Discovery MI DR (DMI DR). The PET/CT system used in UH in Kraków.

1.4. PET/CT Discovery MI DR

The PET/CT Discovery MI DR system consists of two fully integrated modules: a multilayer computed tomography scanner and a 3D positron emission tomography scanner. The table of the apparatus rests on a specialy designed base that allows transfers into the PET and CT areas of the gantry. The PET detector module consists of an LBS-Lutetium based scintillators with 4.2mm×6.3mm×25mm dimension of each element, where the total number of crystals is 13.824. This results in the sizes of AFOV and TFOV equal to 15.6 cm and 70 cm, respectively. The system uses 1024 of photomultiplier tubes and the time resolution is 549 ps. The value of the temporal window of coincidence is 4.9 ns [61].

1.5. Preparation and verification of the correct operation of the PET/CT system

Calibration of the detector response has to be done to connect the activity in the phantom with the number of counts in the detector. Calibration should be performed periodically as crystal characteristics in terms of sensitivity and energy distribution may vary over time.

Before starting the research, as part of the doctoral dissertation, the readiness of the PET/CT system for operation was verified. All acceptance and operational tests were performed in accordance with the law requirements and the GE company requirements. In order to determine the value of the SUV, a calibration was performed using the Flood Phantom with the ^{18}F fluorine isotope (fig 2.5).

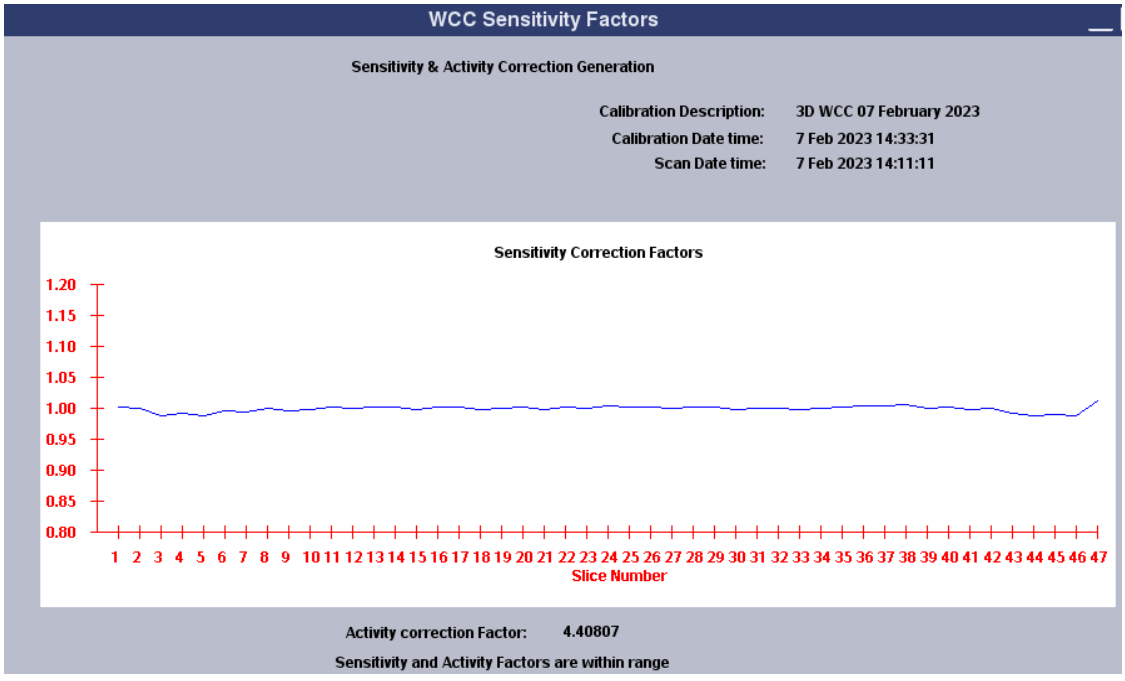

Figure 2. 5 The chart of Well Counter Calibration PET/CT system.

On the day of the study, daily tests were performed with a sealed radioactive source containing $^{68}Ge/^{68}Ga$ isotopes. The tests performed with the source allowed to state that the system is ready for operation (fig 2.6).

Figure 2. 6 Dedicated source $^{68}Ge/^{68}Ga$ for quality control of PET/CT system.

2. Fantom imaging

2.1. Phantom description

In order to determine the impact of the Beta on image quality, I decided to perform tests using the NEMA IEC phantom (Biodex, PET Phantom) which is recommended for use in the evaluation of reconstructed image quality in whole body PET imaging. The NEMA phantom consists of three main parts:

a) body part,

b) lung insert,

c) 6 spheres of different sizes that can be refilled from the outside of the phantom.

The possibility of filling the spheres from outside allows for the achievement of other radioisotope concentrations in the body parts the phantom and spheres. Taking into account the phantom studies in the conducted analysis allows to determine the change of the SUV value for the known concentration of the ^{68}Ga isotope. This further allows a reliable assessment, without the tracer uptake being influenced by pathological changes in patient body.

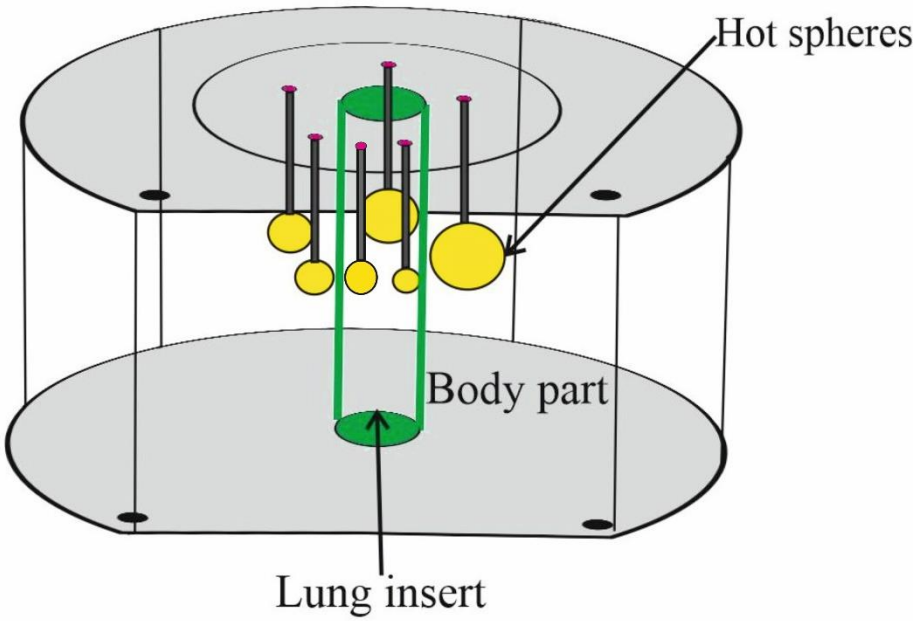

Figure 2. 7 Scheme of the NEMA IEC Phantom.

The study employed the NEMA IEC Body Phantom (Biodex, USA) consisting of the body part and 6 spheres which were independently filled (figures 2.7 and 2.8). The phantom spheres have the following volumes [ml] and diameters [mm]: 0.5/10 ; 1.2/13; 2.6/17; 5.6/22; 11.5/27; 26.5/37 [ml/mm] [62]. The different diameters of spheres in the phantom allow to simulate any organ or anatomy with increased uptake.

Figure 2. 8 The NEMA phantom on the PET/CT Discovery MI DR system table.

2.2. Description of the experiment

For the purposes of this study, the body part and all six spheres were filled with ^{68}Ga isotope. In order to obtain a solution, which was then introduced into the spheres, a separate vessel (beaker) was used. The vessel contained 100 ml of water into which an netto value activity of 6.11 MBq was introduced. The activity in the syringe was measured before and after filling. In order to limit the loss of activity, the syringe was additionally rinsed with water from the vessel. The solution prepared in this way was then introduced into the spheres, which allowed to obtain the same isotope concentration in all spheres First, the spheres were filled in accordance with the manufacturer's recommendations and the principles of radiological protection (much more activity was introduced to the body part). Replenishing of the spheres requires precision and is time consuming. The long fill time of the spheres resulted in a reduction in the assumed amount of activity that was introduced into the body part in order to maintain a concentration ratio of 1:4 (Tab. 2.1). This ratio allows for precise isolation spheres from the background, resulting in more accurate SUV mean values. 90% of the body parts of the phantom volume was filled with water. The isotope of netto value activity equal to 140.57 MBq was then introduced and mixed. Then, water was added to fill up the whole phantom volume carefully to avoid the formation of an air bubbles inside the phantom. The activity introduced to the phantom made it possible to obtain a homogeneous image of the whole phantom. Information about the phantom contained total activity (58.4 MBq) and time when the phantom preparation was done were entered into the system. The total activity was the sum of the activities in the spheres and the body part after taking into account the decay accordingly to the law of radioactive decay. The introduction of additional time resulted from the fact that the measurements of the empty and full syringe activity for two independent parts (sphere and body part) were made at a certain time interval. The data were taken as the starting point for further evaluation, i.e. the difference between the recorded time and the time of imaging.

The gallium isotope concentration ratio in the body part and the spheres was almost 1:4, in accordance with NEMA NU 2-2018 recommendations for Image Quality Measurement tests [62].

Table 2. 1 Planned and actually introduced activities to the NEMA phantom along with calculated concentrations.

	Total volume [ml]	Theoretical activity [MBq]	Teoretical Concentration [kBq/ml] and ratio Body to Spheres	Actual activity [MBq]	Measurement time	Real concentration [kBq/ml] and ratio Body to Spheres (16:28)
Body	9700	150	15.38 1	$\boldsymbol{A_0 = 140.6}$	16:26	14.05 1
				$\boldsymbol{A_e = 0.03}$	16:27	
				$\boldsymbol{A_{inj} = 140.6}$	16:27	
Spheres	47.82	3	62.73 4	$\boldsymbol{A_0 = 6.5}$	16:15	53.44 3.8
				$\boldsymbol{A_e = 0.39}$	16:17	
				$\boldsymbol{A_{inj} = 5.97}$	16:17	

A_0 – activity before injection, A_e – residual activity in syringe , A_{inj} – activity injected to spheres or body part of the phantom

Imaging was performed with the use of PET/CT Discovery MI DR device (GE Healthcare, USA). The system is currently in clinical use with the regular quality control tests and inspections performed, in accordance with the binding regulations.

2.3. Imaging

In total, three PET/CT scans were performed 1h 8 minutes, 2h 1 minutes, 2 h 26 minutes after recorded time. The imaging was made on two beds: 3 minutes for each. Each time, the spheres were placed in the same position (no phantom movement) with the constant values of the table setting (height, table co-ordinates). The data for the analysis were always used from the same image layer for spheres (system coordinates - I113.2) and body part (system coordinates - I185.2). The imaging parameters used correspond to the current protocol in the clinically used PET/CT system. Because in clinical practice, various radiopharmaceutical activities can be used in a much larger volume and the patient's imaging takes place about 1 hour after the injection, several scans were performed after different time to verify the system's response. For the conducted research, it was important to verify the response for a low level of activity, hence the delay in the start of imaging in relation to the time of injection of the isotope into the phantom.

2.4. Image reconstruction

The obtained phantom raw data were reconstructed with the use of the VP FX+Q.Clear and VP HD+Q.Clear alghoritms, with a retrospective technique for diverse values of the β parameter, ranging between 150 and 950, with steps every 100. The range was selected due to the literature data and indications of the manufacturer of the system. Subsequent reconstructions were used:

a) VUE Point HD+Q.Clear, beta parameter 150 – 950,
b) VUE Point FX+Q.Clear, beta parameter 150 – 950.

All images were taken with the same study protocol using the option in the next series system in reconstruction process. This solution allowed to avoid geographical errors in the location of layers in the phantom image. The images were assessed on the same layer of the sphere on I113.2 and the body on I185.2. A weight of 10 kg was entered into the system as a patienr`s weight (the system rounds the patient's weight, the original weight was assumed to be 9.8 kg). The phantom was imaged with the protocol that is used to image the patient (the number of beds was reduced to 2). All analyzes were collected from strata within 1 bed, bed linking occurred below the spheres. Raw LIST mode data was used to reconstruct the image. Phantom imaging was performed using a standard patient PET/CT protocol with DFOV 70 cm, 256x256 matrix size, and 3 minutes per bed position.

3. Results

3.1. Body part of the phantom

3.1.1. Visual assessment

3.1.1.a Analysis

The simplest assessment is the visual rating, which allows a rough estimation of image quality. It is usually the first step in evaluating the image quality of the phantom. Such analysis, however, is influenced by a high level of recipient subjectivity and may be disturbed due to the lighting in the room, the monitor settings and quality, on the matrix size on which the image is displayed and the observer visual impairments. The visual assessment of quality in the first step was made on the basis of the image of the body part (figures 2.9-11).

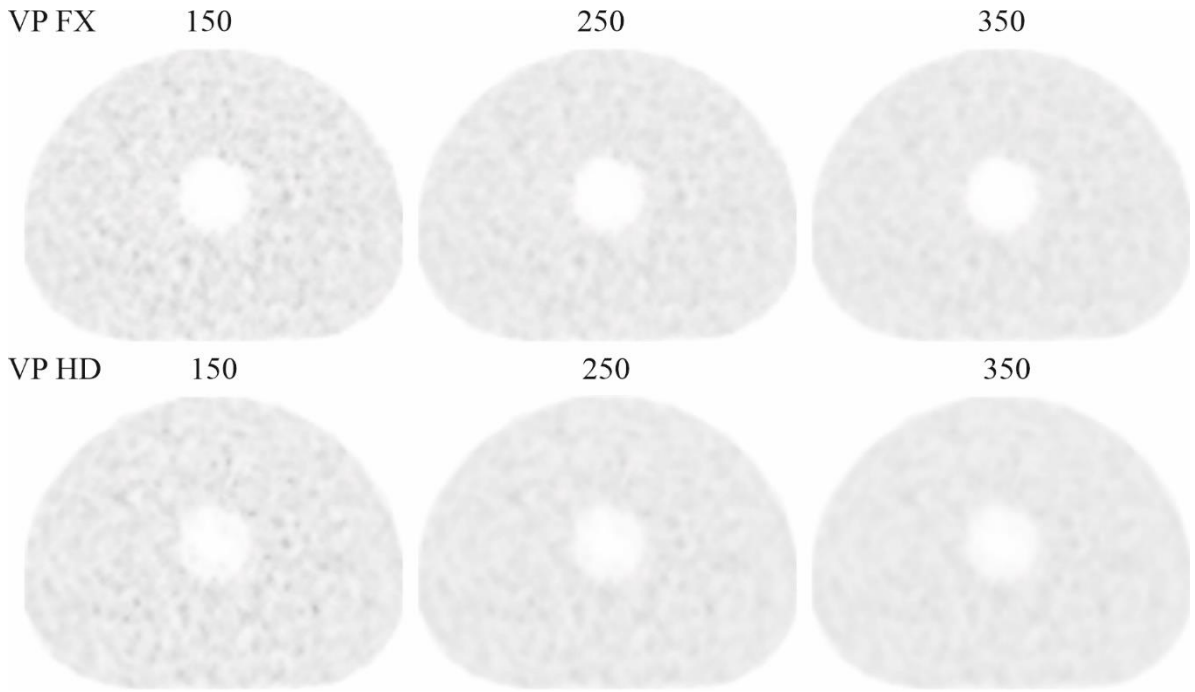

Figure 2. 9 NEMA Body Phantom with ^{68}Ga isotope reconstructed with the Q.Clear algorithm. The effect of application of different Beta parameter values (from the left, respectively): 150, 250, 350 (VP FX/VP HD+Q.Clear). The acquisition was performed 1 h 8 minutes after recorded time.

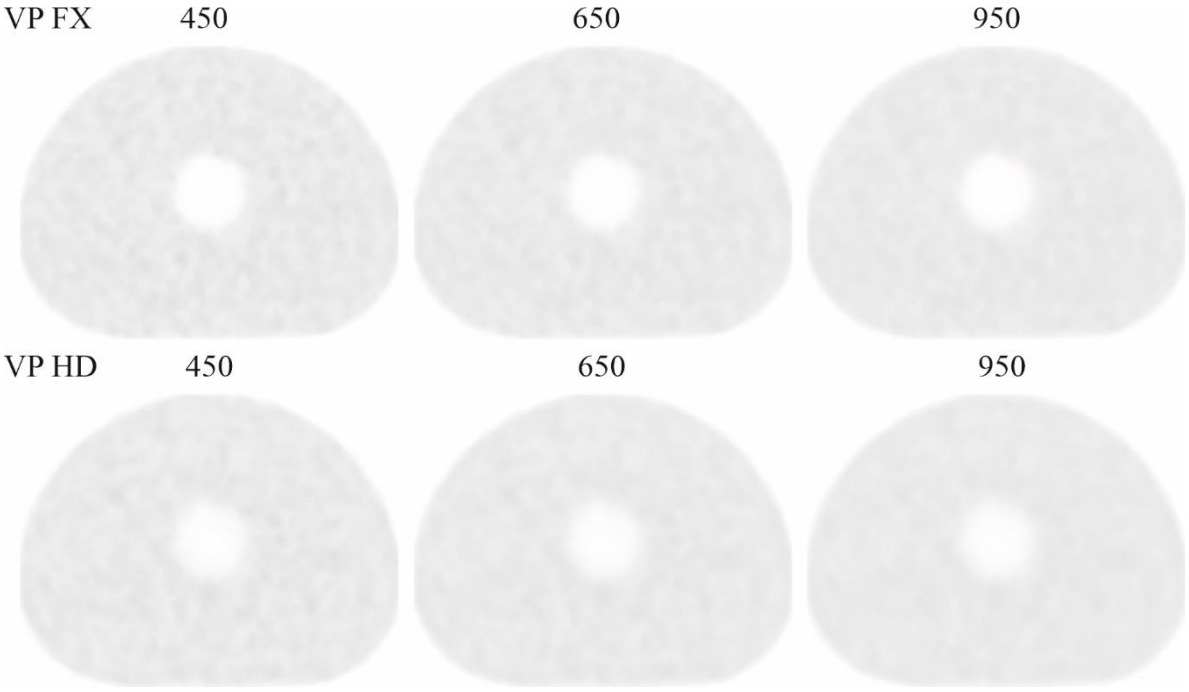

Figure 2. 10 NEMA Body Phantom with ^{68}Ga isotope reconstructed with the Q.Clear algorithm. The effect of application of different Beta parameter values (from the left, respectively): 450, 650, 950 (VP FX/VP HD+Q.Clear). The acquisition was performed 1 h 8 minutes after recorded time.

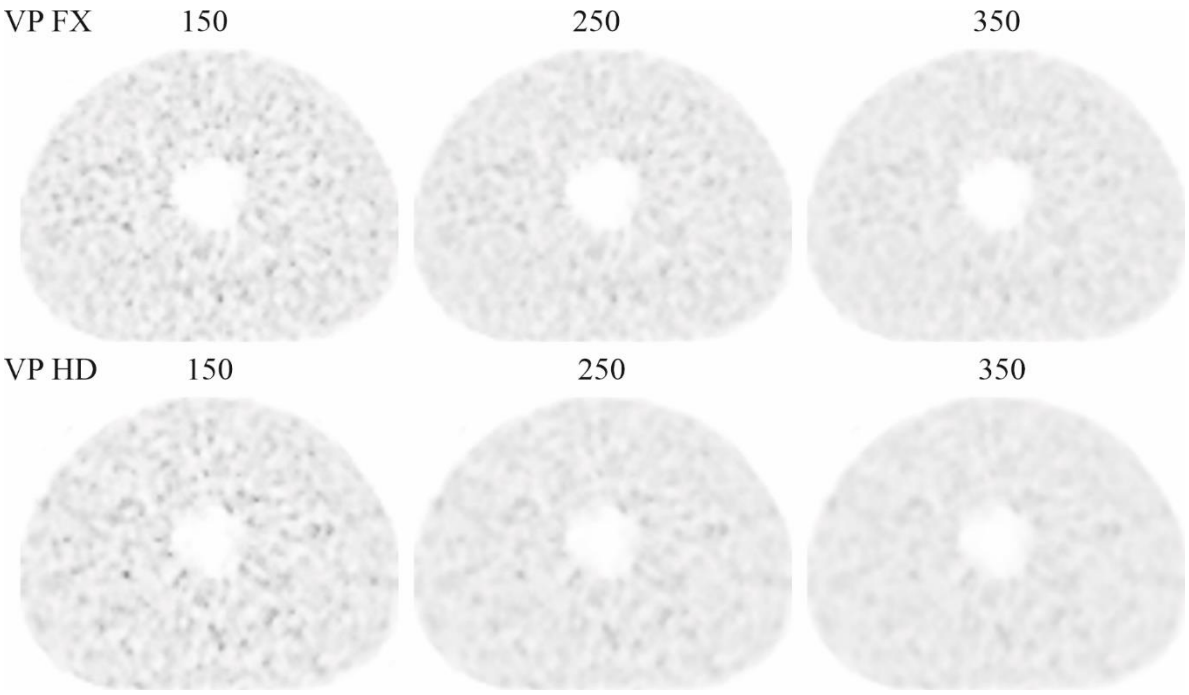

Figure 2. 11 NEMA Body Phantom with ^{68}Ga isotope reconstructed with the Q.Clear algorithm. The effect of application of different Beta parameter values (from the left, respectively): 150, 250, 350 (VP FX/VP HD+Q.Clear). The acquisition was performed 2 h 26 minutes after recorded time.

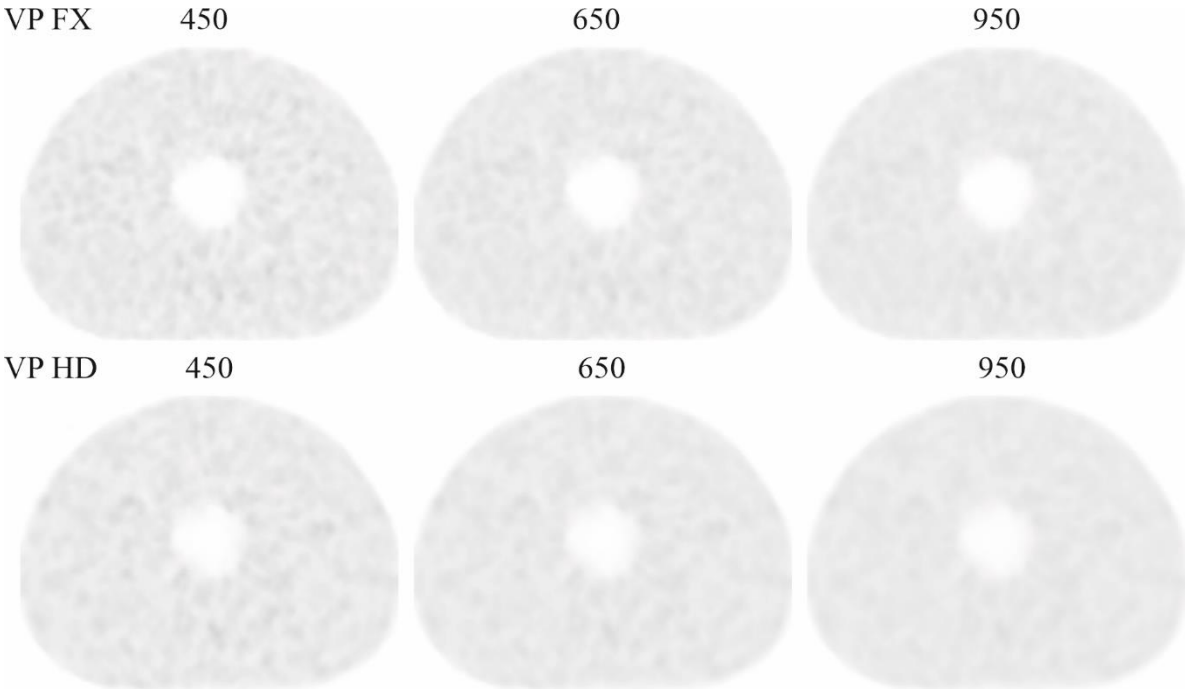

Figure 2. 12 NEMA Body Phantom with ^{68}Ga isotope reconstructed with the Q.Clear algorithm. The effect of application of different Beta parameter values (from the left, respectively): 450, 650, 950 (VP FX/VP HD+Q.Clear). The acquisition was performed 2 h 26 minutes after recorded time.

3.1.1.b Discussion

The obtained images of the same phantom layer at two time points (1h 8 min and 2h 26 min after recorded time) show a lower image quality for lower values of the beta parameter. The image of the phantom should be homogeneous and should have a constant gray level. At the same time, it can be stated that at lower activity content (after 2h 26 min) a satisfactory background image quality occurs at higher values of the Beta parameter. Visual assessment shows that a similar image quality at Beta equal to 250 (after 1 h 8 min) occurs at 450 after 2 h 26 min, with the image being more noisy (less homogeneous) in the VP HD + Q.Clear reconstruction.

3.1.2. Minkowski analysis - quantitative image analysis

3.1.2.a Analysis

The subjective assessment of the obtained images quality presented above was the preliminary step of the analysis, before the main and most important stage, which is the quantitative analysis. For the obtained two-dimensional (2D) grayscale images, a quantitative assessment was carried out using Minkowski's measures. In the case of 2D images the surface coverage (F), curvature of distinct objects (U), and density of observed objects (χ_E) are the most obvious quantitative measures. Phantom images can be treated as arrays of pixels characterized by various gray levels. Each pixel can be assigned either as white or as black depending on whether its value is larger or lower than the threshold. Using the threshold gray level as the variable each 2D image (subsequent layers of the whole study series) can be transformed into a series of black-and-white images (so called level contours). Then the values of Minkowski functionals (F, U and χE) can be determined for each level contour. Such a threshold procedure results in the plots of the Minkowski measures against the threshold variable [GUT, RAC03]. This approach is used, inter alia, in the evaluation of inhomogeneous polymer layers imagined as grayscale images [63, 64]. In the case of Phantom PET/CT images, plots of the surface coverage F against the gray level may be applied to assess quantitatively the quality and homogeneity of the image. The analysis was carried out for one selected layer, without spheres imitating hot spots, for low and very low concentration of the ^{68}Ga isotope (scans after 1 h 8 min, 2h 1 min, and 2h 26 min after recorded time). The example images analyzed this way are shown in fig. 2.13 while the result of surface coverage F analysis for the whole extend of beta values for particular measurements is presented in fig. 2.14.

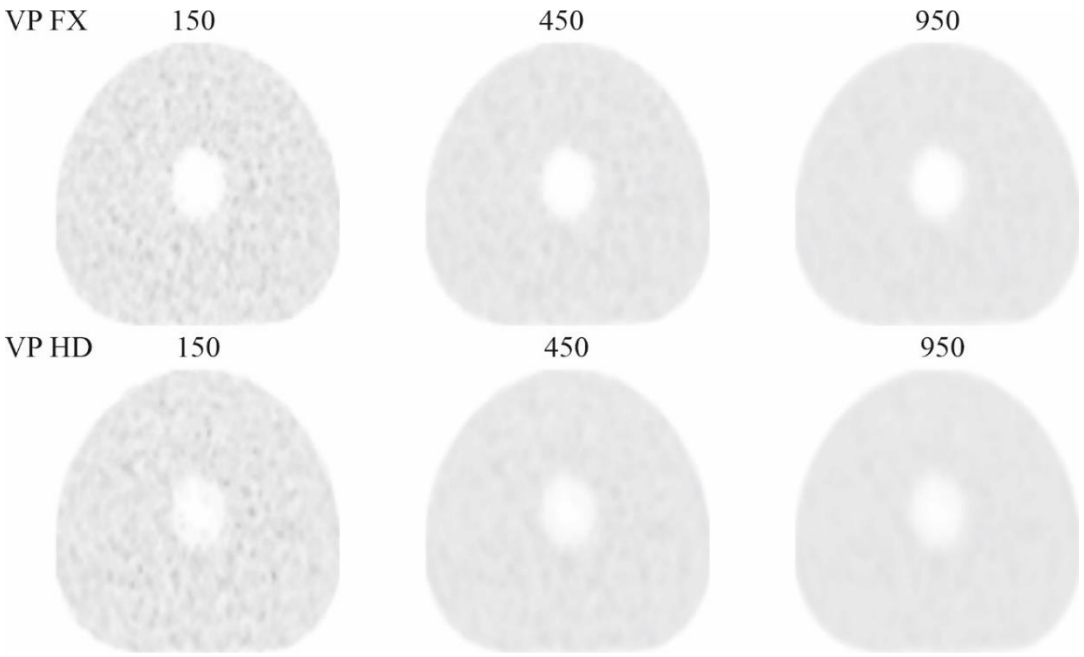

Figure 2. 13 The examples of the processed NEMA body phantom images used for Minkowski's analysis (1h 8 min, VUE Point FX, HD). From the left, an image for the Beta parameter of 150, 450, 950.

It was assessed that the more heterogeneous the picture, the wider the range of gray scale levels for-which the value of the Minkowski coefficient decreases (Graph 2.1-6).

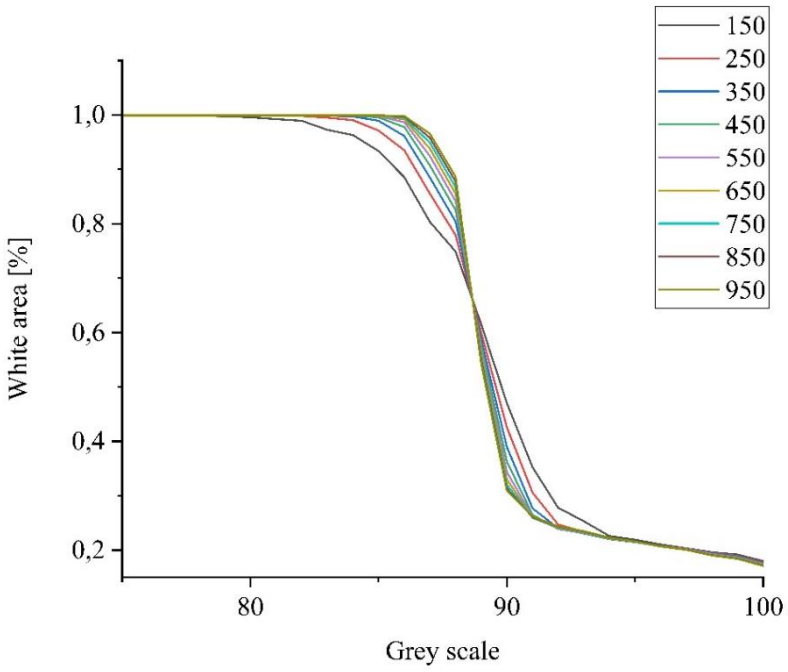

Graph 2. 1 Change of the amount of white area for different values of the Beta parameter (VP FX+Q.Clear). The acquisition was performed 1h 8 min after recorded time (beta parameter 150 – 950, 1st measurement).

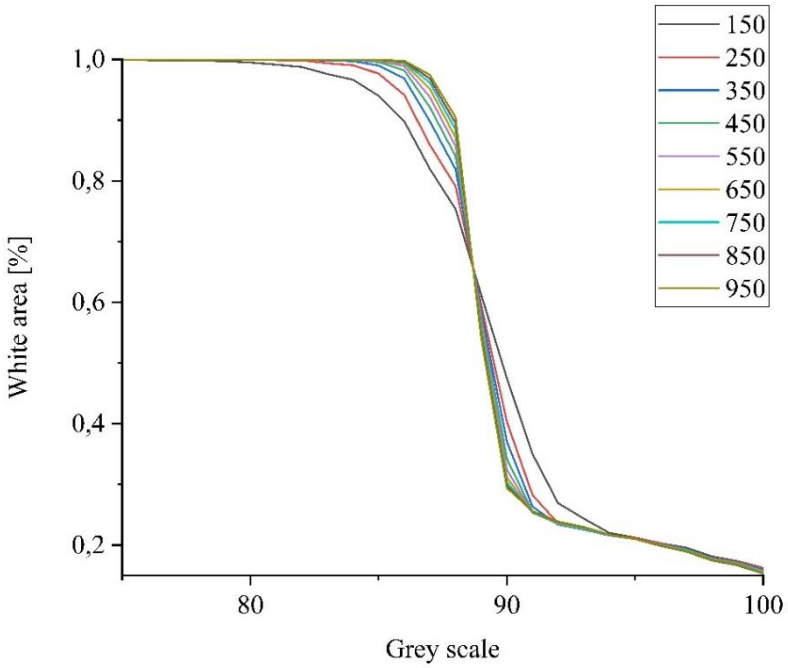

Graph 2. 2 Change of the amount of white area for different values of the Beta parameter (VP HD+Q.Clear). The acquisition was performed 1h 8 min after recorded time (beta parameter 150 – 950, 1st measurement).

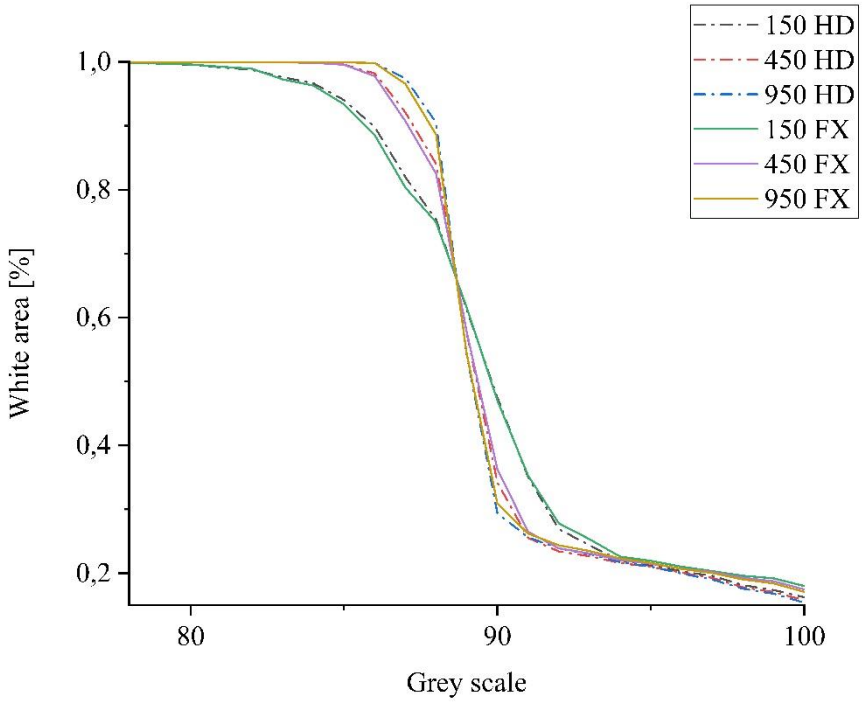

Graph 2. 3 Change of the amount of white area for different values of the Beta parameter: 150, 450, 950 (VP HD/VP FX+Q.Clear). The acquisition was performed 1h 8 min after recorded time (1st measurement).

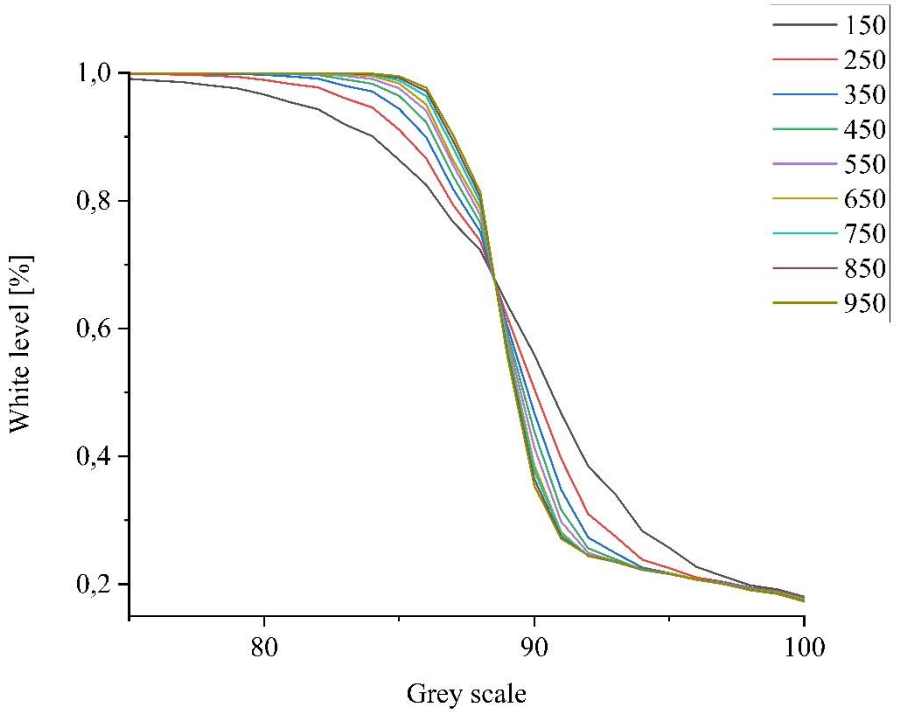

Graph 2. 4 Change of the amount of white area for different values of the Beta parameter (VP FX+Q.Clear). The acquisition was performed 2h 26 min after recorded time (beta parameter 150 – 950, 3rd measurement).

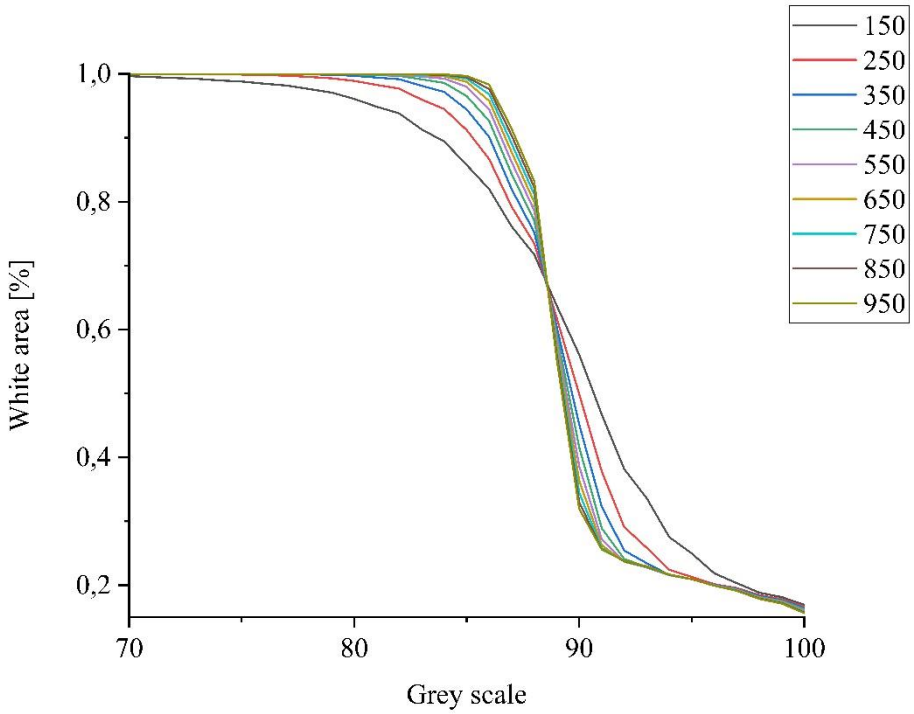

Graph 2. 5 Change of the amount of white area for different values of the Beta parameter: 150, 450, 950 (VP FX+Q.Clear). The acquisition was performed 2h 26 min after recorded time (3rd measurement).

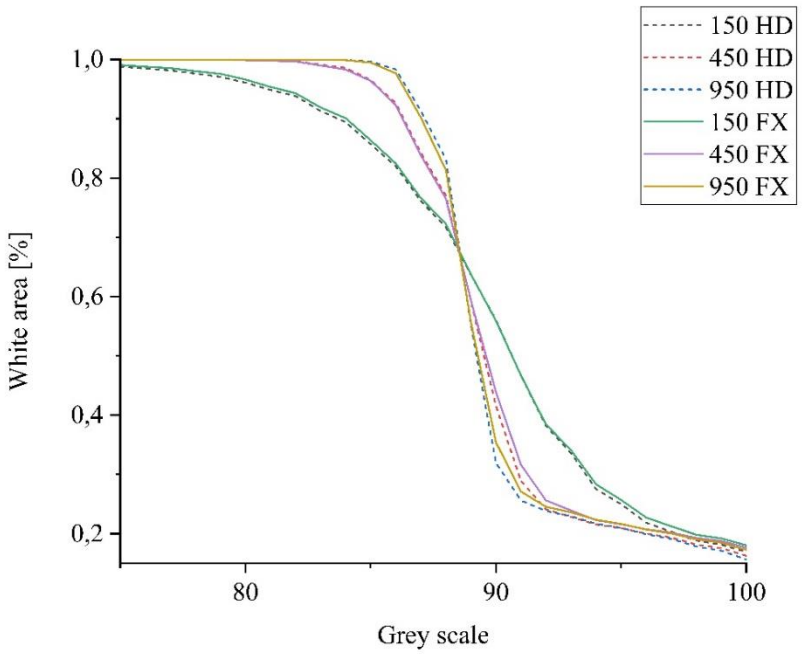

Graph 2. 6 Change of the amount of white area for different values of the Beta parameter 150, 450, 950 (VP FX/VP HD+Q.Clear). The acquisition was performed 2h 26 min after recorded time (3rd measurement).

The obtained surface coverage versus threshold functions were then differentiated allowing the calculation of a minimum which parameters characterized quantitatively the image grey scale variability (Graph 2.7). It was possible by fitting a reversed Gaussian curve to the obtained derivative function in order to get the half-width (FWHM) of the distribution. The FWHM value obtained from the Gaussian peak describes quantitatively the variability present in the obtained layer of the PET image. The values of FWHM for different Beta parameters in reconstructions VUE Point FX/HD+Q.Clear presented in Tables 2.2 and 2.3. A graphical presentation of FWHM variability depending on the Beta value, reconstruction and measurement time is presented in the Graph 2.8.

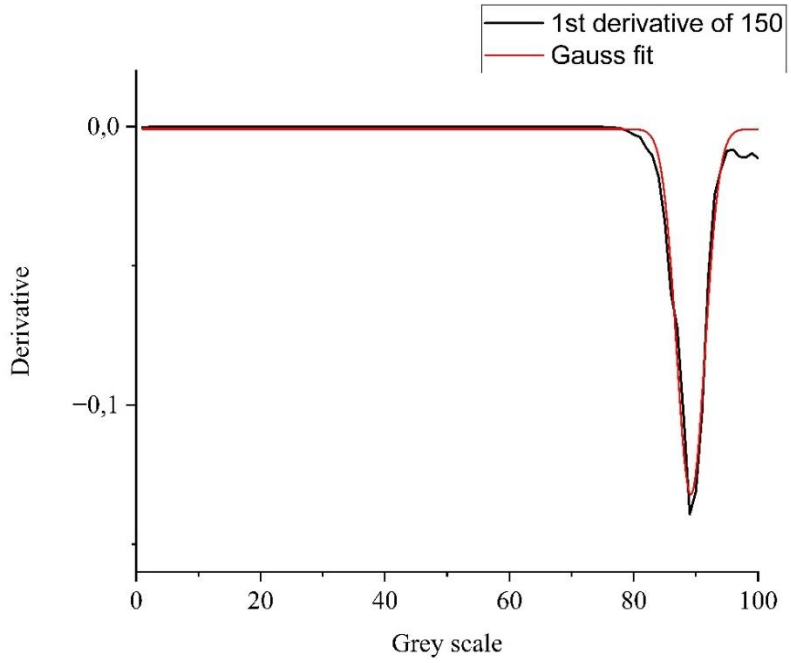

Graph 2. 7 A Gaussian curve fitted to F plot was used for the analysis. The acquisition performed 1 h 8 min after recorded time (VP HD+Q.Clear, 150 Beta parameter).

Table 2. 2 Values of FWHM for different Beta parameters (VUE Point FX+Q.Clear).

Beta	FWHM1	SD FWHM1	FWHM2	SD FWHM2	FWHM3	SD FWHM3
150	5.56	0.14	7.39	0.15	8.35	0.36
250	4.30	0.08	5.49	0.10	6.21	0.28
350	3.60	0.06	4.55	0.08	5.39	0.10
450	3.16	0.05	3.99	0.07	4.67	0.09
550	2.88	0.04	3.59	0.06	4.18	0.08
650	2.69	0.04	3.30	0.06	3.77	0.08
750	2.55	0.03	3.09	0.05	3.54	0.06
850	2.44	0.03	2.93	0.04	3.32	0.06
950	2.36	0.03	2.93	0.04	3.15	0.05

Table 2. 3 Values of FWHM for different Beta parameters (VUE Point HD).

Beta	FWHM1	SD FWHM1	FWHM2	SD FWHM2	FWHM3	SD FWHM3
150	5.39	0.11	6.79	0.31	9.39	0.19
250	3.89	0.09	4.94	0.21	6.33	0.14
350	3.28	0.06	4.22	0.08	5.03	0.11
450	2.89	0.05	3.63	0.06	4.26	0.10
550	2.66	0.04	3.24	0.05	3.60	0.21
650	2.50	0.03	2.99	0.05	3.25	0.18

750	2.39	0.03	2.70	0.08	2.95	0.18
850	2.27	0.05	2.56	0.07	2.80	0.14
950	2.18	0.04	2.46	0.07	2.69	0.13

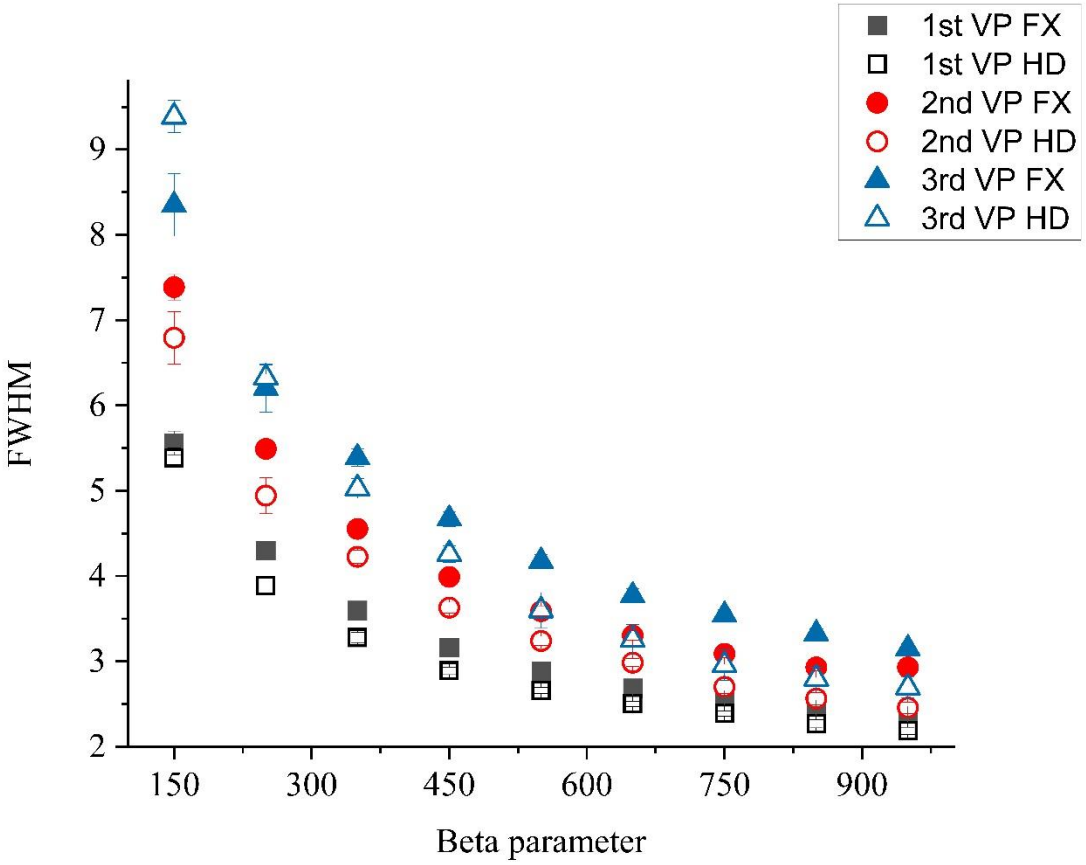

Graph 2. 8 Comparison of the FWHM results depending on the value of Beta parameter in three different time points.

3.1.2.b Discussion

With the increase of the beta, the FWHM decreases, which describes the dependence of the degree of opacity of pixels in the image assigned as the black and white in Minkowski binarization. A similar trend can be observed in each measurement when consider the reconstruction algorithm, with the FWHM parameter being highest for the VP FX + Q.Clear reconstruction. The fastest decrease in FWHM, i.e. an increase in phantom homogeneity, can be observed in the range of 150 – 350 for the Beta parameter. The amount of the white area increases with the decrease in activity in the body part of the phantom, which indicates a decrease in the concentration of the radiopharmaceutical and homogeneity in the phantom. At low activities, an increase in the Beta parameter for the phantom body area is beneficial as it leads to a more homogeneous image of the phantom.

The conducted quantitative analysis allows to assess accurately the variability of the FWHM in the image connected to the variability of the activity concentration in the body part and the Beta value. The quantitative analysis confirms the previous qualitative discussion. Similarly to visual evaluation, as activity decreases, we observe that the Beta also increases in order to achieve adequate image homogeneity. At the time points 1h 8min, 2h 1min, 2h 26min, similar FWHM values are obtained for the Beta parameter of 350 (3.6), 550 (3.59) and 750 (3.54) in the VP FX + Q.Clear reconstruction. A similar trend is observed for the reconstruction of VP HD + Q.Clear, but the dependence of the FWHM change on the Beta parameter is lower for lower isotope activity concentrations – similar FWHM results, i.e. 3.24 and 3.25, occur at the Beta parameter values of 550 (2h 1min) and 650 (2h 26 min) respectively.

It can be assumed that the reduction of the statistics of counts connected to lower activity or shortening the bed time by 30% (e.g. from 3 minutes to 2 minutes), should be compensated by the increase in Beta value in order to keep the quality of the obtained homogeneous images.

3.1.3. SUV measurement of the body part

3.1.3.a Analysis

In accordance with NEMA standards, 60 representative ROIs were selected for each background (bcg) measurement of SUV max and SUV mean, for which finally the global SUV mean and global SUV max (mean value of SUV max from 60 ROIs) was estimated (fig. 2.14, graph 2.9, 2.10). The average and maximum activity concentration values were also determined. For this measurement, 60 circular ROIs with an area about 300 mm^2 each were selected (12 for each layer) (fig. 2.14).

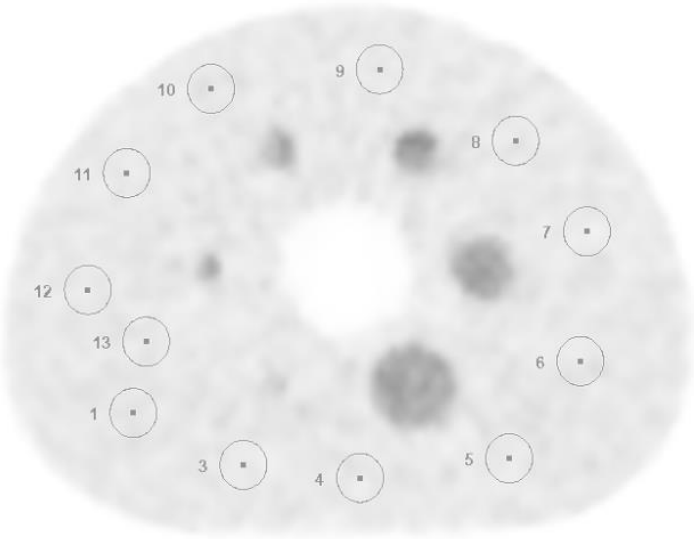

Figure 2. 14 ROI selected to SUV mean, SUV max, max and average concentration in bcg.

The layer on which measurements were made with spheres and two layers above and two below were used. In order to obtain the SUV peak value and activity concentration, 20 cuboidal ROIs with a volume of 12 cm^3 were additionally defined as peak value (fig. 2.15). As for the SUV mean and max values, the average SUV peak value was also determined (fig 2.11). These data were then analyzed for variability at beta values of 350-950, as well as in the analysis of the results for spheres with increased concentration. The beta range was selected after consultation with experienced physicians, for whom background images in the range of 150 – 250 were too low quality.

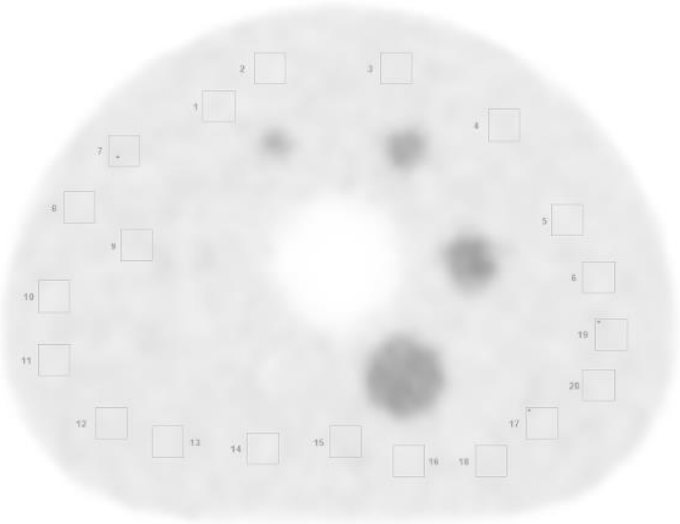

Figure 2. 15 ROI selected to SUV peak, and concentration peak value of the background estimation.

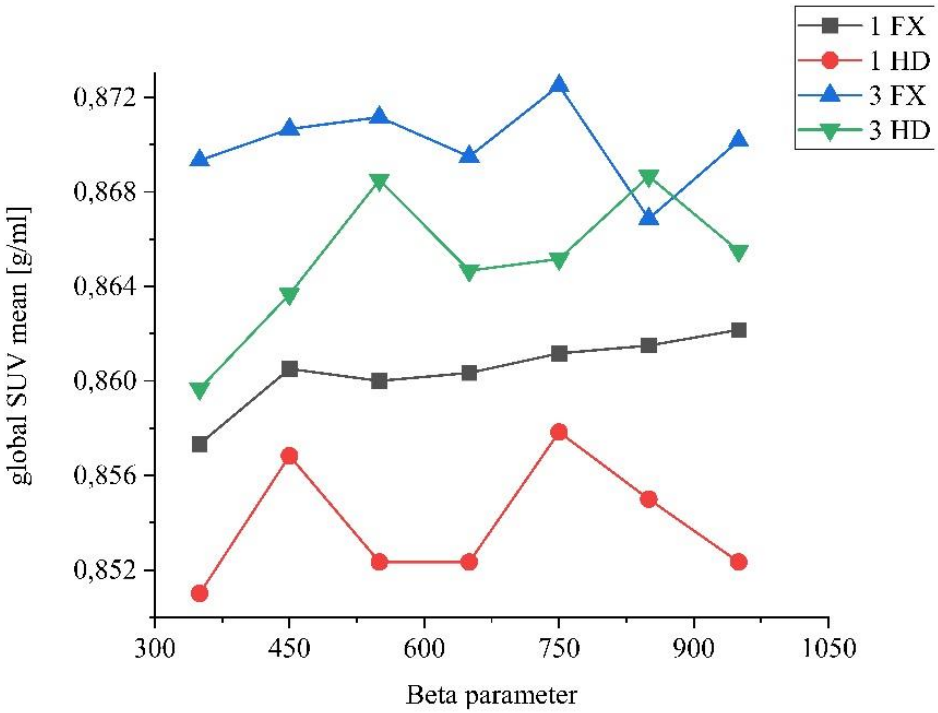

Graph 2. 9 Dependence of global SUV mean values for the body part of the NEMA IEC Body Phantom for the beta ranged 350-950, 1h 8 min and 2h 26 min after recorded time (VUE Point FX/HD).

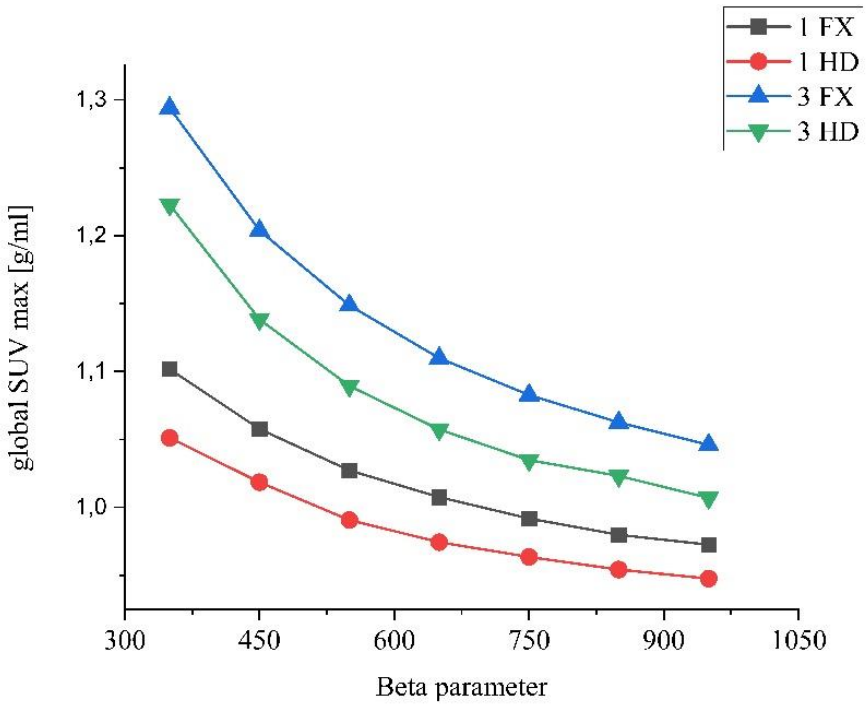

Graph 2. 10 Dependence of global SUV max values for the body part of the NEMA IEC Body Phantom for the beta ranged 350-950, 1h 8 min and 2h 26 min after recorded time (VUE Point FX/HD).

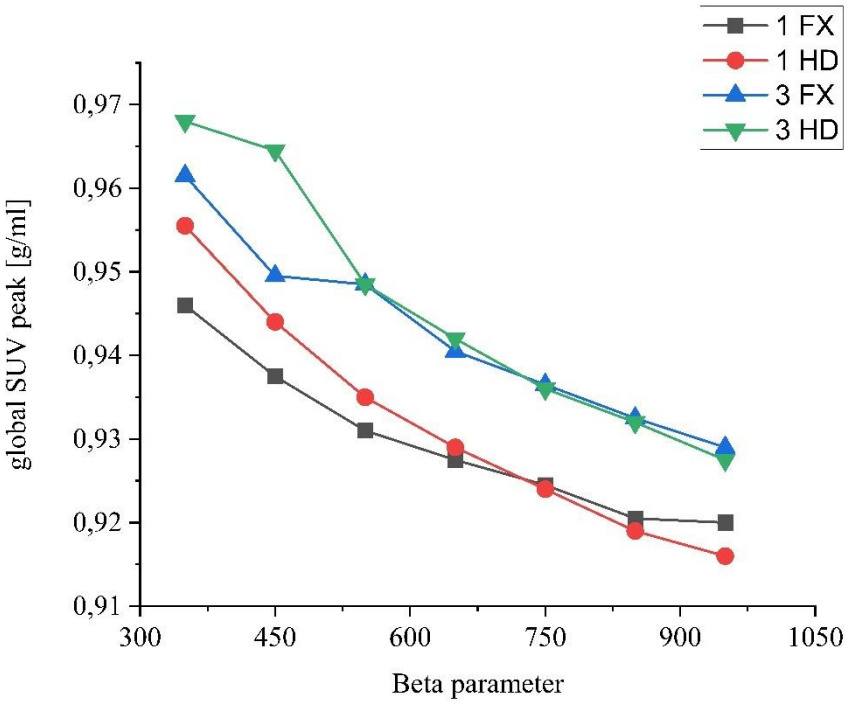

Graph 2. 11 Dependence of global SUV peak values for the body part of the NEMA IEC Body Phantom for the beta ranged 350-950, 1h 8 min and 2h 26 min after recorded time (VUE Point FX/HD).

3.1.3.b Discussion

Reconstructed images have higher SUV mean and max values for lower radiopharmaceutical concentrations (3rd measurement) and for time-of-flight reconstruction. For a homogeneous phantom, an increase in the value of SUV mean can be observed, which would mean that the homogeneity of the phantom increases with the increase in the value of SUV mean. It can also be observed that there is observed parallely a significant decrease in the value of SUV max. The SUV max value is the value of individual pixels in the image. An increase in the SUV mean and a decrease in the SUV max may mean that the "grain" level in the image decreases and the measured values for individual pixels are becaming a higher values.

3.1.3.c Summary of body part

The performed analysis showed that for the body part of the phantom, it is beneficial to increase the value of the Beta in order to obtain a homogeneous distribution. This allows to lower the SUV max and peak values without deterioration of the SUV mean value. This means that increment of the Beta value for a large, homogeneous object produces also a more homogeneous image. However, there is a dependence of the Beta value adjustment on the activity concentration in the phantom, the smoothing effect is achieved faster for higher activities (with a lower beta parameter). There is also the dependence on the image reconstruction algorithm used. For higher concentration, the effect of increasing image homogeneity is similar for VP FX+Q.Clear and HD+Q.Clear, with a decrease in isotope concentration. A greater difference between the algorithms becomes visible in favor of VP FX+Q.Clear. This means that the value of the Beta should be adjusted not only to the isotope used, but also to the type of reconstruction algorithm used. Higher Beta values should be considered for VP HD+Q.Clear.

A worrying signal, however, is the decrease in the value of SUV max for a homogeneous phantom in further analysis, as it may mean that the increase in Beta will also reduce the value of SUV max in hot spheres.

3.2. Spheres

3.2.1. Visual assessment of the visibility of the spheres

3.2.1.a Results

Similar to the body part study, a visual assessment of the image quality for the spheres was made. The visibility of all spheres (1-6) and their quality (if their shape is reconstructed properly), were taken into account. The level of visibility of the spheres at different times from the isotope injection for two reconstructions VP FX and VP HD was also compared (fig 2.16-2.17.

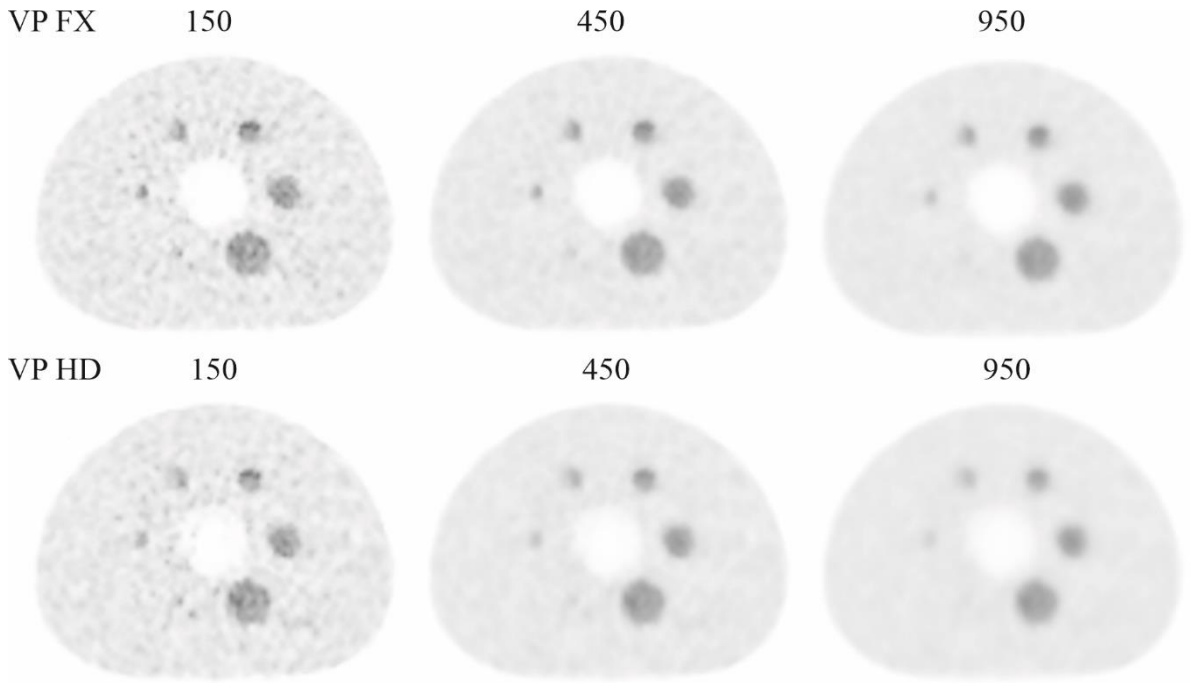

Figure 2. 16 NEMA Body Phantom with ^{68}Ga isotope reconstructed with the Q.Clear algorithm for the Beta parameter from the left, respectively: 150, 250, 350 (VP FX, VP HD) 1h 8 minutes after recorded time.

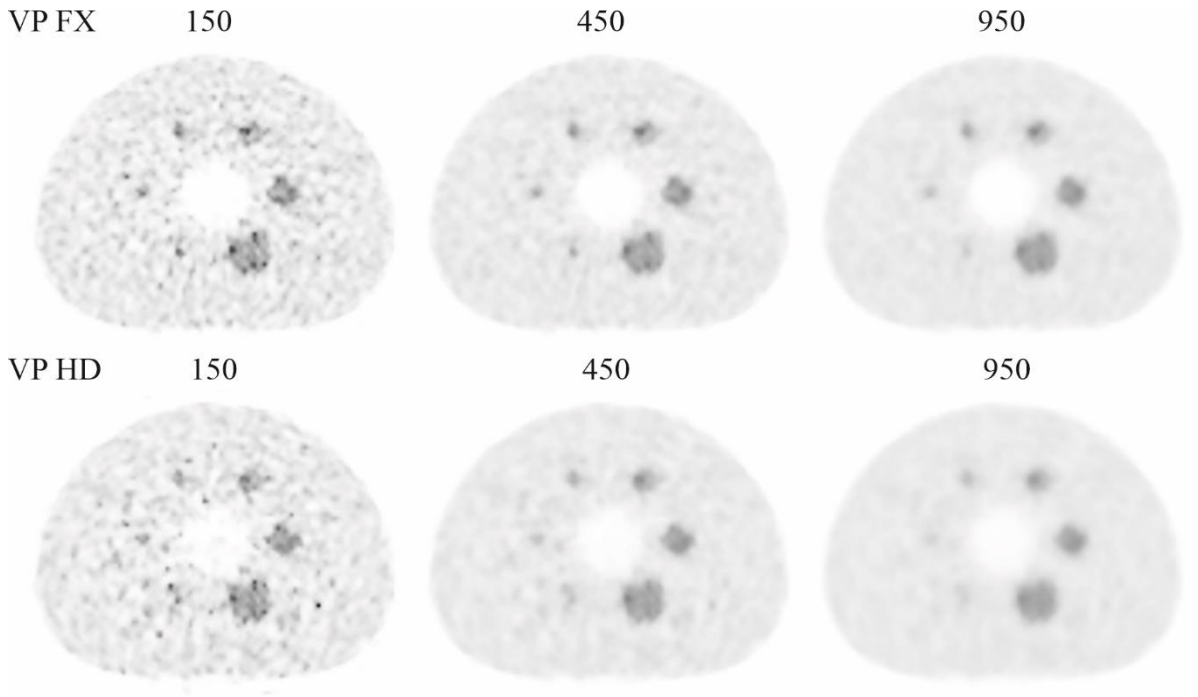

Figure 2. 17 NEMA Body Phantom with ^{68}Ga isotope reconstructed with the Q.Clear algorithm for the Beta parameter from the left, respectively: 150, 250, 350 (VP FX, VP HD) 2h 26 minutes after recorded time.

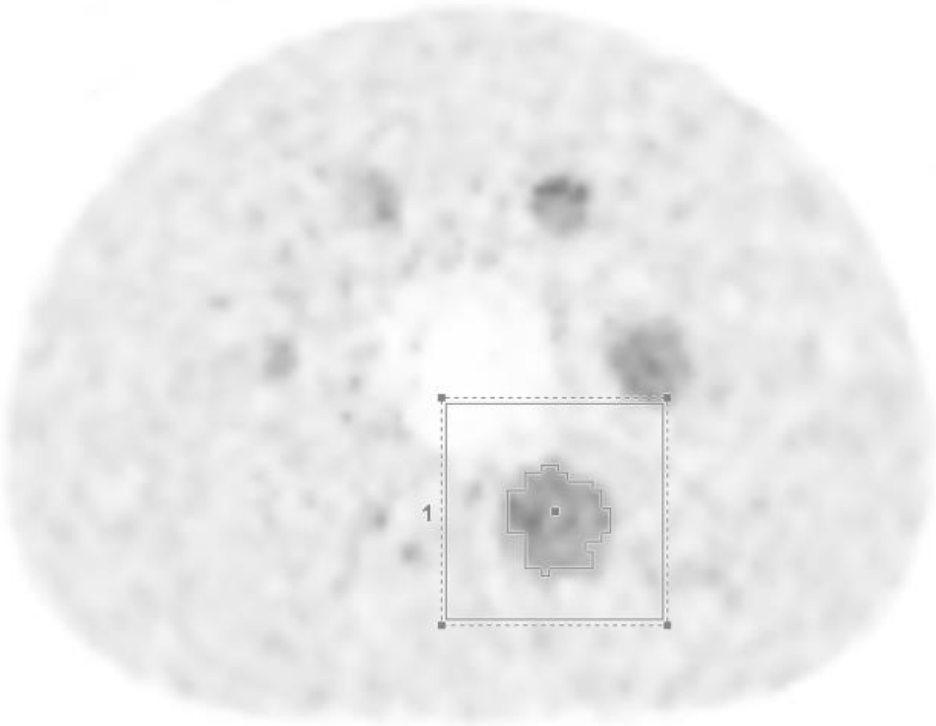

Figure 2. 18 NEMA Body Phantom with ^{68}Ga isotope reconstructed with the Q.Clear algorithm for the Beta = 150 (VP HD), 1h 8 minutes after recorded time.

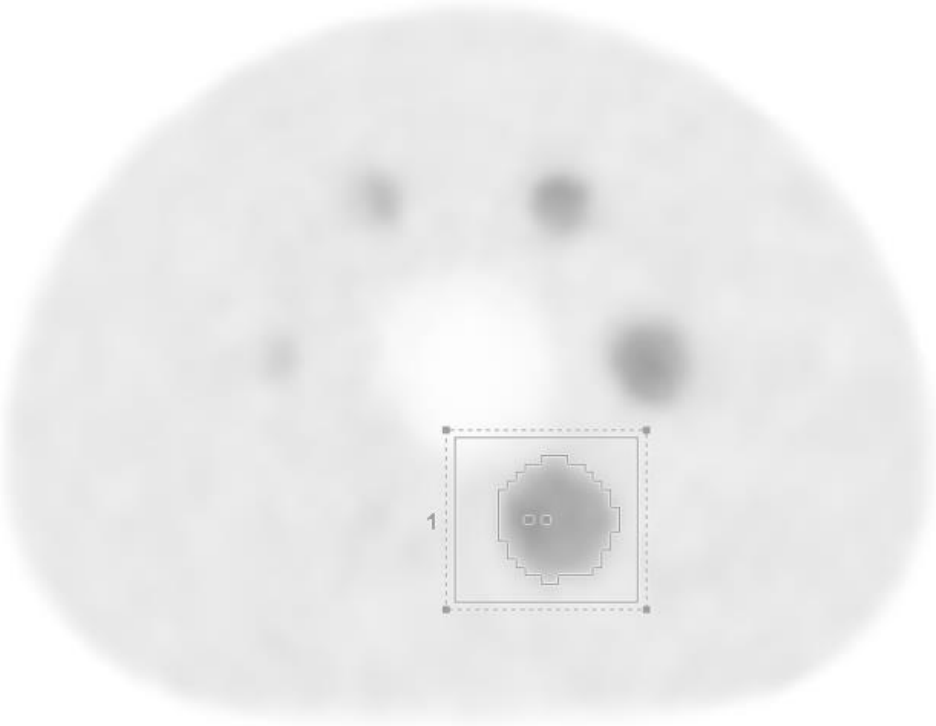

Figure 2. 19 NEMA Body Phantom with ^{68}Ga isotope reconstructed with the Q.Clear algorithm for the Beta = 850 (VP HD), 1h 8 minutes after recorded time.

3.2.1.b Discussion

The visual assessment performed showed that at higher Beta, the outlines using the autocontour of the largest spheres acquire a more oval shape, consistent with reality. Increasing the Beta, however, results in the loss of the smallest two spheres, which means that, despite the smoothed background area, a potentially important diagnostic information can be lost.

3.2.2. SUV analysis

3.2.2.a Results

The values of SUV mean, SUV max and SUV peak were determined on the reconstructed images with the use of automatic contouring method, with a threshold value of 42% (the value has a clinical application) for the spheres and body parts of the phantom. Automatic contour was used in the image analysis to eliminate the influence of the subjective judgment of the researcher. The described parameters were determined for beta in the range of 350 – 950, for two types of reconstruction VP FX+Q.Clear and VP HD+Q.Clear (graph 2.12-17). Particular attention was paid to the influence of Beta for the smallest spheres (graph 2.18-19). The SUV mean, peak and max were selected for the analysis, as a set of parameters allowing the assessment of the advancement of the disease by the physicians.

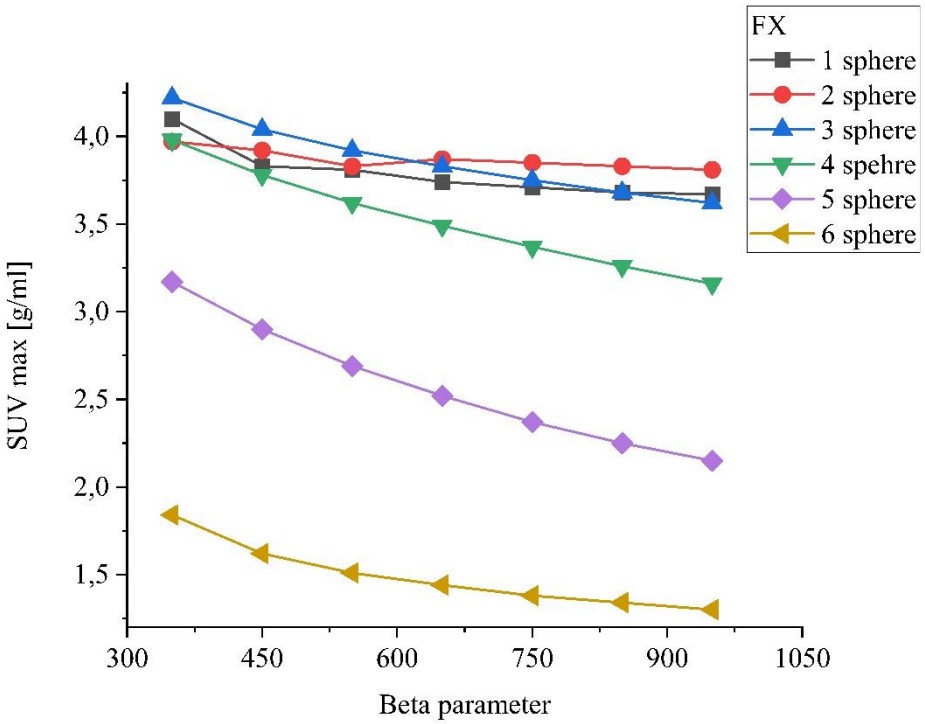

Graph 2. 12 Dependence of SUV max values for spheres in the NEMA IEC Body Phantom on the Beta parameter (150 – 950), 1 h 8 minutes min after recorded time (VUE Point FX).

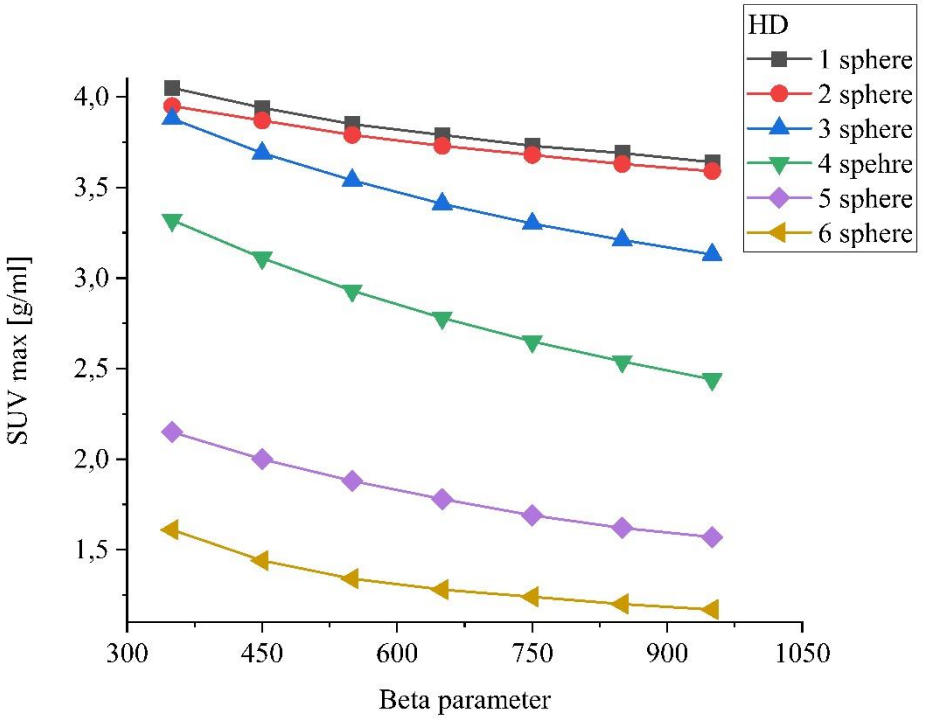

Graph 2. 13 Dependence of SUV max values for spheres in the NEMA IEC Body Phantom on the Beta parameter (150 – 950), 1 h 8 minutes min after recorded time (VUE Point HD).

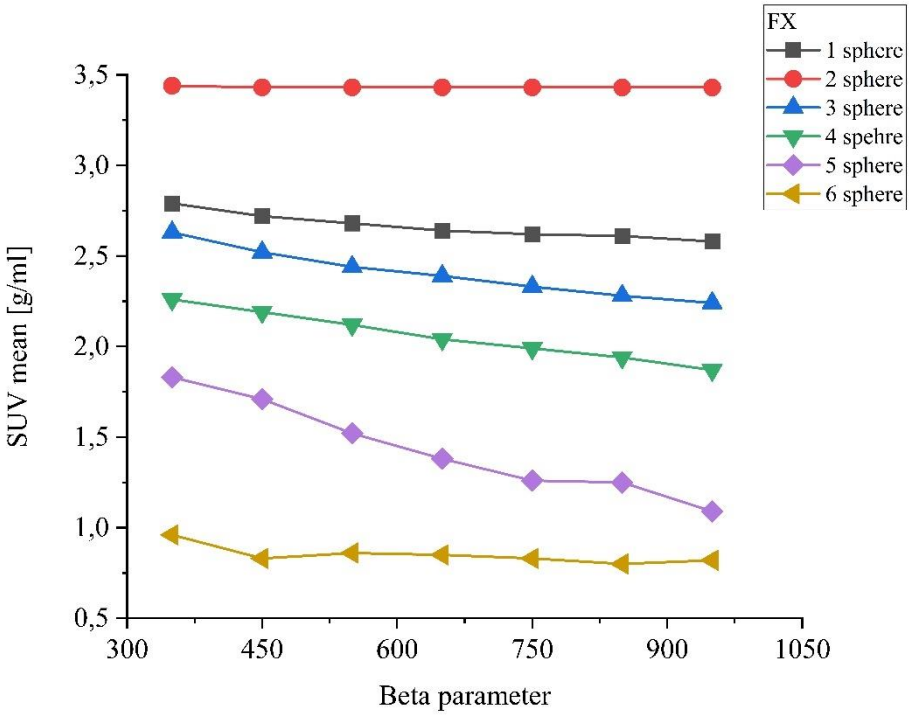

Graph 2. 14 Dependence of SUV mean values spheres in of the NEMA IEC Body Phantom on the Beta parameter (350 – 950), 1 h 8 minutes min after recorded time (VUE Point FX).

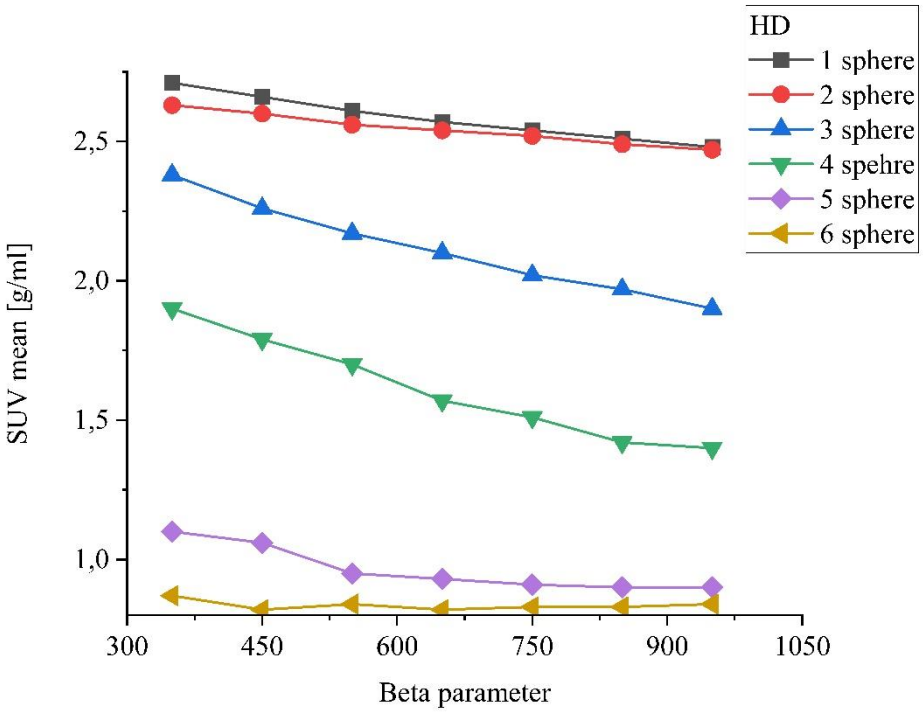

Graph 2. 15 Dependence of SUV mean for spheres in the NEMA IEC Body Phantom on the Beta parameter (350 – 950), 1 h 8 minutes min after recorded time (VUE Point HD).

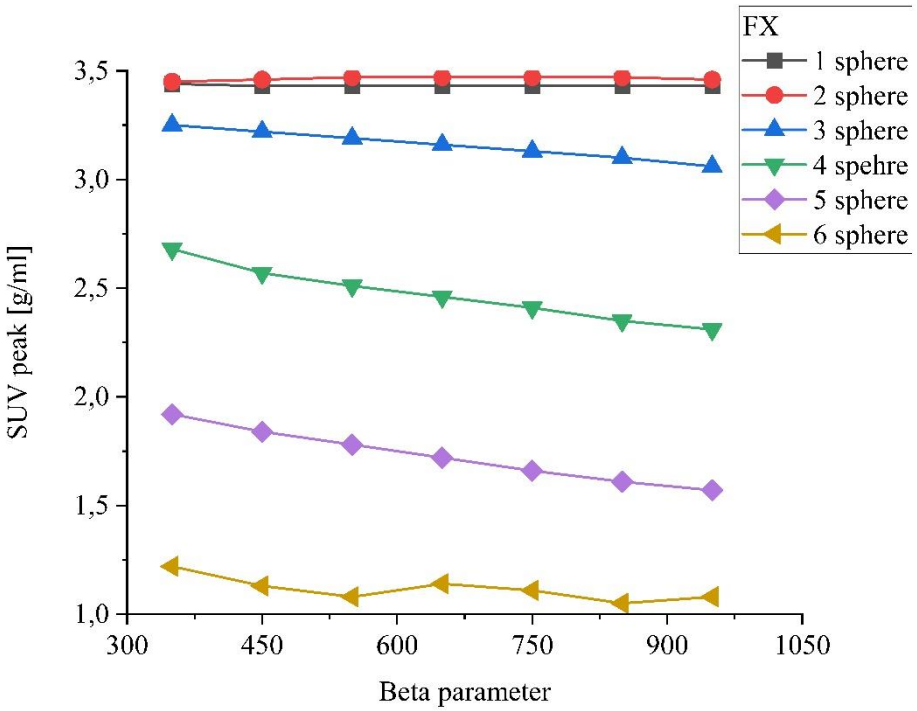

Graph 2. 16 Dependence of SUV peak values for spheres in the NEMA IEC Body Phantom on the Beta parameter (350 – 950), 1 h 8 minutes min after recorded time (VUE Point FX).

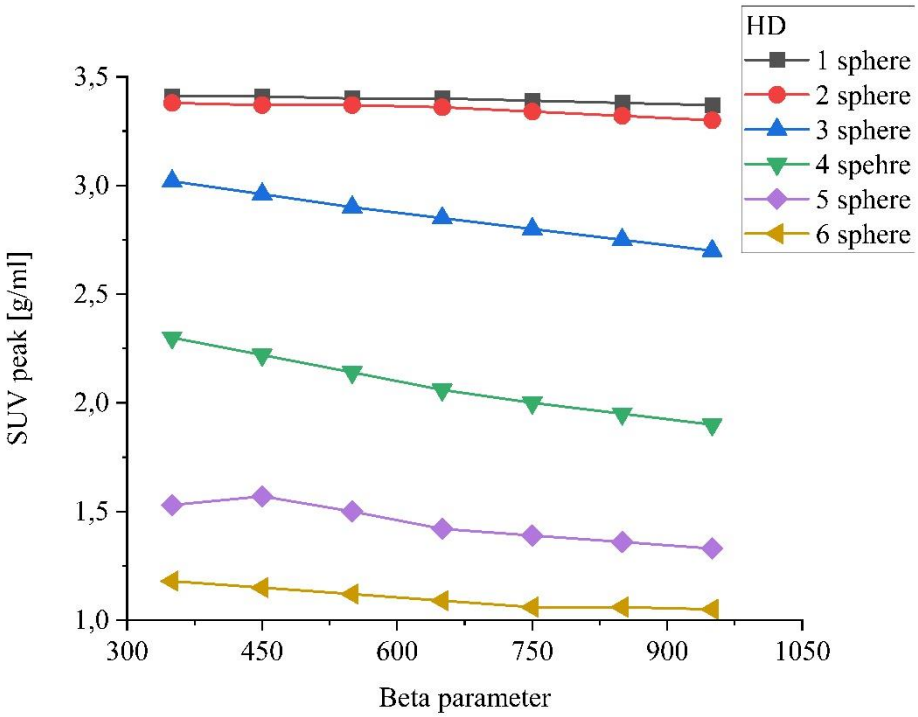

Graph 2. 17 Dependence of SUV peak values for spheres in the NEMA IEC Body Phantom on the Beta parameter (350 – 950), 1 h 8 minutes min after recorded time (VUE Point HD).

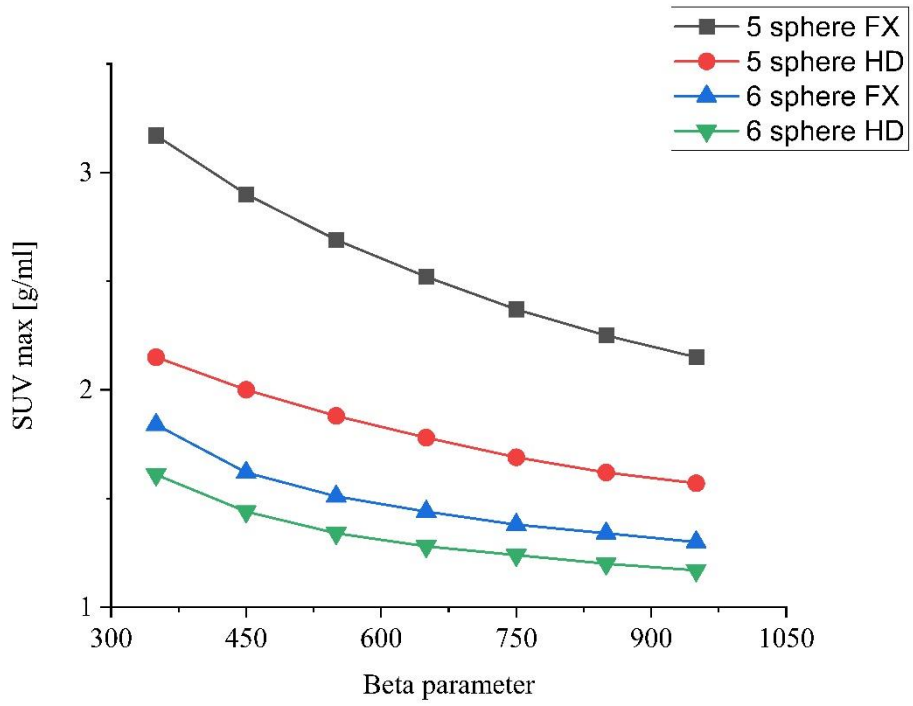

Graph 2. 18 Dependence of SUV max values for 5th and 6th spheres in the NEMA IEC Body Phantom on the Beta parameter (350 – 950), 1 h 8 minutes min after recorded time (VUE Point HD/FX).

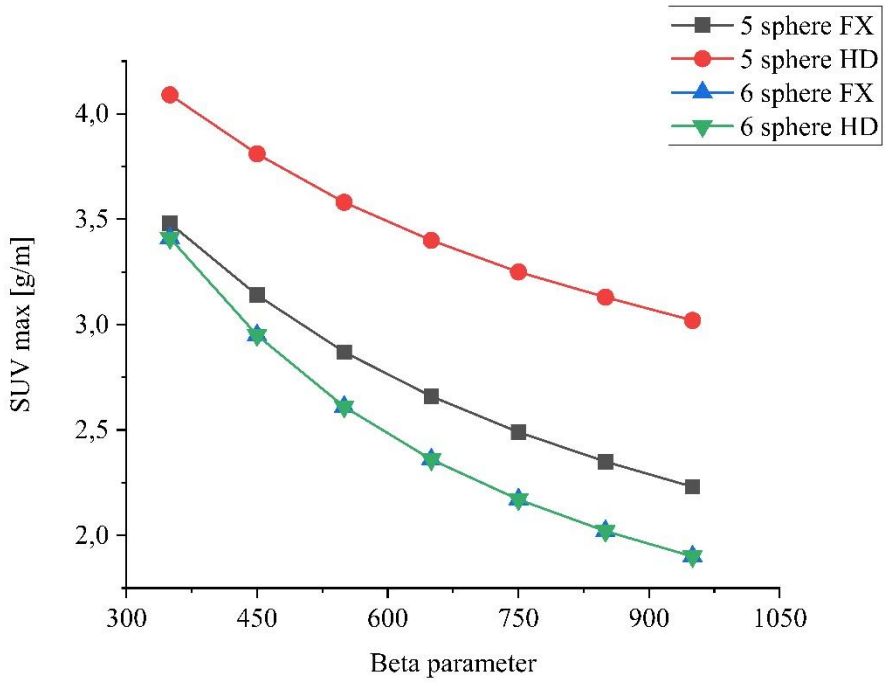

Graph 2. 19 Dependence of SUV max values for 5th and 6th spheres in the NEMA IEC Body Phantom on the Beta parameter (350 – 950), 2 h 26 minutes after recorded time (VUE Point HD/FX).

The comparison of the SUV mean value decrease for higher values of the beta parameter of 450 and 950 against the value of 250 was used for the analysis (table 2.4-9).

Table 2. 4 Summary of Beta and SUV max values 1h 8 minutes after recorded time.

Beta parameter value	SUV max value 4th sphere		Difference to value for β=250 [%]		SUV max value 5th		Difference to value for β=250 [%]		SUV max value 6th sphere		Difference to value for β=250 [%]	
	FX	HD	FX	HD	FX	HD	FX	HD	FX	HD	FX	HD
250	4.25	3.59			3.51	2.36			2.36	1.94		
450	3.78	3.11	-11.1	-13.37	2.9	2	-17.38	-15.25	1.62	1.44	-31.36	-25.77
950	3.16	2.44	-25.65	-32.03	2.15	1.57	-38.75	-33.48	1.3	1.17	-44.92	-39.69

Table 2. 5 Summary of Beta and SUV mean values 1h 8 minutes after recorded time

Beta parameter value	SUV mean value 4th sphere		Difference to value for β=250 [%]		SUV mean value 5th		Difference to value for β=250 [%]		SUV mean value 6th sphere		Difference to value for β=250 [%]	
	FX	HD	FX	HD	FX	HD	FX	HD	FX	HD	FX	HD
250	2.41	2.03			2.11	1.35			1.23	1.01		
450	2.19	1.79	-9.13	-11.82	1.71	1.06	-18.96	-21.48	0.96	0.82	-32.52	-18.81
950	1.87	1.4	-22.41	-31.03	1.09	0.9	-48.34	-33.33	0.83	0.84	-33.33	-16.83

Table 2. 6 Summary of Beta and SUV peak values 1h 8 minutes after recorded time.

Beta parameter value	SUV peak value 4th sphere		Difference to value for β=250 [%]		SUV peak value 5th		Difference to value for β=250 [%]		SUV peak value 6th sphere		Difference to value for β=250 [%]	
	FX	HD	FX	HD	FX	HD	FX	HD	FX	HD	FX	HD
250	2.68	2.39			2.01	1.75			1.25	1.26		
450	2.57	2.22	-4.1	-7.12	1.84	1.53	-8.46	-10.29	1.13	1.15	-9.6	-8.7
950	2.31	1.9	-13.81	-20.5	1.57	1.33	-21.89	-24	1.08	1.05	-13.6	-16.67

Table 2. 7 Summary of Beta and SUV max values 2h 26 minutes after recorded time.

Beta parameter value	SUV max value 4th sphere		Difference to value for β=250 [%]		SUV max value 5th		Difference to value for β=250 [%]		SUV max value 6th sphere		Difference to value for β=250 [%]	
	FX	HD	FX	HD	FX	HD	FX	HD	FX	HD	FX	HD
250	4.52	4.52			4.15	4.52			4.07	4.07		
450	3.81	3.81	-15.71	-15.7	3.14	3.81	-24.33	-15.71	2.95	2.95	-27.52	-27.19
950	3.02	3.02	-33.19	-33.19	2.23	3.02	-46.27	-33.19	1.9	1.9	-53.32	-57.46

Table 2. 8 Summary of Beta and SUV mean values 2h 26 minutes after recorded time.

Beta parameter value	SUV mean value 4th sphere		Difference to value for β=250 [%]		SUV mean value 5th		Difference to value for β=250 [%]		SUV mean value 6th sphere		Difference to value for β=250 [%]	
	FX	HD	FX	HD	FX	HD	FX	HD	FX	HD	FX	HD
250	2.53	2.53			2.29	2.31			1.66	2.28		
450	2.27	2.27	-10.28	-10.27	1.74	1.77	-24.34	-23.38	0.97	1.66	-35.66	-27.52
950	1.79	1.77	-29.25	-30.1	1.16	1.2	-46.27	-48.06	0.87	0.97	-63.18	-53.32

Table 2. 9 Summary of Beta and SUV peak values 2h 26 minutes after recorded time.

Beta parameter value	SUV peak value 4th sphere		Difference to value for β=250 [%]		SUV peak value 5th		Difference to value for β=250 [%]		SUV peak value 6th sphere		Difference to value for β=250 [%]	
	FX	HD	FX	HD	FX	HD	FX	HD	FX	HD	FX	HD
250	2.75	2.75			2.05	2.05			1.67	1.67		
450	2.6	2.6	-5.46	-5.46	1.86	1.86	-9.27	-9.27	1.53	1.53	-9.27	-9.27
950	2.26	2.26	-17.82	-17.82	1.58	1.58	-22.93	-22.93	1.21	1.32	-22.93	-22.93

3.2.2.b Discussion

Analysis of SUV results for low β values of 150 indicated that SUV values were overestimated, especially for VP HD reconstructions and low concentrations of radiopharmaceutical in the phantom. This precluded the use of very low Beta parameter values for patient imaging. At Beta values of 250 and above, there was a decrease in SUV_{mean}, max and peak values. This decrease was highest for the smallest spheres, SUV mean/max values and Beta values of 950 (the maximum value used in the study). Comparison of the SUV_{mean} and SUV_{max} values for the smallest spheres (4-6) showed that there is decrement in these semi-quantitative results by up to 60% at low concentrations of the radiopharmaceutical for the Beta parameter of 950 versus 250.

3.3.3 Image Quality analysis - Contrast recovery Coefficient (CRC)

3.3.3.a Introduction

The measurements for PET systems before they are allowed to be put into service are defined by standards developed by the National Electrical Manufacturers Association (NEMA). They are based on the use of the ^{18}F isotope. One of the parameters evaluated is the image quality estimated for cold and hot foci. The image quality for hot spots is defined according to the formula (23) which describes so called contrast recovery coefficient (CRC). In the analysis of fluorine isotope data, activity is injected into the phantom at 4:1 or 8:1 ratios of spheres activity to body parts activity [65]. Then, the pass value determined for the background is compared to the ROI average pass values determined during the measurements. The test uses two largest spheres as cold spots and the remaining spheres as hot spots. Due to the fact that patients are given a lower activity of the ^{68}Ga isotope (about 150 MBq) than the ^{18}F isotope (typical dosage required is 4 MBq/kg, which gives about 300 MBq in total). The activity of about 140 activity was introduced into the phantom body part, while the activity in the spheres was 3.8 times higher (the planned ratio was 1:4). This is a situation that imitates an increased uptake relative to the patient's background, which allows to determine the sensitivity of the method in unfavorable circumstances - low overexpression of the receptor in the patient's neoplastic lesion.

$$CRC_{hot} = \frac{\frac{C_{hot}}{C_{bkgd}} - 1}{\frac{a_{hot}}{a_{bkgd}} - 1} * 100 \quad (23)$$

where C_{hot} and C_{bkgd} are the average/max of the counts measured (activity concentration) in the hot sphere ROI and the average/max of the counts in all background ROIs, respectively, and a_{hot}/a_{bkgd} is the ratio of the mean concentration in the hot sphere and background [66].

The PET/CT Discovery MI DR system is equipped with an automatic software tool to evaluate the CRC parameter with NEMA phantom. The image quality analysis is performed in accordance with the NEMA-2011 criteria which is appropriate for the system which was produced when this particular standard was in force. According to these criteria, the four smallest spheres should contain a higher concentration than the background (e.g. 4:1), while the two largest should be supplemented with an inactive solution – water [65]. It is possible to obtain CRC_{hot} results for the reconstructed images of the 4 smallest spheres defined manually by the user. The user can obtain results for all particular spheres just by selecting them. Anyway during one analysis, 4 hot spheres can be assessed at the same time in PET/CT Discovery MI DR system (fig. 2.20 A, and D). The graph also shows the layer of the image for which the

analysis is performed. This allows the operator to assess whether the automated tool is performing the analysis correctly (fig. 2.20 C) or not. Next to the designated ROIs for the spheres, there are ROIs that are used to analyze the background values (fig. 2.20 B). One can see in the selected area the CRC increase in accordance to the increase in the size of the sphere (fig 2.20 A).

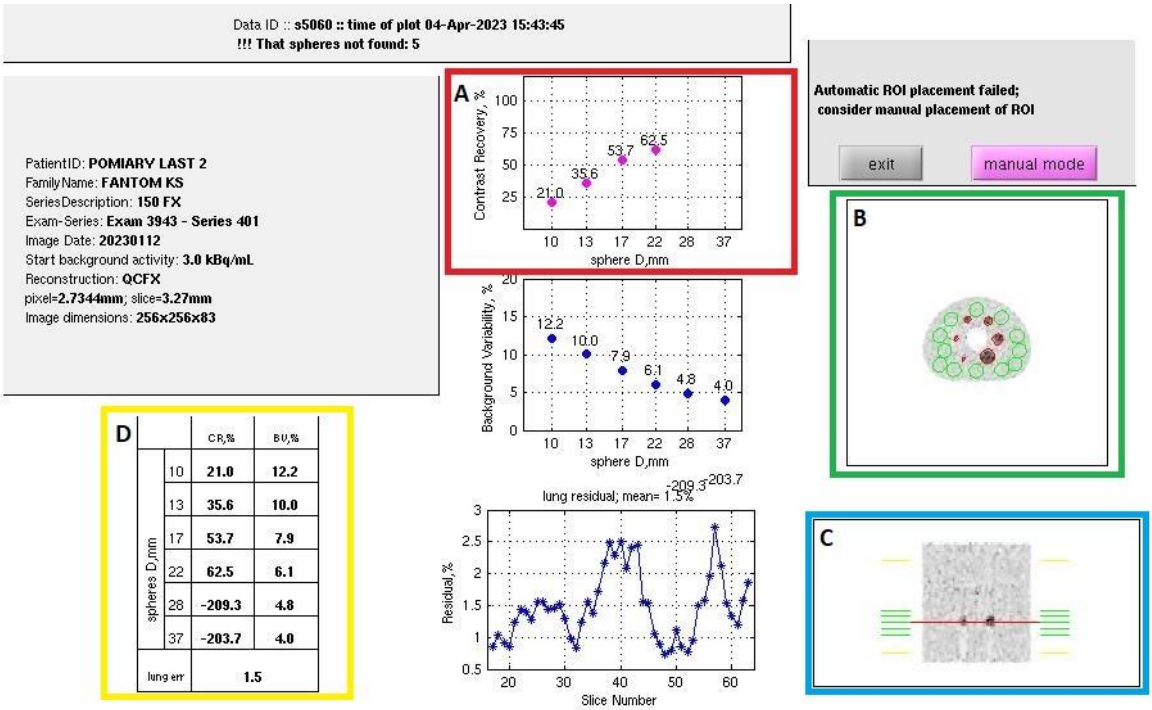

Figure 2. 20 Screenshot showing the automatic tool used for CRC evaluation.

3.3.3.b Results

Data for the calculation of average activity concentration values in the body part were obtained from the analysis described in section 3.1.3. For the spheres, the average concentration values were measured using an automatic contour at a threshold of 42%. In the analysis of image quality for measurements with the NEMA Body Phantom, this formula was used, but the quantitative change in the spheres was assessed for all spheres imitating the hot spots. The aim of the analysis was to verify how the $CRC_{hotmean}$ changes for all spheres filled with the same concentration of the solution with the ^{68}Ga isotope, along with the change of the β for two types of VP HD and VP FX reconstructions (graph 2.20-24). In addition, due to the very similar results of the measured averages in the smallest spheres and in the body part, CRC_{hotmax} values for changes and body part were compared, in accordance with the above formula 23 (graph 2.25).

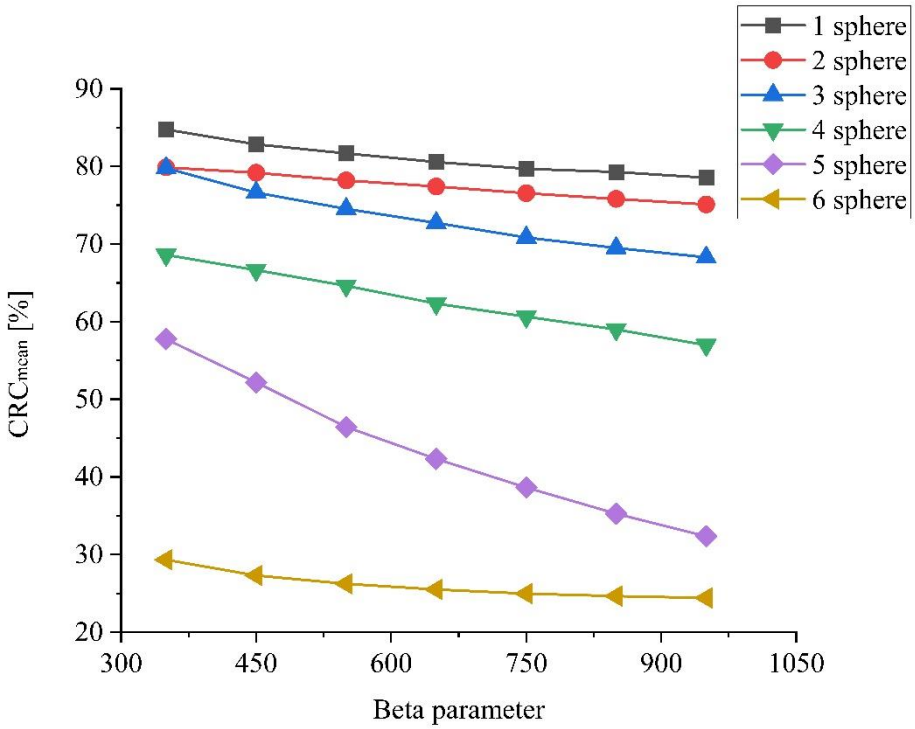

Graph 2. 20 Dependence of CRCmean values for six spheres in the NEMA IEC Body Phantom on the Beta parameter (350 – 950), 1 h 8 minutes after recorded time (VUE Point FX).

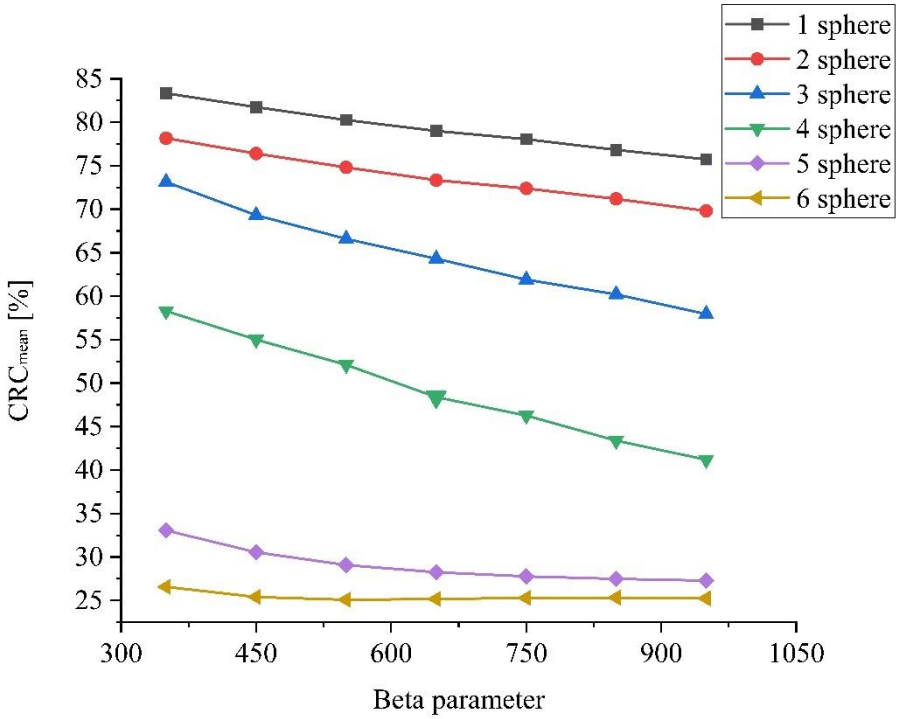

Graph 2. 21 Dependence of CRCmean values for six spheres in the NEMA IEC Body Phantom on the Beta parameter (350 – 950), 1 h 8 minutes after recorded time (VUE Point HD).

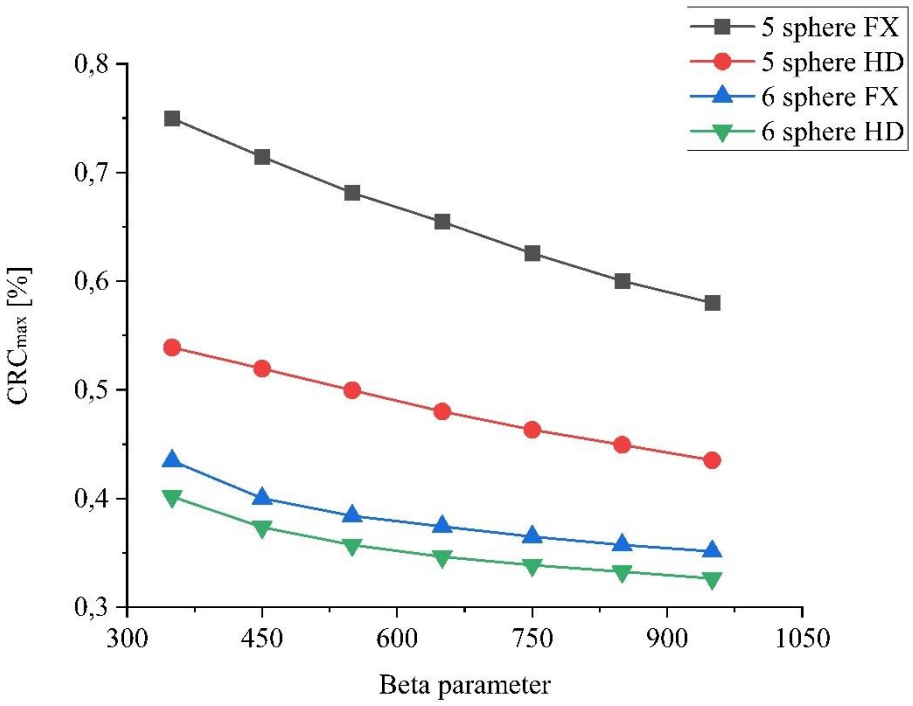

Graph 2. 22 Dependence of CRCmax values for six spheres in the NEMA IEC Body Phantom on the Beta parameter (350 – 950), 1 h 8 minutes after recorded time (VUE Point HD/FX).

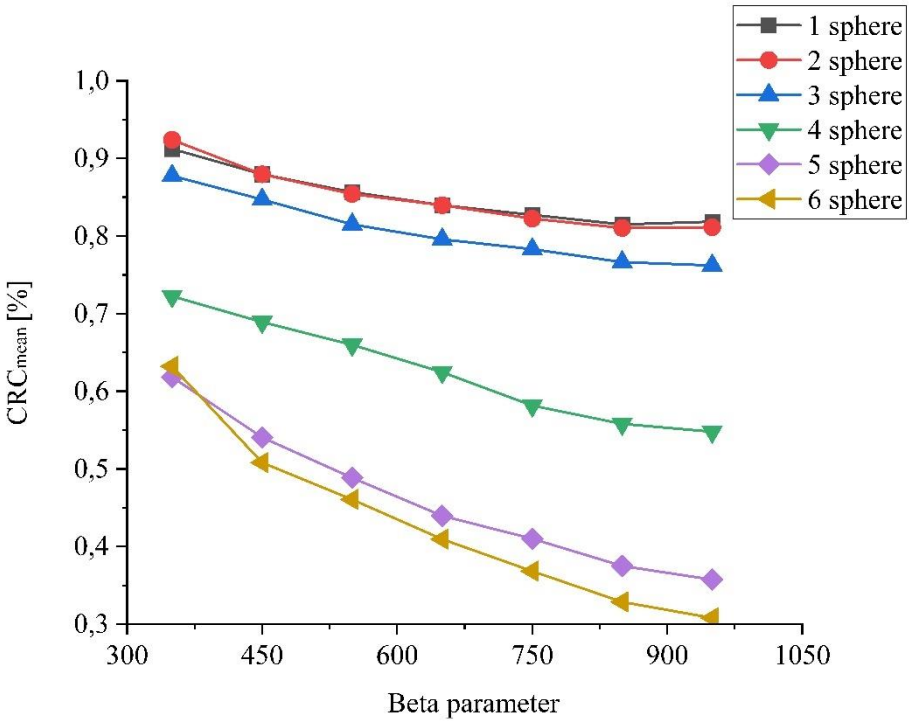

Graph 2. 23 Dependence of CRCmean values for six spheres in the NEMA IEC Body Phantom on the Beta parameter (350 – 950), 2h 26 minutes after recorded time (VUE Point FX).

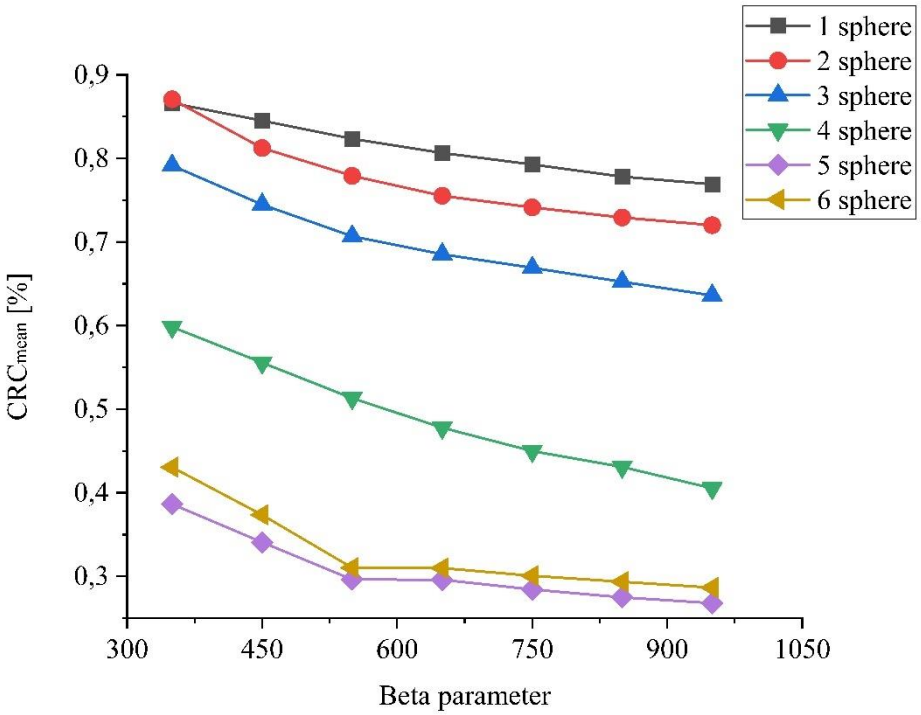

Graph 2. 24 Dependence of CRCmean values for six spheres in the NEMA IEC Body Phantom on the Beta parameter (350 – 950), 2h 26 minutes after recorded time (VUE Point HD).

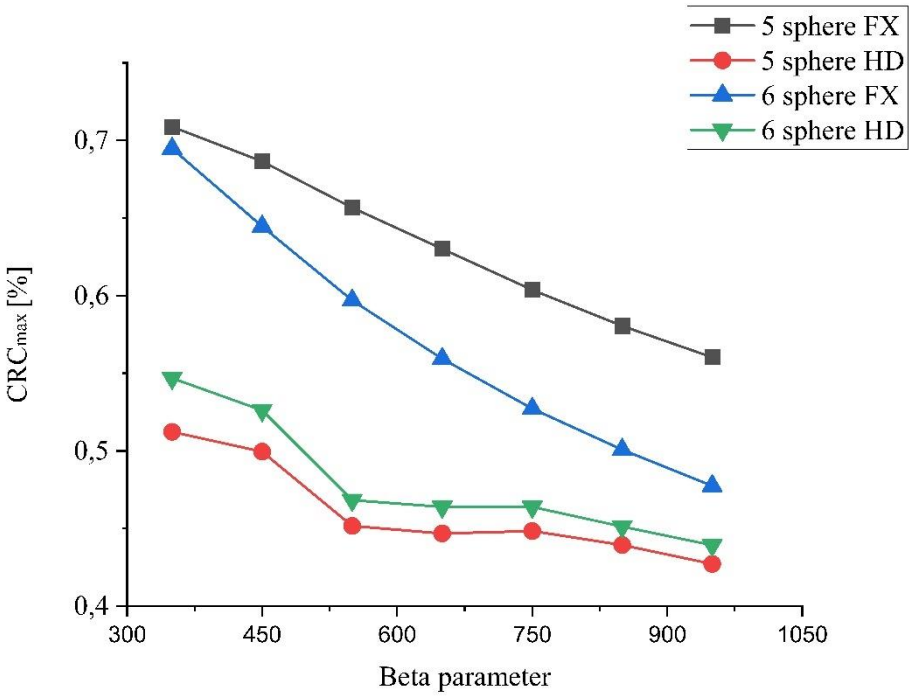

Graph 2. 25 Dependence of CRCmax values for the two smallest spheres in the NEMA IEC Body Phantom o the Beta parameter (350 – 950), 2h 26 minutes after recorded time (VUE Point HD/FX).

3.3.3.c Discussion

The obtained results show significant dependence between CRC_{mean} and CRC_{max} coefficients and the Beta parameter values in the range of 350 – 950. In graphs 2.20-24-27, a clear decrease in the CRC value can be observed when β increases, which is an unfavorable phenomenon.

For CRC values, there are also clear differences between the reconstruction of VP FX and VP HD in measurements made both after 1 h and after more than 2 h. In the VP FX reconstruction, we can observe relatively similar CRC_{mean} values for the three largest spheres (1-3). The differences for these spheres increase as Beta increases. When using VP HD reconstruction, differences in CRC_{mean} values between spheres 1 – 3 are greater. Interestingly, for the smallest spheres, a more favorable result of the CRC_{mean} value can be observed after a longer time from filling the phantom (2h 26 minutes).

The CRC_{max} and CRC_{mean} values obtained in the experiment for the smallest spheres may be influenced by the low background-to-spheres ratio (1:3.8) and the limited capabilities of the autocontur tool. With higher Beta values, this tool marked too large areas in relation to the real ones, which actually lowered the CRC value.

3. Conclusions

The analysis of the phantom studies showed the influence of β parameter on the visual, semi-quantitative SUV and CRC estimates for the PET/CT images of the hot spheres with varying size range and different activity levels (1h 8 minutes and 2h 26 minutes after recorded time) for two reconstruction algorithms VP FX + Q.Clear and VP HD + Q.Clear. The results presented here show that the image quality of body part increases together with an increase of the β value in the Q.Clear algorithm – the image is smoother and more homogenous. However, the increase in the β value adversely affects the semi-quantitative assessment of the SUV and the CRC parameter, which quantitatively describes the diagnostic capabilities of the PET device. The CRC value is lower than that obtained for similar studies [66, 67]. The lower CRC results may be due to the fact that the study used a gallium isotope, which has a much greater maximum range of positrons in tissue than in the case of the fluorine ^{18}F isotope, resulting in more blurred image.

The obtained results show that it is more advantageous to use VP FX + Q.Clear reconstructions compared to VP HD + Q.Clear. High homogeneity of the body part was obtained for lower values of the Beta while its impact on the decrease in the value of SUV and CRC was limited.

The analysis performed using the phantom allows to conclude that the optimal solution is to use the VP FX + Q.Clear algorithm in combination with the Beta from the range of 350 – 450. Images for the Beta below 350 show a significant decrease homogeneity in the background (body part). Below 150 an distortion in the SUV value can be observed, while above 450 an unfavorable and significant decrease in the SUV and CRC values appears. The increase of the β may affect the final diagnosis, especially in the case of smaller lesions with which the partial volume effect (PVE) plays a significant role.

Studies using the phantom have shown that it is a safe way and optimal tool to select the appropriate type of image reconstruction and the value of Beta, which is responsible for noise control in the PET/CT Discovery MI DR system. The results of the conducted research were used in further analysis, in this case, in the assessment of the impact of image reconstruction on the actual results of patients. The selected variant of the conducted research, i.e. the assumption of a low concentration difference between the spheres and the bad part and lower activity in the phantom in relation to NEMA standards, including the use of the gallium ^{68}Ga isotope, was aimed at the most realistic simulation of the clinical cases, i.e. patients with slight changes in the pathological uptake of somatostatin analogues.

This shows that choosing the right Beta value is some kind of compromise between high background homogeneity and CRC/SUV values and β value should be determined by an interdisciplinary team with clinical experience. The study shows that the value of β must not be arbitrarily changed, in order to improve the image quality. As can be seen, the increase in β value, especially for small changes with low statistics, is unfavorable, as the SUV value decreases, which may affect the final diagnosis. This effect should be taken into account in the clinical selection of Beta value for different radiopharmaceuticals due to the administration of variable activity to patients.

In a similarly conducted study, the β range estimated as optimal was slightly different and equal to 300-600 [37, 68, 69]. Here obtained results fall within the above but they narrow it to 350-450 and additionally show the influence of β on all significant elements in the diagnostic evaluation of PET/CT with a gallium ^{68}Ga isotope.

Chapter III

1. Introduction

The phantom study was the first stage of the project. Satisfactory results were obtained and the differences between the two types of reconstruction: VP HD+Q.Clear and VP FX+Q.Clear, were evaluated. In this way, the range of the optimal value of the Beta and the type of reconstruction for the phantom were also selected. Phantom studies allowed to assess the impact of β settings in idealized circumstances. The clinical trials are characterized by many parameters which are difficult to control and make the investigations much complicated e.g. there was no patient's respiratory movement, nor was there a change in isotope concentration in the hot spheres in the phanotm case. Phantom studies built also confidence in the available Q.Clear image reconstruction technique. This is very important, because decisions considering patients treatment have to be made on the basis of the of the diagnostic studies descriptions. Interestingly, the Q.Clear reconstruction algorithm has not often been used in the NM Department so far. Descriptions of examinations were made by physicians based on the known and reliable OSEM algorithm with time-of-flight correction (VP FX). This is the default image reconstruction algorithm which was available on the previously used PET/CT system (Discovery 690).

Scientific reports and manufacturer's data indicated that the Q.Clear reconstruction algorithm allows to obtain higher SUV values in the semi-quantitative assessment compared to the standard reconstruction, i.e. VP FX/HD without Q.Clear [70-73]. Obtaining higher SUV values does not mean that the studied tumour classification will be different. In the standard diagnosis of neuroendocrine tumours in patients, a neoplastic lesion is characterized by a visual assessment in the Krenning scale [74]. This scale describes the relationship between the uptake of radiolabeled somatostatin analogues in lesions and the physiological uptake in the liver, spleen and kidneys (individually for each patient). The Krenning scale, as a form of some kind of visual assessment, is closely related to the quantitative assessment, as a change in the lesion uptake value (height) affects the Krenning score. Changing the reconstruction algorithm may result in a change in the Krenning score, especially from grade 2 to grade 3. The second grade on the scale describes the pathological lesion as the lesion characterised by the same uptake value as the liver. The third grade lesion shows the uptake above the level of the liver. The visual assessment reflects the quantification of the mean amount of uptake in the lesion.

2. Study group

2.1. Descriptions of the patients

The study group of 6 patients consisted of male (3) and female (3). All patients have neuroendocrine tumours. Most of the cases were at an advanced stage of the disease (5). The patients have many neoplastic lesions located in various parts of the gastrointestinal tract (mostly in the liver) and in the skeleton. Neoplastic lesions were characterized by variable expression of somatostatin receptors, which resulted in variable values for the uptake of radiolabeled somatostatin analogs. Patients group was characterized by variable weight and height (BMI) and were suffering from the metastases of variable dimensions. A total of 25 neoplastic lesions were used for the analysis, most of which (13) were smaller than 15 mm. There were 5 and 6 lesions within the size range of 15-20 mm and 20-50 respectively. The largest considered lesion was almost as large as 103 mm in diameter. The smallest measured metastasis was 5.7 mm (table 3.1).

2.2. Imaging

Patient imaging was performed in a bed sequence in which the number of beds depended on the height of the patient. Each bed was imaged for 3 minutes in order to obtain the appropriate counting statistics. The scanning parameters were as follows: DFOV – 80 cm, matrix size –256x256, slice thickness – 3.3 mm. PET/CT examinations were performed in the first quarter of 2023.

In order to obtain comprehensive results for the patient image data, a comparison was made for three types of image reconstruction:

- VP FX with 3 iterations and 18 subsets, filter cutoff 5.0 mm, Z-Axis filter standard,
- VP FX+Q.Clear (Beta in range 350-550), VP HD+Q.Clear (Beta in range 350-550).

Thus, the analysis for the assessment of patients was extended.

Table 3. 1 Summary of data on changes in pathological uptake with patient data and administered activity.

No	BMI $(W/H^2)^*$	Activity on the start of the scan [MBq]	Localization of the metastasis	lesion size [mm]
1	35.63	70.32	pancreas	13.2
2	38.67	79.587	liver; bowel; bowel	9.7; 16.2; 33.7

3	25.61	71.54	mediastinum bone, spine, spine, mediastinum bone, above liver, liver; spine; spine	15.8; 9; 7; 14.1; 8.5; 12.6; 8; 11.7;
4	19.49	71.4	liver; liver; liver	12.8; 21.9; 39.3
5	22.86	80.15	liver; liver; hip bone; liver; liver; liver; bone; bone	46.2; 16.6; 17.9; 29.7; 5.7; 16.9; 10.6; 7.8
6	27.06	92.62	liver; liver	102.9; 26.9

3. Results

As in the phantom study, the analysis was divided into visual qualitative assessment and quantitative data describing the relationships between 3 types of reconstruction.

3.1.a. Visual analysis of PET/CT scans

Visual assessment was used to identify foci of pathological uptake in the patient's body and to determine sufficient image quality for further studies. The visual analysis included the image of the whole patient and the assessment of the level of liver homogeneity and the visibility of lesions of pathological radiotracer uptake. These two approaches were used to:

- evaluate homogeneity of the image in the thoracic space, where there is a very low level of uptake of radiolabeled somatostatin analogues,
- maintain the possibility of proper comparison of pathological changes to the uptake in the liver and spleen, on the basis Krenning scale.

In the visual characteristics and in the further statistical analysis, also the influence of the β choice was assessed on the tumour outline determined by the auto-contour tool (fig. 3.1-4).

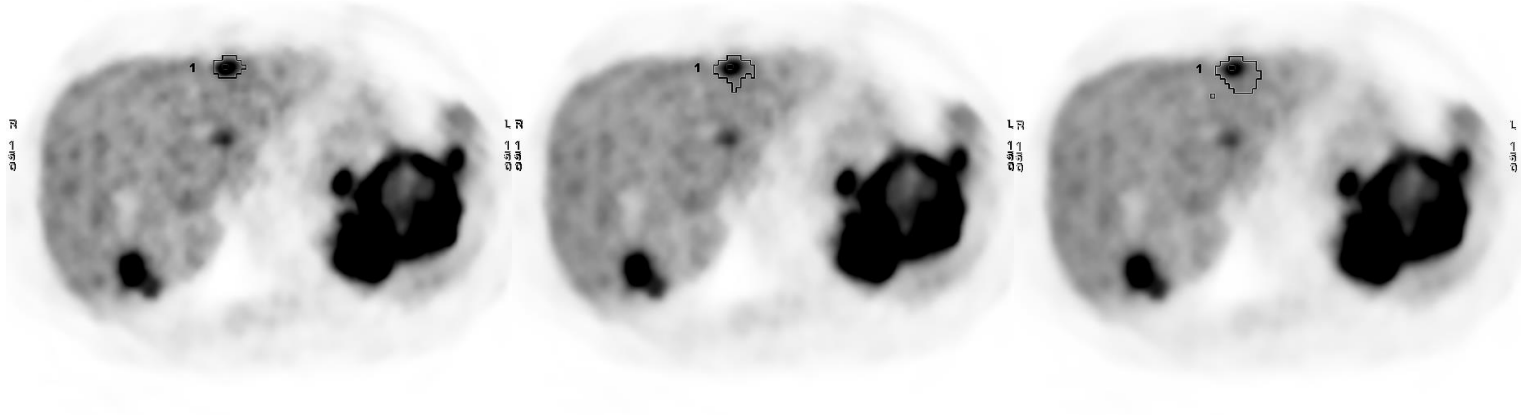

Figure 3. 1 1-layer of the PET/CT image series obtained for the patient with neuroendocrinal tumour with marked lesion of pathological uptake. From left side: images obtained with the VP HD+Q.Clear reconstruction technique with Beta in range 350-550, step 100.

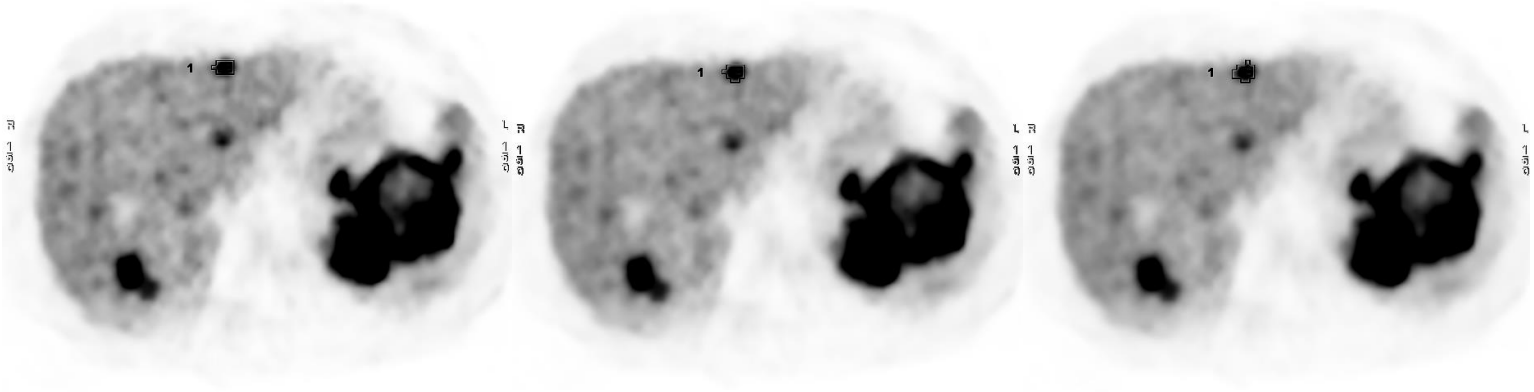

Figure 3. 2 1-layer of the PET/CT image series obtained for the patient with neuroendocrinal tumour with marked lesion of pathological uptake. From left side: images obtained with the VP FX Q.Clear reconstruction technique with Beta in range 350-550, step 100.

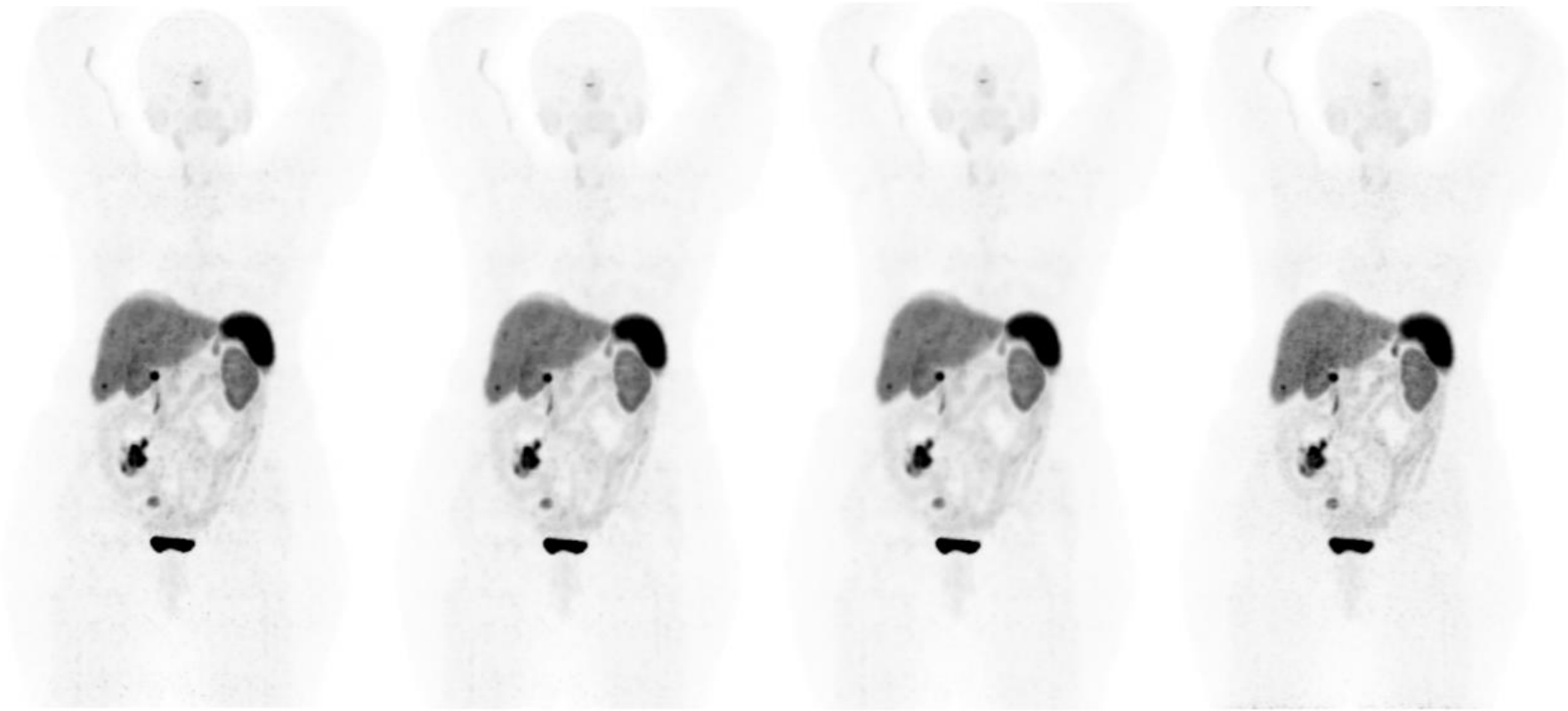

Figure 3. 3 1-layer of the PET/CT image series obtained for the patient with neuroendocrinal tumour. From left side: images obtained with the VP HD+Q.Clear reconstruction technique with Beta in range 350-550, step 100 (3 images); image obtained with the VP FX, without Q.Clear.

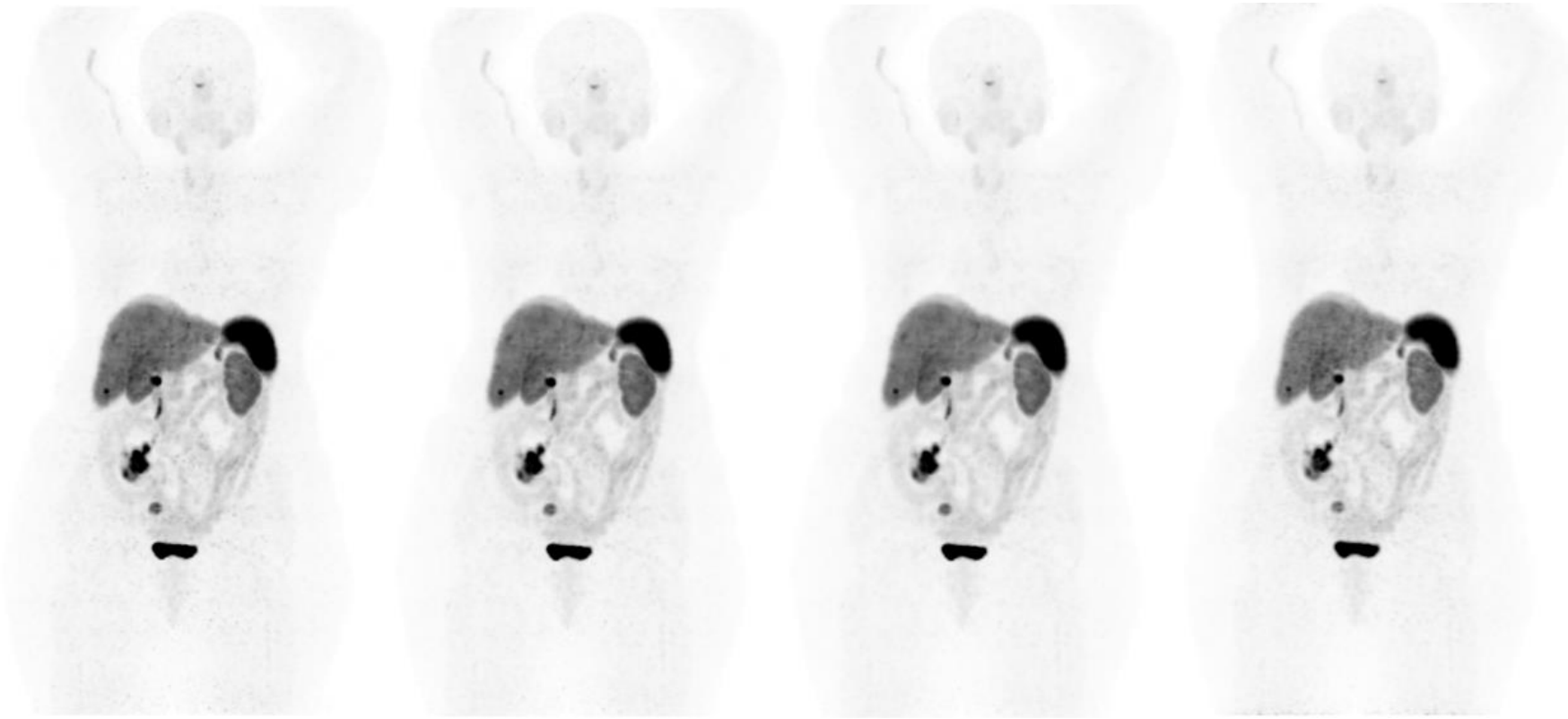

Figure 3. 4 1-layer of the PET/CT image series obtained for the patient with neuroendocrinal tumour. From left side: images obtained with the VP HD+ Q.Clear reconstruction technique with Beta in range 350-550, step 100, images obtained with the VP FX, without Q.Clear.

3.1.b Discussion

Analysis of the liver areas showed that an increase in Beta resulted in a more homogeneous liver image. It can also be observed that there is a greater higher value (darker image) of liver uptake with the VP HD+Q.Clear algorithm compared to VP FX+Q.Clear (fig. 3.1 – 2).

Visual assessment of examinations may be important due to the decrease in the homogeneity of the image in the thoracic region. It can be seen that increment of Beta allows to increase the homogeneity of the image in this area (figure 3.3 – 4). The level of operator experience who is evaluating the image can certainly influence the assessment. As experience increases, image quality requirements may decrease, but an optimum must be maintained.

Despite the increase in the uplift value, a constant, practically unchanging outline of the lesion marked as 1 can be observed in the VP FX+Q.Clear reconstruction. This outline changes significantly for the VP HD+Q.Clear reconstruction for β value from the range of 350 – 550. Importantly, however, the images obtained with the Q.Clear algorithm use show that similar changes occur as in the study of phantoms. A decrease in the β value causes a decrement in image quality.

3.2.a Semi – quantitative data

On the basis of the assessment of lesions in semi–quantitative way relying on the level of activity concentration (kBq/ml) and the evaluation of the Krenning scale, a statistical analysis was performed, including:

- Assessment of the relationship between the mean and maximum liver uptake and lesions for VP FX+Q.Clear reconstruction. In this case, the results for the β=450 and β=550 were compared with the result obtained for β=350.
- Comparison of the results of liver uptake and lesions uptake for the three types of reconstruction directly and as a background to tumor ratio. Direct comparison consists of the measurement of the mean and max uptake values and the assessment of their "gross" values between reconstructions. The tumor/background ratio assessment relies on the comparison of the mean and max uptake [kBq/ml] in the lesions by calculating theirs ratio to the mean and max values observed in the liver [kBq/ml]. The analysis is performed for each type of reconstruction, for VP+Q.Clear use and for beta values of 350, 450, 550. The tumor/background relation includes mean and max results in the liver and lesion for a given value of β (the same in both cases). The tumor/background ratio is then compared for different reconstructions.
- Estimation of the ROI volume ratio with the autocontour tool on the ground 42% for VP FX+Q.Clear, VP HD+Q.Clear and VP FX reconstructions.
- Occurrence of differences in the score for the Krenning evaluation for lesions.

The analysis was divided into three types of lesions: very small lesions (diameter < 1.5 cm), small lesions (1.5 – 2.0 cm), medium lesions (2.0 – 4.0 cm). Tumor/background data was obtained by marking the ROI in the liver (900 mm^2), in its homogeneous area, which was not affected by the disease (fig.3.5). An ROI of similar size was also used to evaluate the uptake in the spleen.

Based on the results of the average uptake in the liver, spleen and pathological foci, a comparative analysis of quantitative data was made according to the Krennig scale for all changes. The analysis was performed for all types of image reconstruction and the adopted ranges of beta. For the analysis, it was assumed that the tumour/background ratio was at a similar level if the ratio was no more than 15% of the difference (0.85-1.15). At that time, in the analysis, the tumour/background ratio was considered to be at the level of 1 which equals to “2” at the Krening scale. This approach eliminates the accusation that the ROI in the liver

was wrongly selected and introduces significant error that actually matter. A Krenning score of "2-3" was selected for the described tumour/background ratio (0.85-1.15) (table 3.2).

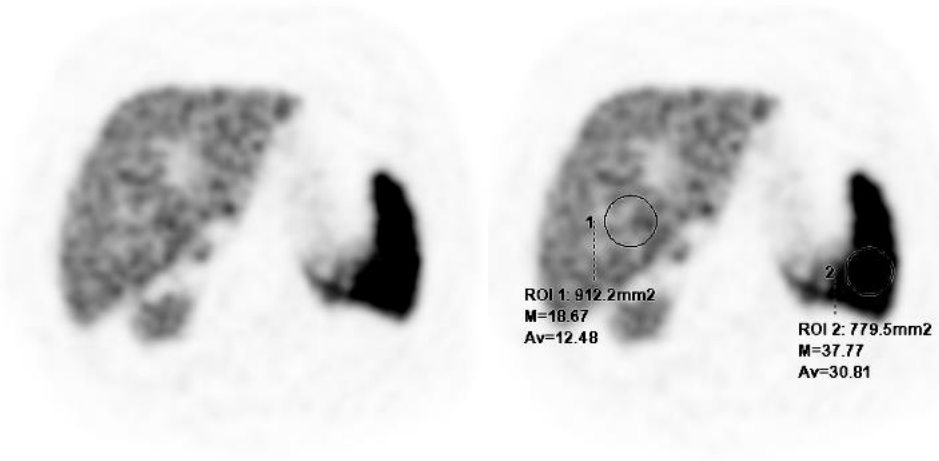

Figure 3. 5 1-layer of the PET/CT image series obtained for the patient with a reference ROI defined in the liver (3), ROI in the spleen (4). Images obtained with the VP FX reconstruction algorithm.

3.2.a.1 Results – very small lesion group

- As the Beta value increased, the relationship between the uptake in lesions and the value of uptake in the liver decreased in all cases as a lesion/background ratio (for both mean and max). The average value of the decrement in the mean value was 7.6% and 6.88% for the maximum value of β (450), and 14.0% and 14.2%, respectively for β=550. In both cases, however, there was a high differentiation of results. The lowest decrease for the mean value was 0.22% and 0.21% fot the max when β was equal to 450, and respectively 1.47% and 3.9% for β=550. The highest decrement for the mean value exceeded even 21%, for the max value it was over 14% (β=450), and over 36% and 26%, respectively (β=550). In the case of the lowest decreases, the changes were located in the bone, the highest differences occurred for changes in the pathological uptake changes were located in the spine. It was observed that the lowest decreases concerned lesions with a tumour/background ratio in the range of up to 1.17. In the case of the highest decreases, the tumour/background ratio was close to 2.77 for the mean value (β=350), and 2.92 for the max value (β=350).
- For the value of β from the range of 350 – 550, apart from 3 changes in this size group, it was observed that the tumour/background ratio is lower for VP HD+Q.Clear and VP FX vs. VP FX+Q.Clear reconstructions. In the remaining cases, there was a relationship in which the VP FX+Q.Clear reconstruction presented the results of a higher tumour/background ratio for the mean and max values. In some cases even more than 30-50%. Typically, the difference was higher the higher was Beta value used in the reconstruction. An inverse

dependence was observed for the VP FX+Q.Clear and VP FX relationships – the beta increment resulted in a difference between the results of the tumour/background relationship. It can be concluded that values of the Beta above 550 reduce the differences between reconstructions to practically imperceptible. The measured mean and max values in the ROIs for liver, spleen and lesions were highest for the VP FX+Q.Clear reconstruction.

- With the increase of the Beta parameter, the size of the ROI increased with a threshold of 42%. Typically, the ROI for VP HD+Q.Clear and VP FX versus VP FX+Q.Clear had a larger volume. The increase in the beta value significantly affected the ROI size in the reconstruction of VP HD+Q.Clear than VP FX+Q.Clear.
- Differences in the Krenning score were present in 54% of the cases when comparing different reconstrution alghoritms. The differences were even as high as 2 points on the scale. The highest scale scores were obtained for the VP FX+Q.Clear reconstruction.

3.2.a.2 Results – small lesion group

- As the Beta value increased, the relationship between the uptake in lesions and the value of uptake in the liver decreased in all cases as a lesion/background ratio (mean and max). The average value of the decrease in the mean value was 1.8% and 4.1% for the max value (β=450), and 3.7% and 7.5%, respectively (β=550). In both cases, there was a large variation in the results, but noticeably lower than for very small changes. The decrease in the mean value for β=450 was in the range of 0.9 – 5.6%. The decrease in the max value for β=450 was in the range of 1.3-7.6%.
- Using the VP FX+Q.Clear reconstruction, the highest tumour/background ratio values were usually obtained for the mean and max values. The images also showed higher uptakes for lesions. The measured mean and max values in the ROIs for liver, spleen and lesions were highest for the VP FX+Q.Clear reconstruction.
- With the increase of the Beta, the size of the ROI increased with a threshold of 42%.
- Changes in the Krenning scale occurred only for one lesion. Kreninng scores were similar (values 1-2) for VP HD+Q.Clear beta 350-550 and VP FX+Q.Clear 550.

3.2.a.3 Results – medium lesion group

- As Beta increased, the relationship between the mean uptake in neoplastic lesions and the value of mean uptake in the liver decreases in almost all cases (exept a single lesion). In the case of two lesions with a very high ratio of background max and max uptake for a lesion, it was observed that the ratio also increases with the increment of the beta parameter.

- Using the VP FX+Q.Clear reconstruction, the highest tumour/background ratio values were usually obtained for the mean and max values. The images also had higher values for capture in lesions. The measured mean and max values in the ROIs for liver, spleen and lesions were highest for the VP FX+Q.Clear reconstruction.
- With the increase of the Beta parameter, the size of the ROI increased with a threshold of 42%.
- There were no changes in the Krenning score.

Table 3. 2 Comparison on the Krenning scale for different image reconstructions for sequentially defined changes in accordance with the table 3.1.

Reconstrution alghoritm	Beta parameter	Krenning score very small lesion													Krenning score small lesion				Krenning score medium lesions						
VP FX	-	**3**	3	**1**	1	**1-2**	3	3	**1-2**	**1**	3	3	**1**	**2-3**	**1-2**	1	4	4	4	3	3	3	4	4	4
VP FX+Q.Clear	350	**4**	3	**3**	1	**3**	3	3	**4**	**1-2**	3	3	**2-3**	**3**	**2-3**	1	4	4	4	3	3	3	4	4	4
	450	**4**	3	**3**	1	**3**	3	3	**3**	**1-2**	3	3	**2-3**	**3**	**2-3**	1	4	4	4	3	3	3	4	4	4
	550	**3**	3	**3**	1	**3**	3	3	**3**	**1**	3	3	**2-3**	**3**	**1-2**	1	4	4	4	3	3	3	4	4	4
VP HD+Q.Clear	350	**3**	3	**2-3**	1	**3**	3	3	**3**	**1**	3	3	**2-3**	**3**	**1-2**	1	4	4	4	3	3	3	4	4	4
	450	**3**	3	**1**	1	**3**	3	3	**1-2**	**1**	3	3	**1-2**	**3**	**1-2**	1	4	4	4	3	3	3	4	4	4
	550	**3**	3	**1**	1	**3**	3	3	**1-2**	**1**	3	3	**1-2**	**3**	**1-2**	1	4	4	4	3	3	3	4	4	4

3.2.b. Discussion

The obtained results show that there are large differences between the values obtained for the VP FX/HD+Q.Clear and VP FX reconstructions. This applies to both the direct results of mean and max values. With the increase in the measured uptake values, the background values, i.e. uptake in the liver and spleen, also increased. This affected the final tumour/background ratio. However, despite the highest increase in the background value, the results for the VP FX+Q.Clear reconstruction tumour/background ratio were the highest, with very good image quality. The area of the thorax and healthy liver and spleen also was homogeneous .

An interesting result is the influence of the choice of image reconstruction on the data in the Krenning scale. The change in beta for the VP FX/HD+Q.Clear reconstruction had a very significant impact on the assessment of a lesion in this scale. The choice of VP FX+Q.Clear not only increased the tumour/background ratio, it was also significant for the description of the clinical condition. In this case, the patient examination result presents usually as a more advanced stage than if the image had been reconstructed using other reconstruction algorithms. Overall, VP HD+Q.Clear scores in the 450 – 550 range were in line with VP FX reconstruction scores.

There were also very large discrepancies observed in the contour size when using the autocontour for the VP HD+Q.Clear reconstruction. This was very unfavourable as it additionally reduced the mean uptake in the designated ROI. Due to the phenomenon of a slight decrease in the mean values for the VP FX+Q.Clear reconstruction, no large changes in contours were observed for the determined ROIs using the autocontour method.

The observed changes were random and it is difficult to assess what really caused that in certain situations there were large differences between the VP FX+Q.Clear reconstruction and the others. Presumably, it can be assessed that changes with uptake close to the background are more difficult to isolate as independent, hence the relatively large size of these lesions and the relatively low level for uptake expressed as an average ROI value.

4. Conclusions

The conducted studies have shown that there is a variability of the obtained tumour/background values between the types of reconstruction applied, as well as between different settings of Beta parameter. This is very important conclusion, because the differentiation of the tumour/background ratio affects the assessment of the severity of the condition in the case of neuroendocrine tumours. As in the case of studies using a phantom, the greatest effect of Beta and reconstruction choice was visible for very small lesions.

The partial volume effect (PVE) probably has a huge impact on this. The range of positrons formed as a result of radioactive decay for the ^{68}Ga isotope is relatively high in the tissue, so there is a large blur at the boundary of region high capture score. In the case of very small lesions this phenomenon can not compensate even with the best mathematical description, the detector simply reads the annihilation phenomenon at a certain distance from the positron occurrence in the patient's body. The Q.Clear reconstruction somewhat compensates for this phenomenon, especially if the time of flight of photons is used.

Unfortunately, it is very difficult to precisely determine the impact of Q.Clear reconstruction on the diagnostic process. The results obtained from the patient imaging data show that there is a high variability in the impact of Q.Clear reconstruction on the tumour/background ratio. However, these changes do not occur in every case. Thus, a fairly generalized conclusion can be drawn that the Q.Clear reconstruction is characterized by better sensitivity for lesions with low uptake and small size.

Comparison of studied algorithms showed that the most advantageous diagnostic solution is the use of VP FX+Q.Clear reconstruction in the range of 350 – 450 for Beta. Lower values indicate an increase in heterogeneity in the liver and in the thoracic region. Similar results are obtained as for OSEM reconstruction with time-of-flight corrections. When comparing the results from different Centers, one should be careful what type of reconstruction was used, because lesions, despite the lack of progression, may show a higher uptake, even in the Krenning scale.

Similar results can be obtained for patients undergoing therapy to assess response to treatment for which we assess the value of SUV peak (Chapter I, 3.5). The value of SUV peak also decreases as Beta increases. The impact of this change is more significant for VP HD+Q.Clear reconstructions. This may result in the patient's imaging affecting the assessment of response to treatment.

Summary

In the following work, a full analysis of the quality of the obtained images was performed using iterative image reconstructions available on the PET/CT Discovery MI DR device. The device is installed at the University Hospital in Kraków and is used for routine diagnostics of oncological patients. The results of patient examinations can also be used to plan radiotherapy treatment using classical linear accelerators and stereotactic techniques.

The available literature data presented in scientific publications and the manufacturer's data showed that the use of the Q.Clear algorithm for image reconstruction allows to achieve more accurate results of oncological patients by obtaining higher tumour/background ratio values. Literature data ambiguously indicated how the beta parameter is selected. Most often, only limited measurements were made to compare different image reconstruction techniques. The results presented in this paper allow for:

1. assessment of the real difference between VP HD+Q.Clear, VP FX+Q.Clear and VP FX reconstructions,
2. assessment of the real impact of beta parameter choice for reconstruction with Q.Clear,
3. **selection of a safe and reliable image reconstruction algorithm for treatment planning and diagnosis of patients with neuroendocrine tumours imaged with radiolabelled somatostatin analogues ^{68}Ga isotope.**

Bibliography

1. Saha G.B., *Physics and Radiobiology of Nuclear Medicine*, 3rd Edition, New York, Springer, 2006.
2. Jevremovic T., *Nuclear Principlesin Engineering*, 2nd Edition, New York, Springer, 2009.
3. Phelps M.E., *PET – Pyhsics, Instrumentation, and Scanners*, New York, Springer, 2006.
4. Kapoor V., McCook B.M.,Torok *An Introduction to PET-CT Imaging,* RadioGraphics, vol. 24, no. 2, 2004, pp. 523-543.
5. Bailey D. L., Townsend D. W., Valk P. E., *Positron Emission Tomography: Basic Science and Clinical Practice,* London, Springer, 2005.
6. Currie G.M., Wheat J.M., Davidson R., Kiat H., *Radionuclide production,* The Radiographer, vol. 58, no. 3, 2010, pp. 46-52.
7. Cantone M.C., Hoeschen Ch. (editors), *Radiation Physics for Nuclear Medicine*, Berlin Heidelberg, Springer-Verlag, 2011.
8. *IAEA RADIOISOTOPES AND RADIOPHARMACEUTICALS*, no. 2, Vienna, IAEA, 2010.
9. *Charakterystyka produktu leczniczego, SPC_GalliaPharm_V01_PL* https://www.synektik.com.pl/assets/Uploads/SPC-Galliapharm-PL-02.15.PDF 06.02.2021.
10. Lewellen T.K., *Recent developments in PET detector technology , Phys. Med. Biol.*, Vol. 53, No. 17, 2008, pp. R287–R317.
11. Moskal P., Kisielewska D., Curceanu C., et all, *Feasibility study of the positronium imaging with the J-PET tomography*, Phys. Med. Biol., vol. 64, 2019.
12. Turkington T.G., *Introduction to PET Instrumentation,* J. Nucl. Med. Technol, vol. 29, 2001, pp. 1–8.
13. Instrukcja do aparatu PET-CT Discovery_MI DR.
14. Lecomte R., *Novel detector technology for clinical PET,* Eur. J. Nucl. Med. Mol. Imaging, vol. 36, 2009, pp. 69–85.
15. Levin C.S., Hoffman E.J., *Calculation of positron range and its effect on the fundamental limit of positron emission tomography system spatial resolution,* Phys. Med. Biol., vol. 44, no.3,1999, pp. 781–799.
16. M. Soret, S. Bacharach, I. Buvat, *Partial-Volume Effect in PET Tumor Imaging*, The Journal of Nuclear Medicine, vol. 48, no. 6, June 2007.
17. Henkin R. E., Bova D., Dillehay G. L., *Nuclear Medicine, 2nd Edition,* St. Louis Missouri, Mosby, 2006.
18. Kak A. C., Slaney M., *Principles of Computerized Tomographic Imaging*, Society of Industrial and Applied Mathematics, 1988.
19. Helgason S., *The Radon Transform, 2nd Edition*, Boston, Springer, 1999.
20. Tong S., Alessio A. Kinahan M., P. E., *Image reconstruction for PET/CT scanners: past achievements and future challenges*, Imaging Med., vol. 2, no. 5, 2010, pp. 529-545.
21. Sio-Iong A., Gelman L. *(editors), Advences in Electrical Engineering and Computional*, Springer 2009.
22. Hsieh J., Nett B., Yu Z., Sauer K., Thibault Jean-Baptiste, et all, *Recent Advances in CT Image Reconstruction*, Curr. Radiol. Rep., vol/no. 1, 2013, pp. 39–51.

23. Vandenberghea S., D'Asselera, Van de Wallea Y. R., et all, *Iterative reconstruction algorithms in nuclear medicine*, Computerized Medical Imaging and Graphics, vol/no. 25, 2001, pp. 105-111.
24. Bruyant P.P., *Analytic and Iterative Reconstruction Algorithms in SPECT* , J Nucl Med, vol. 43, no. 10, 2002, pp. 1343-1358.
25. J. Fessler, *NSS/MIC statistical image reconstruction short course notes*, 2001 www.eecs.umich.edu/fessler/papers/talk.html
26. Leahy R, Qi J., *Statistical approaches in quantitative positron emission tomography. Statistics and Computing*, vol. 10, 2000, pp.147–165.
27. Frederik A.A. de Jonge, Koos (J.) A.K. *Blokland Statistical tomographic reconstruction: How many more iterations to go?*, Eur. J. Nucl. Med., vol. 26, 1999, pp.1247–1250.
28. Geyer L. L., Schoepf U. J., Meinel F. G., et all, *State of the Art: Iterative CT Reconstruction Techniques*, Radiology, vol. 276, no. 2, 2015, pp. 339-357.
29. Argaund Ch., *ASiR a new reconstruction technique to lower dose without compromise*, GE Healthcare.
30. Lewellen T. K., *Time-of-Flight PET, Seminars in Nuclear Medicine*, vol. XXVIII, no. 3, 1998, pp. 268-275.
31. Barca P., Giannelli M., Fantacci M.E., Caramella D., *Computed tomography imaging with the Adaptive Statistical Iterative Reconstruction (ASIR) algorithm: dependence of image qualityon the blending level of reconstruction*, Australasian Physical & Engineering Sciences in Medicine, vol. 41, 2018, pp. 463–473.
32. Sæterstøl J. (master of science thesis), *Characterization of Scintillation Crystals for Positron Emission Tomography*, University of Bergen, Faculty of Mathematics and Natural Sciences Department of Physics and Technology, Bergen, 2010.
33. Karp J. S., Surti S., Daube-Witherspoon M.E., Muehllehner G., *Benefit of Time-of-Flight in PET: Experimental and Clinical Results*, J Nucl Med, vol. 49, no. 3, 2008, pp. 462-470.
34. *VUE Point HD Bringing accuracy to PET reconstruction*, GE Healthcare, 2008.
35. *Clinical Implementation of VUE Point FX*, GE Healthcare, 2009.
36. Ross S., Stearns Ch., *Sharp IR white paper*, GE Healthcare.
37. Vennarta N. J., Birda N., Buscombea Cheowa J. H. K., et all, *Optimization of PET/CT image quality using the GE 'Sharp IR'point-spread function reconstruction algorithm*, Nuclear Medicine Communications, vol. 38, no. 6, 2017, pp. 471-479.
38. Ross S., *Q.Clear*, GE Healthcare.
39. Teoh E.J., McGowan D. R., Macpherson R.E., et all, *Phantom and clinical evaluation of the Bayesian penalized likelihood reconstruction algorithm Q.Clear on an LYSO PET/CT system, J Nucl Med*., vol. 56, no. 9, 2015, pp. 1447–1452.
40. Messerli M., Stolzmann P., Egger-Sigg M., et all, *Impact of a Bayesian penalized likelihood reconstruction algorithm on image quality in novel digital PET/CT: clinical implications for the assessment of lung tumors*, EJNMMI Physics, 2018, pp. 5-7.
41. Rogasch M. J, Suleiman S, Hofheinz F, et al. *Reconstructed spatial resolution and contrast recovery with Bayesian penalized likelihood reconstruction (Q.Clear) for FDG-PET compared to time-of-flight (TOF) with point spread function (PSF*), EJNMMI Phys., vol. 7, 2020.

42. Rijnsdorp S, Roef JM, Arends JA, *Impact of the Noise Penalty Factor on Quantification in Bayesian Penalized Likelihood (Q.Clear) Reconstructions of 68Ga-PSMA PET/CT Scans*, Diagnostics, vol. 11, no. 5, 2021.
43. Barrington S., Blower P., Cook G., *New horizons in multimodality molecular imaging and novel radiotracers*, Clinical Medicine, vol. 17, no 5, 2017, pp. 444–448.
44. Zaidi H., Prasad R., *Advances in multimodality molecular imaging*, J. Med. Phys., vol. 34, no. 3, 2009, pp. 122–128.
45. Shreve P., Townsend D. W. (editors), *Clinical PET-CT in Radiology*, New York, Springer, 2011.
46. Mawlawi O. R., Kemp B.J., Jordan D. W., et all, *PET/CT Acceptance Testing and Quality Assurance*, AAPM REPORT NO. 126, American Association of Physicists in Medicine, 2019.
47. Kinahan P. E., Fletcher J. W., *PET/CT Standardized Uptake Values (SUVs) in Clinical Practice and Assessing Response to Therapy*, Semin Ultrasound CT MR, vol. 31, no. 6, 2010, pp. 496–505.
48. Bai1 B., Bading J., Conti P., *Tumor Quantification in Clinical Positron Emission Tomography*, Theranostics, vol. 3, issue 10, 2013.
49. National Electrical Manufacturers Association, *NEMA Standards Publication NU 2-2018 Performance Measurements of Positron Emission Tomographs (PETS)*, 1300 N. 17th Street, Suite 900 Rosslyn, VA 22209
50. Hyun O J., Lodge M., Wahl R., *Practical PERCIST: A Simplified Guide to PET Response Criteria in Solid Tumors 1.01*, Radiology, vol. 280, no. 2, 2016.
51. Oronsky B., Ma P. C., Morgensztern D., et all, *Nothing But NET: A Review of Neuroendocrine Tumors and Carcinomas*, Neoplasia, vol. 19, 2017, pp. 991–1002.
52. Jeziorski G.K., *Guzy neuroendokrynne układu pokarmowego,* Gastroenterologia Kliniczna, vol. 3, no. 4, 2011, pp. 154–158
53. Yalcin S., Öberg K. (editors) *Neuroendocrine Tumours Diagnosis and Management*, Berlin Heidelberg, Springer, 2015.
54. Hubalewska-Dydejczyk A. (editor), *Somatostatin Analogues From Research to Clinical Practice*, New Jersey, John Wiley & Sons, 2015.
55. Virgolini I., Ambrosini V., Bomanji J. B., et all, *Procedure guidelines for PET/CT tumour imaging, with 68Ga-DOTA-conjugated peptides: 68Ga-DOTA-TOC, 68Ga-DOTA-NOC, 68Ga-DOTA-TATE*, Eur. J. Nucl. Med. Mol. Imaging, vol. 37, 2010, pp.2004–2010.
56. Hofman M.S., Lau W. F. E., Hicks R.J., S*omatostatin Receptor Imaging with 68Ga DOTATATE PET/CT: Clinical Utility, Normal Patterns, Pearls, and Pitfalls in Interpretation, RG* , vol.35, no. 2, 2015, pp. 500-516.
57. Baum R. P., Rosch F., (editors), *Theranostics, Gallium-68, and Other Radionuclides*, New York, Springer, 2013, pp 353-371.
58. Rep S., Santos A., Testanera G. (editors), *Radiation Protection and Dose Optimisation A Technologist's Guide European Association of Nuclear Medicine*, Vienna, 2016.
59. *Pasionek S. Radiofarmaceutyki we współczesnej medycynie, praca licencjacka, UJ, 2018.*
60. https://www.dicardiology.com/article/ge-healthcare-receives-fda-qclear-petct-technology - link active as of 31/05/2023.
61. *Discovery MI Digital Ready Data Sheet_DOC1846138.*

62. Spencer B., Berg E., Schmall J., et all, *Discovery MI Digital Ready Data Sheet_DOC1846138Performance Evaluation of the uEXPLORER Total-Body PET/CT Scanner Based on NEMA NU 2-2018 with Additional Tests to Characterize PET Scanners with a Long Axial Field of View*, The Journal of Nuclear Medicine, vol. 62 no. 6, June 2021.
63. Raczkowska J., Rysz J., Budkowski A., et all, *Surface Patterns in Solvent-Cast Polymer Blend Films Analyzed with an Integral-Geometry Approach*, Macromolecules, 2002.
64. *Adsorpcja białek i tworzenie ich wzorów na powierzchni cienkich warstw polimerów,* Joanna Zemła Praca doktorska, UJ, 2012.
65. Krempser A., Ichinose R., Miranda de Sa A., et all, *Recovery coefficients determination for partial volume effect correction in oncological PET/CT images considering the effect of activity outside the field of view*, Ann. Nucl. Med., vol. 27, 2013, pp. 924–930.
66. Kohlmyer, S. G., Vesselle, H., Miyaoka, R. S., et all, *Comparison of recovery coefficients for PET based on maximum and average ROI pixel values*, Eur. J. Nucl. Med., vol. 27, 2000.
67. National Electrical Manufacturers Association, *NEMA Standards Publication NU 2-2012 Performance Measurements of Positron Emission Tomographs*, 1300 N. 17th Street, Suite 900 Rosslyn, VA 22209
68. Rogasch J., Suleiman S., Hofheinz F., et al. *Reconstructed spatial resolution and contrast recovery with Bayesian penalized likelihood reconstruction (Q.Clear) for FDG-PET compared to time-of-flight (TOF) with point spread function (PSF)*, EJNMMI Phys., vol.7, no. 2, 2020.
69. Rijnsdorp S., Roef JM., Arends JA, *Impact of the Noise Penalty Factor on Quantification in Bayesian Penalized Likelihood (Q.Clear) Reconstructions of 68Ga-PSMA PET/CT Scans*, Diagnostics, vol. 11, 2021.
70. Tian D., Yang H., Li1 Y., et all, *The effect of Q.Clear reconstruction on quantification and spatial resolution of 18F-FDG PET in simultaneous PET/MR*, EJNMMI Physics, vol.9, no. 1, 2022.
71. Ruan W., Qin Ch., Liu1 F., et all, *Q.Clear reconstruction for reducing the scanning time for 68 Ga-DOTA-FAPI-04 PET/MR imaging*, Eur. J. Nucl. Med. Mol. Imaging, vol. 50, no. 7, 2023, pp.1851-1860.
72. Ribeiro D., Hallett W., Tavares A., *Performance evaluation of the Q.Clear reconstruction framework versus conventional reconstruction algorithms for quantitative brain PET-MR studies*, EJNMMI Physics, vol. 8, no. 41, 2021.
73. Reddy R., Hainer J., Sticka W., Park Mi-Ae, *Evaluation of different reconstruction algorithms in contrast recovery for noncentrally located small lesions*, Journal of Nuclear Medicine, vol. 59 (supplement 1), 2018.
74. Hicks J., Dromain C., de Herder W. Costa F., et all, *ENETS standardized (synoptic) reporting for molecular imaging studies in neuroendocrine tumours Rodney*, J. Neuroendocrinol., vol. 34, no. 3, 2022.

List of Figures/Charts

List of Tables